

## MEG Upgrade Proposal

A. M. Baldini<sup>a,\*</sup>, F. Cei<sup>ab</sup>, C. Cerri<sup>a</sup>, S. Dussoni<sup>a</sup>, L. Galli<sup>a</sup>, M. Grassi<sup>a</sup>,

D. Nicolò<sup>ab</sup>, F. Raffaelli<sup>a</sup>, F. Sergiampietri<sup>a</sup>, G. Signorelli<sup>a</sup>, and F. Tenchini<sup>ab</sup>

*INFN Sezione di Pisa<sup>a</sup>; Dipartimento di Fisica<sup>b</sup> dell'Università, Largo B. Pontecorvo 3, 56127 Pisa, Italy*

D. Bagliani<sup>ab</sup>, M. De Gerone<sup>a</sup>, and F. Gatti<sup>ab</sup>

*INFN Sezione di Genova<sup>a</sup>; Dipartimento di Fisica<sup>b</sup> dell'Università, Via Dodecaneso 33, 16146 Genova, Italy*

E. Baracchini, Y. Fujii, T. Iwamoto, D. Kaneko, T. Mori,\*

M. Nishimura, W. Ootani, R. Sawada, and Y. Uchiyama

*ICEPP, The University of Tokyo 7-3-1 Hongo, Bunkyo-ku, Tokyo 113-0033, Japan*

G. Boca<sup>ab</sup>, P. W. Cattaneo<sup>a</sup>, A. de Bari<sup>a</sup>, R. Nardó<sup>a</sup>, and M. Rossella<sup>a</sup>

*INFN Sezione di Pavia<sup>a</sup>; Dipartimento di Fisica Nucleare e Teorica<sup>b</sup> dell'Università, Via Bassi 6, 27100 Pavia, Italy*

M. Cascella<sup>ab</sup>, F. Grancagnolo<sup>a</sup>, A. L'Erario<sup>ac</sup>, A. Maffezzoli<sup>ac</sup>, A. Miccoli<sup>a</sup>, G. Onorato<sup>ad</sup>,

G. Palamà<sup>ab</sup>, M. Panareo<sup>ab</sup>, A. Pepino<sup>a</sup>, S. Rella<sup>ac</sup>, G.F. Tassielli<sup>ad</sup>, and G. Zavarise<sup>ac</sup>

*INFN Sezione di Lecce<sup>a</sup>; Dipartimento di Matematica e Fisica<sup>b</sup> dell'Università;*

*Dipartimento di Ingegneria dell'innovazione<sup>c</sup> dell'Università, Via per Arnesano,*

*73100 Lecce, Italy; Università "G. Marconi"<sup>d</sup>, Via Plinio 44, 00193 Roma, Italy*

G. Cavoto<sup>a</sup>, A. Graziosi<sup>a</sup>, G. Piredda<sup>a</sup>, E. Ripiccini<sup>ab</sup>, and C. Voena<sup>a</sup>

*INFN Sezione di Roma<sup>a</sup>; Dipartimento di Fisica<sup>b</sup> dell'Università "Sapienza", Piazzale A. Moro, 00185 Roma, Italy*

D. N. Grigoriev, F. Ignatov, B. I. Khazin, A. Popov, and Yu. V. Yudin

*Budker Institute of Nuclear Physics, 630090 Novosibirsk, Russia*

T. Haruyama, S. Mihara, H. Nishiguchi, and A. Yamamoto

*KEK, High Energy Accelerator Research Organization 1-1 Oho, Tsukuba, Ibaraki 305-0801, Japan*

M. Hildebrandt, P.-R. Kettle, A. Papa, F. Renga, S. Ritt, and A. Stoykov

*Paul Scherrer Institut PSI, CH-5232 Villigen, Switzerland*

T. I. Kang, G. Lim, W. Molzon, and Z. You

*University of California, Irvine, CA 92697, USA*

N. Khomutov, A. Korenchenko, N. Kravchuk, and N. Kuchinsky

*Joint Institute for Nuclear Research, 141980, Dubna, Russia*

---

\*Spokespersons

## Contents

<b>I. Executive Summary</b>	5
<b>II. Status of the MEG experiment in the framework of experimental charged Lepton Flavour Violation (cLFV) searches</b>	7
<b>III. Scientific merits of the MEG upgrade</b>	11
<b>IV. Upgrade Overview</b>	16
A. Key elements to a MEG upgrade	16
B. Discussion	16
C. Auxiliary devices	19
<b>V. Beam Line and Target</b>	20
A. The MEG beam line and muon target	20
B. Beam Line and Target Upgrade Potential	23
C. Use of a Sub-surface Muon Beam	23
<b>VI. Positron detector</b>	28
A. The positron tracker	28
1. Mechanics	29
2. Ageing tests	32
3. Monte Carlo simulation	35
4. Fast read-out and the cluster timing technique	38
5. Tests for spatial resolution studies	41
B. Pixelated Timing Counter	44
1. Foreword and Status of the Art	44
2. Concept of New Detector	45
3. Pixel Module Design	46
4. Scintillator	47
5. Silicon Photomultiplier (SiPM)	47
6. Support Structure	49
7. Test with Pixel Counter Prototype	50
8. Expected Performance	54

9. Calibration	57
10. Other Issues	58
11. R&D Plan	60
<b>VII. Gamma detector</b>	61
A. Concept of Upgrade	61
B. Development of VUV-sensitive MPPC	63
1. MPPC Advantage	63
2. Issues	64
3. Setup	65
4. PDE	65
5. Transit Time Spread	67
6. Temperature Dependence	67
7. Radiation Hardness	69
8. Linearity	70
9. Large Area Samples	70
10. Possible Further Improvements of MPPC Performance	71
11. MPPC in Other Experiments	72
C. Detector Design	73
1. Design of Sensor Package and Assembly	73
2. Signal Transmission	75
3. Test with Cables and Prototype PCBs	77
4. Readout Electronics	79
5. Cryogenics	79
D. Expected performance	79
1. Simulation	79
2. Results	80
3. High intensity	82
E. Prototype Detector	83
<b>VIII. Trigger and DAQ</b>	86
A. Requirements	86
B. Proposed DAQ boards—WaveDREAM	86
C. Trigger	87

	4
D. Data reduction	88
<b>IX. Final sensitivity</b>	<b>90</b>
<b>X. Costs and responsibilities</b>	<b>93</b>
<b>XI. Time Schedule and Man Power</b>	<b>96</b>
<b>XII. Summary</b>	<b>102</b>
<b>XIII. Appendix</b>	<b>103</b>
A. The Active target option	103
1. Active target concept	103
2. Monte-Carlo simulations	104
3. Experimental set-up for R & D studies	105
4. Conclusion	109
B. Radiative muon decay veto counter : RDC	109
C. TPC-based tracker option	112
1. Concept	112
2. Design	113
3. Expected Performance	116
4. Prototyping Plan	118
D. Silicon vertex tracker option: SVT	119
1. Concept	119
2. Design	122
3. Expected performance	124
E. R&D on New Scintillator Material for Timing Counter	125
F. Development of New Photomultiplier Tube (PMT) for LXe Detector	127
<b>References</b>	<b>129</b>

## I. EXECUTIVE SUMMARY

We propose the continuation of the MEG experiment to search for the charged lepton flavour violating decay (cLFV)  $\mu \rightarrow e\gamma$ , based on an upgrade of the experiment, which aims for a sensitivity enhancement of one order of magnitude compared to the final MEG result. The current MEG experiment can be considered, apart from its discovery potential, as a benchmark for next-generation cLFV decay experiments. This, not only by having imposed one of the most stringent constraints to date on models predicting large LFV-enhancements through "New Physics" beyond the Standard Model (BSM), but also by setting the tightest upper limit on the decay itself, that of  $2.4 \times 10^{-12}$  (90% C.L.). On the experimental side, a benchmark has also been set by both having designed and run the experiment close to the intensity frontier, made possible by the PSI high-intensity proton accelerator facility (HIPA).

The planned sensitivity enhancement for an upgraded MEG experiment would, together with the planned next generation  $\mu \rightarrow e$  conversion experiments COMET at J-PARC and Mu2e at Fermilab and the next-generation  $\mu \rightarrow eee$  experiment at PSI, which seek to probe the other two "Golden" cLFV muon channels, and in addition to efforts at future B-factories to measure the charged LFV tau-decays, test BSM models with unprecedented sensitivity, in a complementary way, to the direct searches at the energy frontier of high-energy colliders. Furthermore, the cLFV experiments also allow access to mass scales for "New Physics" well beyond the reach of the direct searches at colliders.

The MEG experiment is currently close to finishing its 2012 run on schedule, having been able to double its statistics of 2011 and having achieved more than a factor of three more statistics than used for the previously published best limit. The experiment is expected to continue data-taking until mid 2013, when a sensitivity of about  $\sim 6 \cdot 10^{-13}$  is expected to be reached, beyond which only limited improvement is expected due to the expected increasing dominance of background events in the signal region. Therefore, in order to significantly improve the sensitivity reach with a goal of being able to detect the  $\mu \rightarrow e\gamma$  decay at a level of about one order of magnitude lower, a new upgraded MEG experiment is required.

The key features of this new MEG upgrade, aimed at significantly improving the experimental sensitivity, are to increase the rate capability of all detectors to enable running at the intensity frontier, while also improving the energy and angular and timing resolutions, for both the positron and photon arms of the detector. This is especially valid on the positron-side, where a new low-mass, single volume, high granularity tracker is under development. This, in combination with a thinner stopping target and hence a reduction in the multiple scattering of the positrons, will lead to the spatial, angular and energy requirements being met on the positron side. A new highly segmented, fast timing counter array will replace the old system, so allowing improved timing resolution capabilities in order to minimize the number of background events

entering the signal timing window. The photon-arm, with the largest liquid xenon (LXe) detector in the world, totalling 900 l, will also be improved by increasing the granularity at the incident face, by replacing the current photomultiplier tubes (PMTs) with a larger number of smaller photosensors and optimizing the photosensor layout also on the lateral faces. This should also lead to improved energy and spatial resolutions for the LXe detector. Finally, in order to meet the stringent requirements of an increased number of readout channels and to cope with the necessary bandwidth required by such a system, a new DAQ scheme involving the implementation of a new combined readout board capable of integrating the various functions of digitization, trigger capability and splitter functionality into one condensed unit, is also under development.

During the R&D that has been on-going since 2011, various complementary and auxiliary devices and technologies have been studied in order to reach the baseline solution outlined in this proposal. Some of these devices have been developed to a significant level, such that once prototypes have been rigorously tested under realistic beam conditions they could then be introduced into the running experiment, so allowing for further improvements.

The overall planned schedule for the upgrade and its implementation is shown in the timeline in Figure 1. An initial period of design and development, with the planned end of construction date of around mid 2015, is to be followed by an engineering run in the latter half of 2015 and, providing the performance is as expected, data-taking could start in 2016. The present sensitivity estimate is based on a muon stopping rate of  $7 \cdot 10^7$  muons/s for a running time of 3 years, assuming 180 DAQ days per year.

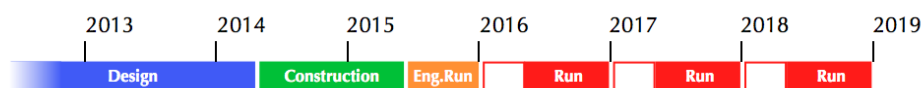


FIG. 1: Planned Schedule for the MEG Upgrade, showing the periods for R&D, construction, and implementation, as well as an Engineering Run followed by three years of data-taking.

In the following sections of the proposal, a detailed description of the current status of the MEG experiment, the scientific merits of an upgrade and the detailed overview of the key features involved will be addressed. In conclusion to this, the sensitivity reach of such an upgrade will be given, as well as the necessary collaboration infrastructure, costs, manpower and a detailed time schedules presented. In the appendix, an overview of the complementary and auxiliary devices and technologies studied will be given.

Finally, the MEG collaboration is confident that the goals outlined of such a MEG upgrade will lead to the new MEG experiment being a further benchmark for future LFV experiments.

## II. STATUS OF THE MEG EXPERIMENT IN THE FRAMEWORK OF EXPERIMENTAL CHARGED LEPTON FLAVOUR VIOLATION (CLFV) SEARCHES

The experimental upper limits established in searching for cLFV processes including the  $\mu \rightarrow e\gamma$  decay are shown in Fig. 2 as a function of the year. Historically, the negative results of these experiments led to the formulation of the Standard Model (SM) of elementary particles interactions, in which lepton flavour conservation is put directly in from the beginning. During the past 35 years the experimental sensitivity to the  $\mu \rightarrow e\gamma$  decay has improved by almost three orders of magnitude, thanks to improvements in detector and beam technologies. In particular surface muon beams (i.e. beams of muons originating in the decay of  $\pi^+$ s that stopped in the pion production target) with a momentum of  $\sim 29 \text{ MeV}/c$ , offer the highest muon stop densities obtainable at present, allowing for the low-mass experimental targets that are required to reach the ultimate resolution in positron momentum and emission angle and to suppress the generation of the unwanted  $\gamma$ -background.

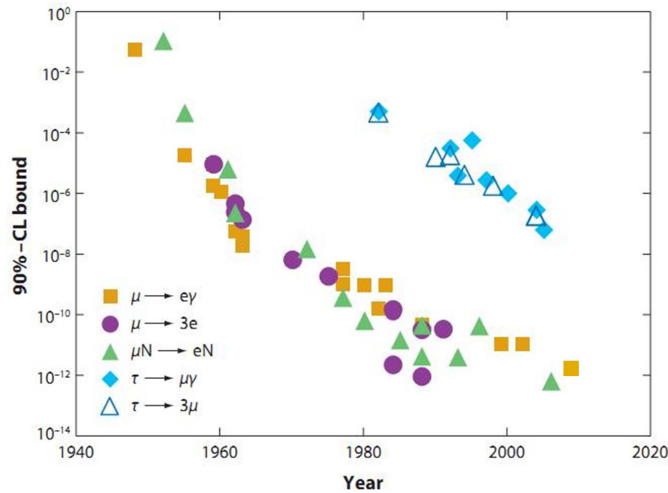


FIG. 2: Upper limits on cLFV processes as a function of the year

The MEG experiment at the Paul Scherrer Institute (PSI, Zurich, Switzerland) uses the world's most intense (higher than  $10^8 \mu/s$ ) continuous surface muon beam but, for reasons explained in the following, the stopping intensity is limited to  $3 \times 10^7 \mu/s$ . The signal of the possible two-body  $\mu \rightarrow e\gamma$  decay at rest is distinguished from the background by measuring the photon energy  $E_\gamma$ , the positron momentum  $P_e$ , their relative angle  $\Theta_{e\gamma}$  and timing  $t_{e\gamma}$  with the best possible resolutions <sup>1</sup>.

<sup>1</sup> In the following we will indicate the ( $1\sigma$ ) resolution on a variable with a  $\Delta$  in front of that variable

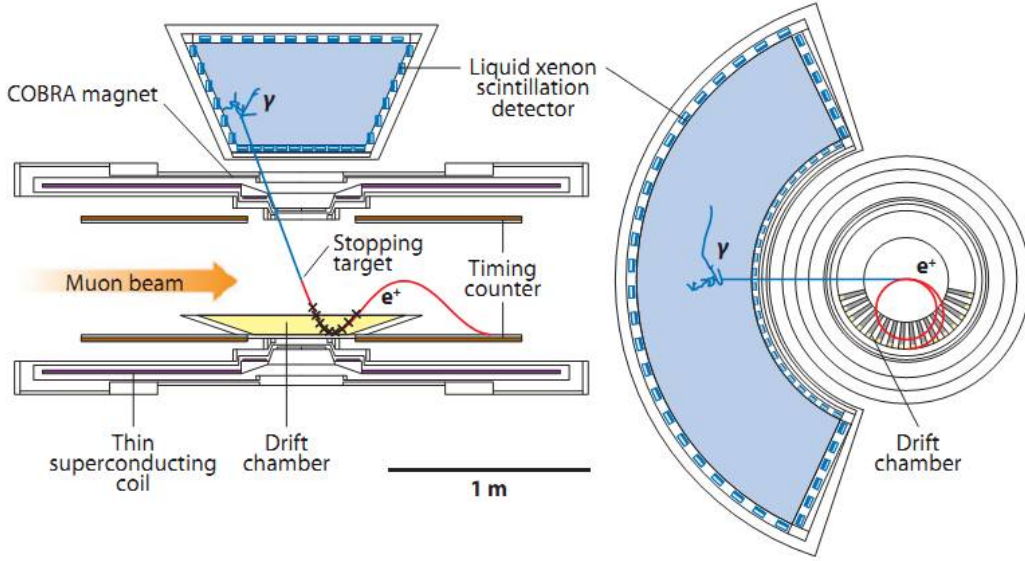


FIG. 3: A sketch of the MEG experiment

Muons are stopped in a thin ( $205 \mu\text{m}$ ) polyethylene target, placed at the centre of the experimental set-up which includes a positron spectrometer and a photon detector, as sketched in Fig. 3. The positron spectrometer consists of a set of drift chambers and scintillating timing counters located inside a superconducting solenoid with a gradient magnetic field along the beam axis, ranging from 1.27 Tesla at the centre to 0.49 Tesla at either end. The photon detector, located outside of the solenoid, is a homogeneous volume ( $900 \ell$ ) of liquid xenon (LXe) viewed by 846 UV-sensitive photomultiplier tubes (PMTs) submerged in the liquid. The spectrometer measures the positron momentum vector and timing, while the LXe detector is used to reconstruct the  $\gamma$ -ray energy as well as the position and time of its interaction in LXe. All the signals are individually digitized by in-house designed waveform digitizers (DRS) [1].

The background comes either from radiative muon decays  $\mu^+ \rightarrow e^+ \nu \bar{\nu} \gamma$  (RMD) in which the neutrinos carry away little energy or from an accidental coincidence of an energetic positron from a normal Michel decay with a photon coming from RMD, bremsstrahlung or positron annihilation-in-flight.

The number of accidental coincidences ( $N_{\text{acc}}$ ), for given selection criteria, depends on the experimental resolutions with which the four relevant quantities ( $E_\gamma$ ,  $P_e$ ,  $\Theta_{e\gamma}$ ,  $t_{e\gamma}$ ) are measured. By integrating the RMD photon and Michel positron spectra over respectively the photon energy and positron momentum resolution it can be shown that:

$$N_{\text{acc}} \propto R_\mu^2 \times \Delta E_\gamma^2 \times \Delta P_e \times \Delta \Theta_{e\gamma}^2 \times \Delta t_{e\gamma} \times T \quad (1)$$

where  $R_\mu$  is the rate of stopping muons and  $T$  is the measurement time. The number of expected signal events for a given branching ratio ( $\mathcal{B}$ ) is instead related to the solid angle  $\Omega$  subtended by the photon and positron detectors, the total acquisition time ( $T$ ), the efficiencies of these detectors ( $\epsilon_\gamma$ ,  $\epsilon_e$ ) and the efficiency of the selection criteria ( $\epsilon_s$ ):<sup>2</sup>

$$N_{\text{sig}} = R_\mu \times T \times \Omega \times \mathcal{B} \times \epsilon_\gamma \times \epsilon_e \times \epsilon_s \quad (2)$$

The Single Event Sensitivity (SES) is defined as the  $\mathcal{B}$  for which the experiment would see one event. In principle the lowest SES, and therefore the largest possible  $R_\mu$ , is experimentally desirable in order to be sensitive to the lowest possible  $\mathcal{B}$ . However, due to the quadratic dependence on the muon stop rate, the accidental coincidences are largely dominant over the background coming from RMD (which is linearly dependent on  $R_\mu$ ). It is then clear from Eq. (1) and (2) that, for fixed experimental resolutions, the muon stop rate cannot be increased too much but it must be chosen in order to keep a reasonable signal over background ratio.

In Fig. 4 the event distribution in the  $E_e$  vs  $E_\gamma$  and  $t_{e\gamma}$  vs  $\cos \Theta_{e\gamma}$  plane for data acquired in year 2009 and 2010 are shown in a region where the possible signal is expected. The (accidental) background extends into the signal region. This implies that the sensitivity of the experiment will not increase linearly with the statistics. The upper limit (90% C.L.) of  $2.4 \times 10^{-12}$  on  $\mu^+ \rightarrow e^+\gamma$  published by MEG in year 2011 is the present best experimental result on this decay. Based on this result we estimate to reach a sensitivity  $\sim 6 \times 10^{-13}$  in the middle of year 2013 and then stop data taking due to the limited statistical significance of a further continuation.

There are three other cLFV channels, in competition with  $\mu \rightarrow e\gamma$ , which are currently being actively considered:  $\mu \rightarrow e$  conversion,  $\mu \rightarrow eee$  and  $\tau \rightarrow \mu\gamma$ .

In  $\mu \rightarrow e$  conversion experiments negative muons are stopped in a thin target and form muonic atoms. The conversion of the muon into an electron in the field of the nucleus results in the emission of a monochromatic electron of  $\simeq 100 \text{ MeV}/c$ . Here the backgrounds to be rejected are totally different from the  $\mu \rightarrow e\gamma$  case. The dominant ones are those correlated with the presence of beam impurities, mostly pions. In order to reduce these backgrounds the experiments planned at Fermilab (Mu2e)[2] and JPARC (COMET)[3] will use accelerators with bunched proton beams to produce muons. Since muonic atoms have lifetimes of the

<sup>2</sup> A usual selection criteria is to choose 90% efficient cuts on each of the variables ( $E_\gamma$ ,  $P_e$ ,  $\Theta_{e\gamma}$ ,  $t_{e\gamma}$ ) around the values expected for the signal: this criterion defines the selection efficiency to be  $\epsilon_s = (0.9)^4$ . This kind of analysis in which one counts the number of events within some selection cuts and compares the number found with predictions for the background is named ‘‘box analysis’’. The MEG experiments usually adopt much more refined analyses which take into account the different distribution of ( $E_\gamma$ ,  $P_e$ ,  $\Theta_{e\gamma}$ ,  $t_{e\gamma}$ ) for background and signal by using maximum likelihood methods.

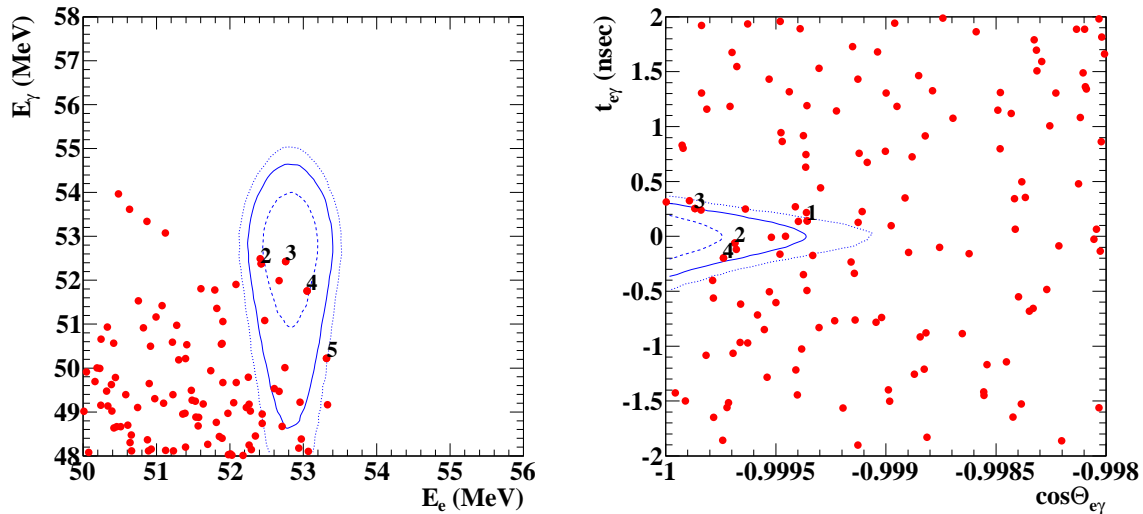


FIG. 4: Event distribution in  $E_e$  vs  $E_\gamma$  and  $t_{e\gamma}$  vs  $\cos\Theta_{e\gamma}$  planes. The curves shown are the 68, 90 and 95% probability contour levels for signal events. Events numbered are the ones having a largest probability of being signal rather than background

order of hundreds of nanoseconds conversion electrons will be searched for at times different from those of the bunches. These experiments can in principle reach sensitivities in the BR  $\mu \rightarrow e$  conversion below  $10^{-17}$ . The Mu2e experiment is now foreseen to start in year 2020 with a first phase goal of  $7 \times 10^{-17}$  sensitivity.

In a recent letter of intent presented to PSI[4] it is planned to perform an experiment to search for the  $\mu \rightarrow eee$  decay down to a sensitivity of  $10^{-15}$  (three orders of magnitude improvement with respect to the present best experimental limit) by utilizing the same beam line of MEG. In the second phase a new muon beam line with an increased muon stopping rate in the target ( $10^9 \mu/s$  instead of the  $10^8$  presently possible with the MEG muon beam line) could bring the experiment to reach a sensitivity of  $10^{-16}$ .

$\tau \rightarrow \mu\gamma$  will be explored at future high intensities B factories [5][6] where sensitivities of the order of  $10^{-9}$  to the BR for this decay will be possible.

A comparison between the sensitivity planned for the MEG upgrade and that envisaged for the other above mentioned cLFV processes will be discussed in the next section after a very short introduction on cLFV predictions in theories beyond the standard model.

### III. SCIENTIFIC MERITS OF THE MEG UPGRADE

The Standard Model (SM) practically forbids Lepton Flavour Violation in the charged lepton sector (cLFV). In fact even introducing massive neutrinos in the model, in order to account for the experimentally measured phenomenon of neutrino oscillations, the SM predicts a branching ratio ( $\mathcal{B}$ ) for  $\mu \rightarrow e\gamma$  below  $10^{-50}$ , which cannot be experimentally observed. cLFV processes are therefore clean channels to look for possible new physics beyond the SM. Although no experiment has until now observed any discrepancy from its predictions, the SM model is widely considered to be a low energy approximation of a more complete and general theory. Several candidates for such a theory, among which Supersymmetric Grand-Unified Theories (SUSY-GUT), predict cLFV with rates close to the present  $\mu \rightarrow e\gamma$  experimental upper limit. According to SUSY several low mass states should have been observed. However, these have not been discovered yet in energy frontier experiments and this represents one of the aims, unfortunately not yet reached, of the LHC program. Experiments looking for cLFV processes can provide another approach to clarify these theories since they are very sensitive to SUSY and particularly to SUSY-GUT models. In this sense, cLFV experiments are complementary to LHC in testing these theories. (see, *e.g.* Figure 5, where the sensitivity of  $\mu \rightarrow e\gamma$  to the high-energy scale is compared to direct LHC searches.)

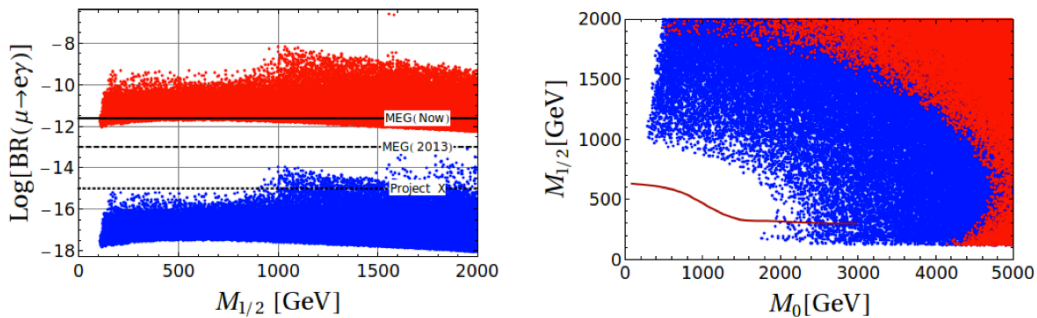


FIG. 5: Predictions of the  $\mu \rightarrow e\gamma$  decay rate obtained by scanning the mSUGRA parameter space, for  $\tan\beta = 10$  and  $U_{e3} = 0.11$ . The red points correspond to PMNS-like mixing, the blue ones to CKM-like. The figure on the right shows the allowed space in the  $m_0 - m_{1/2}$  plane which satisfies the current MEG bound. The region below the red line is excluded by the current LHC searches [7].

In such theories the mass matrix of the supersymmetric partners of the leptons (sleptons) is considered to be diagonal in flavour space at the Planck mass scale but radiative corrections in the renormalization group evolution from the GUT to the weak scale generate relevant non diagonal terms, giving rise to cLFV. So far two terms have been discussed . The first term considered comes from the fact that at the Planck

scale leptons and quarks belong to the same group representation (Grand Unification); radiative corrections induce large non diagonal terms in the slepton mass matrix owing to the heavy top quark mass [8]. The second term, which is independent from the previous one and adds up to it in contributing to the slepton mass mixing, therefore giving rise to cLFV, is linked to neutrino oscillations. The introduction of see-saw mechanisms to explain the neutrino mass pattern, with the addition of large mass right-handed neutrinos, in SUSY models gives rise to these non diagonal mass terms [9],[10].

Predictions of the  $\mu \rightarrow e\gamma$  branching ratio depend on the particular SUSY-GUT model taken into consideration and on the several other parameters of the theory such as the masses of the (yet unobserved) supersymmetric particles and the vacuum expectation values of the Higgs particles. However the requirement of constructing a stable theory without the need of fine tuning of the parameters implies that the new SUSY particles must have masses not much higher than 1 TeV. In this case most models predict that the sum of the two cLFV terms described above gives a predicted  $\mathcal{B}$  for  $\mu \rightarrow e\gamma$  larger than  $10^{-13}$ . This is shown for instance in Fig. 6 where the predicted  $\mu \rightarrow e\gamma$  branching ratio is shown as a function of the mass of the stau particle for values around 1 TeV in a SUSY-GUT model based on SO(10).

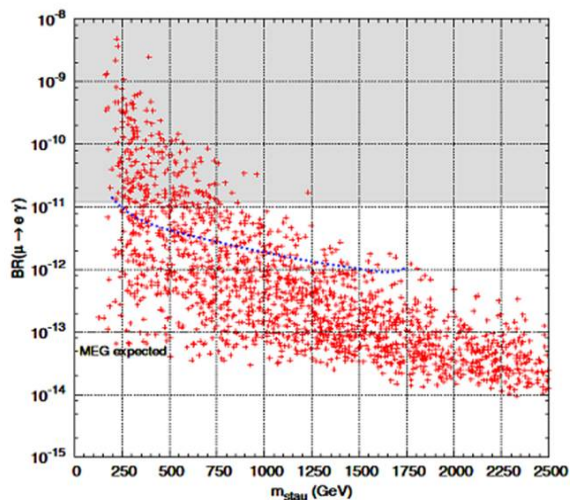


FIG. 6: SUSY-GUT SO(10) predictions for the  $\mu \rightarrow e\gamma$  decay [11].

In non-GUT SUSY models cLFV predictions are more dependent on parameters choices but the recent observations [12],[13],[14],[15] of a non vanishing value for  $\theta_{13}$  ( the mixing angle between the first and the third neutrino mass eigenstates, measured to be about 8.5 degrees) bring again models to predict large branching ratios for  $\mu \rightarrow e\gamma$ . This can be seen for instance in Fig. 7 where we show the predictions for  $\mu \rightarrow e\gamma$  vs for  $\tau \rightarrow \mu\gamma$  in a supersymmetric see-saw model [16] as a function of the largest of the masses of the right-handed neutrinos introduced and of  $\theta_{13}$ . This can be understood by the noting that  $\theta_{13}$  represents a

mixing between the first and the other generations of neutral leptons, which is mapped to a large mixing, in a model-dependent way, in the charged sector.

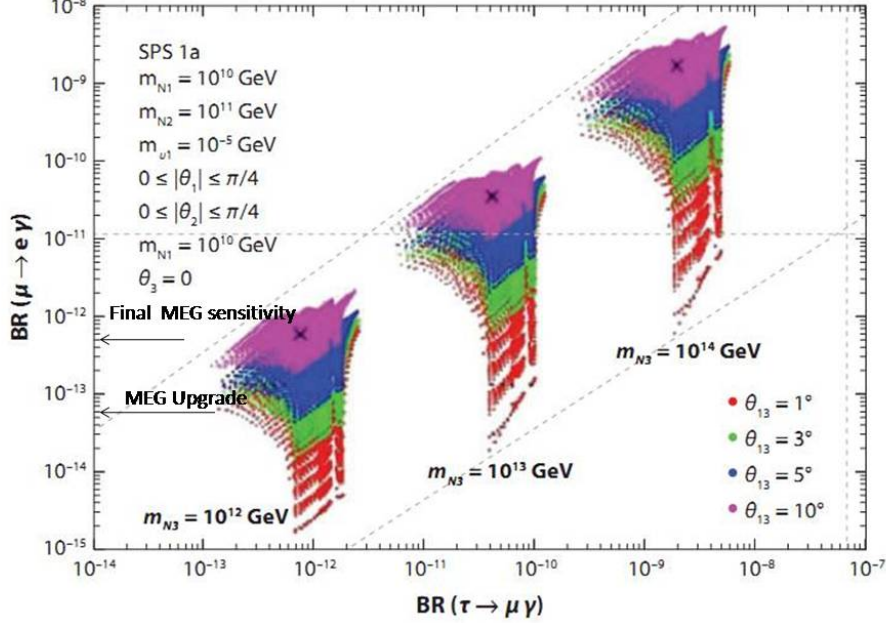


FIG. 7: SUSY see-saw model predictions for  $\mu \rightarrow e\gamma$  vs  $\tau \rightarrow \mu\gamma$ : see the text for an explanation

Another example of the predictions of a non GUT SUSY model[17] is shown Fig. 8, where again a plot of  $\tau \rightarrow \mu\gamma$  vs  $\mu \rightarrow e\gamma$  branching ratio is given. In this model only one of the squarks families is considered to have a mass in the TeV scale while the other two can have higher mass values as suggested by the most recent LHC measurements. The regions with different colour intensities correspond to points densities differing by one order of magnitude.

The sensitivity of the  $\mu \rightarrow e\gamma$  decay with respect to  $\tau \rightarrow \mu\gamma$  roughly ranges from 500 to  $10^4$  in SUSY-GUT models. This is not true in general for non-GUT SUSY models, as shown in Fig. 7, from which it seems that the sensitivity in the search for cLFV at future B factories, in some of these models, cannot compete with the sensitivity of the present proposal.

The comparison between  $\mu \rightarrow e\gamma$  versus  $\mu \rightarrow e$  conversion and  $\mu \rightarrow 3e$  is usually done in a model independent way by using the effective lagrangian[18]

$$\mathcal{L}_{CLFV} = \frac{m_\mu}{(\kappa + 1)\Lambda^2} \bar{\mu}_R \sigma_{\mu\nu} e_L F^{\mu\nu} + \frac{\kappa}{(\kappa + 1)\Lambda^2} \bar{\mu}_R \gamma_\mu e_L \bar{f} \gamma^\mu f \quad (3)$$

which contains two possible terms contributing to cLFV. In the second one  $f$  stands for the appropriate

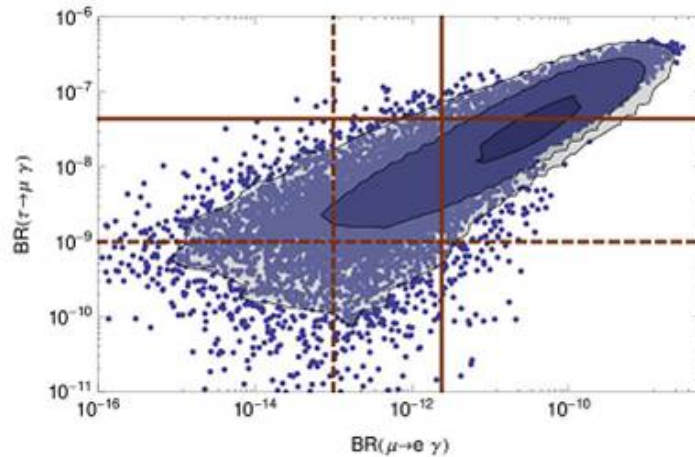


FIG. 8: SUSY see-saw model predictions for  $\mu \rightarrow e\gamma$  vs  $\tau \rightarrow \mu\gamma$ : see the text for an explanation

fermion field: the electron in the  $\mu \rightarrow 3e$  case or the relevant quarks in the  $\mu \rightarrow e$  conversion case. While  $\mu \rightarrow e\gamma$  proceeds only via the first term, corresponding to  $\kappa = 0$ , the  $\mu \rightarrow e$  conversion process and the  $\mu \rightarrow 3e$  decay may proceed also through the other one (large  $\kappa$  values). Fig. 9 shows the range of parameters in the  $(\kappa, \Lambda)$  plane which can be explored for the sensitivities that can be reached by  $\mu \rightarrow e$  conversion,  $\mu \rightarrow 3e$  or  $\mu \rightarrow e\gamma$  experiments. All the relevant SUSY - GUT models privilege the  $\kappa = 0$  term for which one can see from the figure that MEG is not only competitive with the second phase of the  $\mu \rightarrow 3e$  experiment but also, with a much shorter timescale and a far lower budget, with the first phase of the Mu2e project.

We finally care to note that the upgraded MEG will represent the best effort to address the search of the  $\mu \rightarrow e\gamma$  rare decay with the available detector technology coupled with the most intense dc muon beam in the world. We know that to achieve any significant improvement in this field several years are needed (one decade was necessary to pass from MEGA to MEG), and therefore we feel committed to push the sensitivity to the ultimate limits.

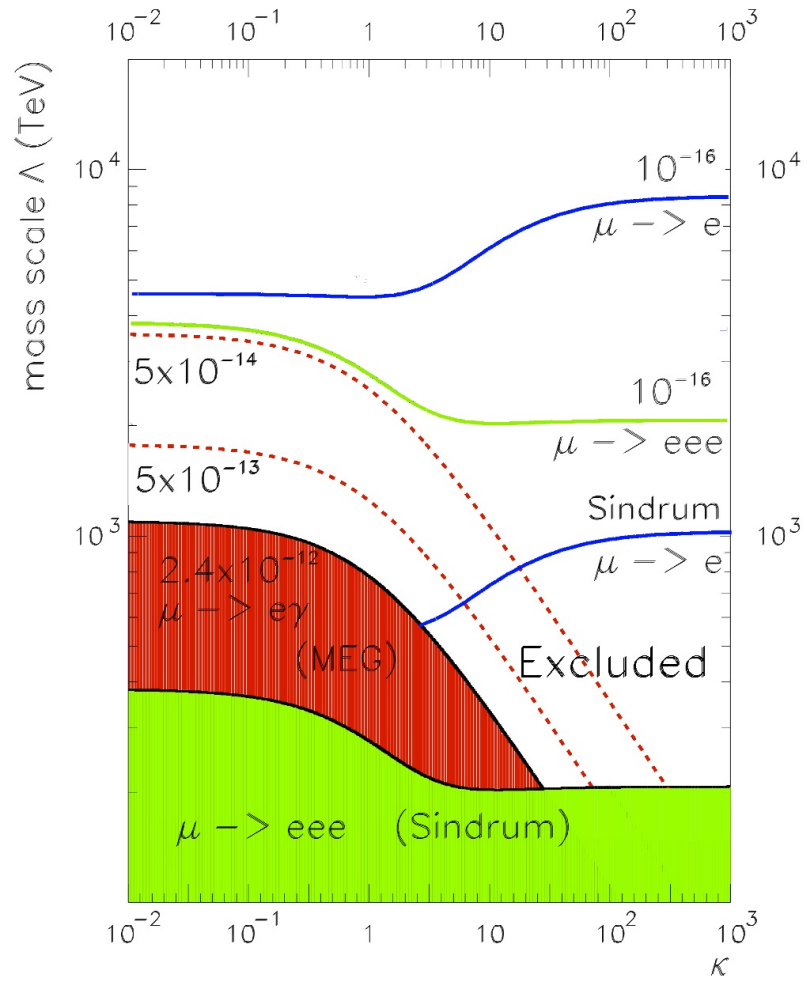


FIG. 9: the range of parameters in the  $(\Lambda, \kappa)$  plane that are explored by  $\mu \rightarrow e\gamma$ ,  $\mu \rightarrow 3e$  and  $\mu \rightarrow e$  conversion experiments (adapted from [2]).

## IV. UPGRADE OVERVIEW

### A. Key elements to a MEG upgrade

The MEG upgrade relies on the following improvements compared with the present MEG experiment, shown schematically in Figure 10 and discussed below:

1. Increasing the number of stopping muons on target;
2. Reducing the target thickness to minimize the material traversed by photons and positrons on their trajectories towards the detector;
3. Replacing the positron tracker, reducing its radiation length and improving its granularity and resolutions;
4. Improving the positron tracking and timing integration, by measuring the  $e^+$  trajectory to the TC interface;
5. Improving the timing counter granularity for better timing and reconstruction;
6. Extending the  $\gamma$ -ray detector acceptance;
7. Improving the  $\gamma$ -ray energy, position and timing resolution for shallow events;
8. Integrating splitter, trigger and DAQ while maintaining a high bandwidth.

### B. Discussion

A major improvement in the sensitivity to the  $\mu \rightarrow e\gamma$  decay requires a higher muon stopping rate and improved detectors efficiencies, to achieve a better single event sensitivity. This requires improvements to the experimental resolutions to proceed in parallel, to keep the accidental background low. The MEG measured resolutions and efficiencies are compared in Tab. I with the original MEG proposal.

While the photon detector and the timing counter almost met their requirements, the resolutions of the positron spectrometer are significantly worse than the design values, with consequences also on the relative  $e\text{-}\gamma$  timing.  $t_{e\gamma}$  in fact contains the length of the positron track from the target to the timing counter, as measured by the positron tracker.

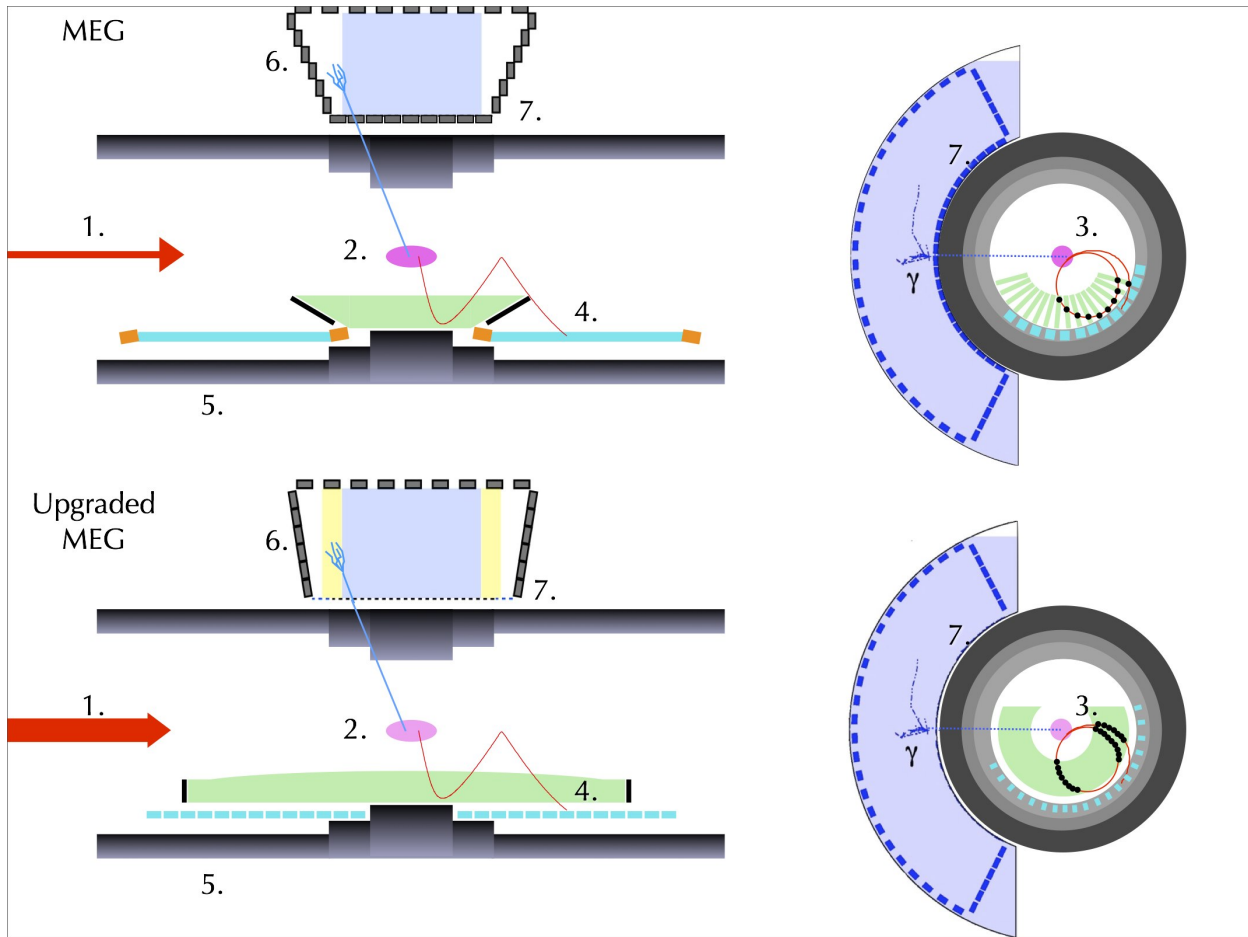


FIG. 10: An overview of the present MEG experiment versus the proposed upgrade. The numbers refer to the items listed in the text.

The photon detector showed somewhat degraded reconstruction capabilities for photons converting at the edge of its acceptance. Close to the entrance face the size of the 2" PMTs introduces a strong non-uniformity, while close to the lateral faces the PMTs introduce shadows in the acceptance. As explained in section VII a different solution is now envisaged for the front and lateral faces, to recover resolutions and efficiencies.

Furthermore there is also room for improving the tracker efficiency. The main part of the MEG tracking inefficiency is mainly due to the DC front-end electronic boards and mechanical support which intercept a large fraction of positrons on their path to the timing counters. The use of segmented cathode foils (Vernier pads) to reconstruct the  $z$ -coordinate was partially limited by the low amplitude of the induced signals on the cathodes, making the  $z$ -measurement more sensitive to the noise. The chamber operation presented some instabilities: their use in a high radiation environment led to ageing related problems, with discharges preventing their usage. This implied the impossibility of operating some of the chamber planes during part

Variable	Foreseen	Obtained
$\Delta E_\gamma$ (%)	1.2	1.7
$\Delta t_\gamma$ (psec)	43	67
$\gamma$ position (mm)	4(u,v),6(w)	5(u,v),6(w)
$\gamma$ efficiency (%)	> 40	63
$\Delta P_e$ (KeV)	200	306
$e^+$ angle (mrad)	5( $\phi_e$ ),5( $\theta_e$ )	8.7( $\phi_e$ ),9.4( $\theta_e$ )
$\Delta t_{e^+}$ (psec)	50	107
$e^+$ efficiency (%)	90	40
$\Delta t_{e\gamma}$ (ps)	65	122

TABLE I: Foreseen and measured resolutions for the MEG detector. In this Table  $\theta_e$  is the angle w.r.t. the  $z$ -axis (beam direction) and  $\phi_e$  is the angle in the transverse plane;  $u,v$  and  $w$  are local Cartesian coordinates that refer the photon position reconstruction to the liquid xenon detector ( $w$  represents the reconstructed photon conversion depth).

of the MEG runs.

We propose to build a new tracking chamber, designed to overcome the previous limitations, with improved efficiency, momentum and angular resolutions and capable of steady operation at high rates. The planned resolutions for the proposed tracker, together with a thinner stopping target (reported in section VI) lead to a substantial improvement in the determination of the positron kinematic variables.

In section V we show the prospects from upgrading the beam-target combination, with studies performed under different configurations of beam (surface/sub-surface) and target thicknesses, showing that a  $140 \mu\text{m}$  target at an angle of  $15^\circ$  with respect to the incoming surface muon beam is considered as the baseline solution for a three-years run.

We further propose to upgrade the liquid xenon detector to improve the photon acceptance, and its energy and position resolutions, by using a larger number of photo sensors with smaller dimensions, as described in section VII.

A new pixelated timing counter is described in section VIB, that can withstand the increased positron rate, with improved resolution in the  $t_{e\gamma}$  measurement,

The increased number of channels will be handled by a new mixed trigger/digitizer DAQ board (described in section VIII) maintaining the high bandwidth of the DRS analogue front-end.

### C. Auxiliary devices

The detector described so far represents the baseline design for the MEG upgrade. In parallel other R&D studies are being performed within our collaboration to study possible sensitivity improvements by complementing the measurements of positron and photon kinematic variables.

To further improve the positron angular and momentum resolutions an Active TARget (ATAR) and a Silicon Vertex Tracker (SVT) options are under study. A scintillation fibre-based active target (already independently financed) aims at tagging the incoming muons and the decay electrons with excellent position and timing resolutions. The silicon vertex tracker relies on an extremely innovative technology (high-voltage monolithic active pixel sensors, HV-MAPS) that is not yet mature.

A radiative muon decay counter (RDC) could also be used to tag low energy positrons associated with the high energy photons in the signal region. The existence of a companion positron would exclude a tagged photon from our signal candidate sample.

Those auxiliary devices, when beam tested and having demonstrated their usefulness without having significant impact on the background of the experiment, could then be accommodated in the experiment during the running phase.

These complementary and auxiliary devices will be described in detail in the appendix of the present document together with a tracker based on a different technology (a Time Projection Chamber). The TPC option was considered as a possible positron tracker at the early stages of this proposal, but its R&D turned out to be incompatible with the present proposal time scale.

Needless to say, all the calibration and monitoring techniques developed for the MEG experiment will be carried on also in the upgraded detector [19, 20]. Furthermore we plan to implement auxiliary calibration and monitoring techniques for the new tracker already at its design stage.

## V. BEAM LINE AND TARGET

### A. The MEG beam line and muon target

A schematic of the MEG beam line and the  $\pi E5$  channel is shown in Fig. 11. Driven by the world's most intense DC proton machines at the Paul Scherrer Institut's high-intensity proton accelerator complex HIPA, it constitutes the intensity frontier in continuous muon beams around the world (c.f. Table II) and as such, is capable of delivering more than  $10^8 \mu^+/s$  at  $28 \text{ MeV}/c$  to the MEG experiment. The surface muon beam has distinct advantages over a conventional 2-step pion decay-channel.

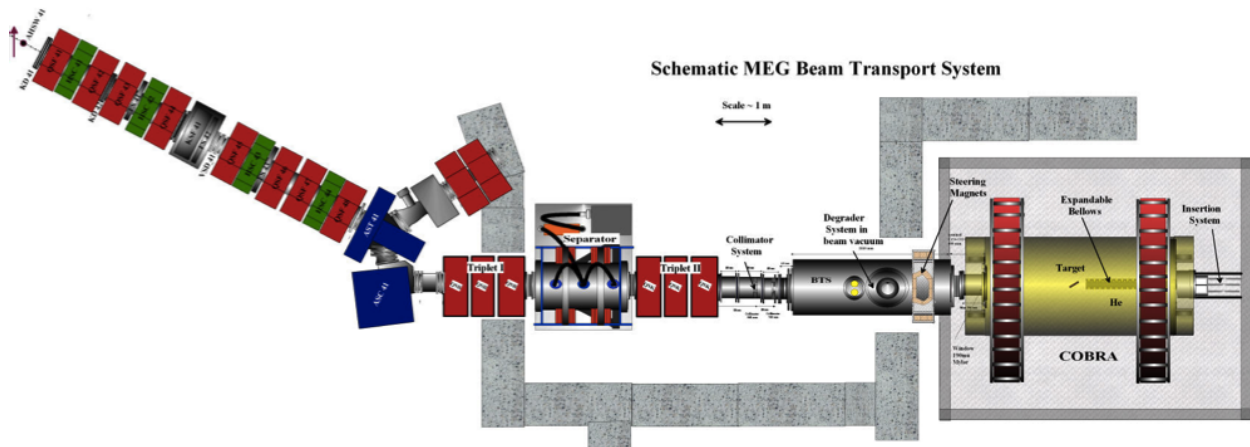


FIG. 11: (Left-part) shows the  $\pi E5$  channel, connecting the production target  $E$  to the  $\pi E5$  area. The MEG beam line starts from the extraction element Triplet I exiting the wall, followed by a Wien-filter, Triplet II and a collimator system, used to eliminate the beam contamination. The final range adjustment and focusing is performed by a superconducting solenoid BTS, before the muons are stopped in an ultra-thin target placed at the centre of the COBRA positron spectrometer.

The main beam characteristics are:

- High intensity
- Small beam emittance
- High-transmission optics for “ surface muons ”( $28 \text{ MeV}/c$ )
- Small, adjustable momentum-byte (less than 10% FWHM), implying a “ monochromatic” beam with a high muon stopping density
- Use of an ultra-thin, slanted muon target and minimization of material along the beam line (vacuum and He-environments) to reduce multiple scattering for both muons and Michel decay positrons as

TABLE II: Shows the currently running muon beam facilities around the world that are used for particle physics experiments and materials science  $\mu$ SR investigations. Also shown are the planned next-generation facilities designed for cLFV experiments, together with an estimate of their starting date. The PSI HiMB solution is currently only under study and is included purely for completeness.

<b>Laboratory/ Beam line</b>	<b>Energy/ Power</b>	<b>Present Surface <math>\mu^+</math> rate (Hz)</b>	<b>Future estimated <math>\mu^+/\mu^-</math> rate (Hz)</b>
<b>PSI (CH)</b>	(590 MeV, 1.3 MW, DC)		
LEMS	”	$4 \cdot 10^8$	
$\pi E5$	”	$1.6 \cdot 10^8$	
HiMB	(590 MeV, 1 MW, DC)		$4 \cdot 10^{10}(\mu^+)$
<b>J-PARC (JP)</b>	(3 GeV, 1 MW, Pulsed) currently 210 KW		
MUSE D-line	”	$3 \cdot 10^7$	
MUSE U-line	”		$4 \cdot 10^8(\mu^+)$ (2012)
COMET	(8 GeV, 56 kW, Pulsed)		$10^{11}(\mu^-)$ (2019/20)
PRIME/PRISM	(8 GeV, 300 kW, Pulsed)		$10^{11-12}(\mu^-)$ (> 2020)
<b>FNAL (USA)</b>			
Mu2e	(8 GeV, 25 kW, Pulsed)		$5 \cdot 10^{10}(\mu^-)$ (2019/20)
Project X Mu2e	(3 GeV, 750 kW, Pulsed)		$2 \cdot 10^{12}(\mu^-)$ (> 2022)
<b>TRIUMF (CA)</b>	(500 MeV, 75 kW, DC)		
M20	”	$2 \cdot 10^6$	
<b>KEK (JP)</b>	(500 MeV, 2.5 kW, Pulsed)		
Dai Omega	”	$4 \cdot 10^5$	
<b>RAL -ISIS (UK)</b>	(800 MeV, 160 kW, Pulsed)		
RIKEN-RAL		$1.5 \cdot 10^6$	
<b>RCNP Osaka Univ. (JP)</b>	(400 MeV, 400 W, Pulsed)		
MUSIC	currently max 4W		$10^8(\mu^+)$ (2012) means $> 10^{11}$ per MW
<b>DUBNA (RU)</b>	(660 MeV, 1.65 kW, Pulsed)		
Phasatron Ch:I-III		$3 \cdot 10^4$	

well as to reduce the probability of background photon production, such as annihilation-in-flight or Bremsstrahlung

- Minimization and separation of beam-related background, such as beam  $e^+$  from  $\pi^0$ -decay in the production target or decay particles along the beam line

The beam line layout (Fig. 11) consists of the  $\pi E5$  channel, a high-acceptance  $165^\circ$  backward directed quadrupole and sextupole channel connecting the main target  $E$  station to the  $\pi E5$  area. Coupled to this is

the MEG beam line starting with the set of extraction quadrupole magnets, Triplet I, exiting the shielding wall and allowing for an optimal high transmission through the Wien-filter ( $E \times B$  field separator). This together with Triplet II and a collimator system placed after the second triplet, separates the muons from the factor eight-times higher beam positron contamination coming from the target. A separation quality between muons and beam positrons of  $8.1 \sigma_\mu$  is achieved, corresponding to a 12 cm physical separation at the collimator system as shown in Fig. 12. This allows an almost pure muon beam to propagate to the superconducting transport solenoid BTS, which has a degrader system placed at its intermediate focus to minimize the multiple scattering contribution to the beam and to adjust the muon range for a maximum stop-density at the centre of muon target, placed inside a helium atmosphere, at the centre of the positron spectrometer.

The  $205 \mu\text{m}$  thick muon stopping target, an elliptical shaped sheet of polyethylene foil, sandwiched between a Rohacell foam-structured frame which maintains it in a vertical plane, has a major axis length of 200.5 mm and minor axis length of 79.8 mm and is placed at an angle of  $20.5^\circ$  to the beam axis. This allows, together with the  $300 \mu\text{m}$  thick degrader,  $190 \mu\text{m}$  vacuum window and the 1475 mm of helium gas, a maximal stopping efficiency of about 82%. A series of 10 mm diameter holes are also punched into the foil to allow an independent check of the planarity and target plane position from reconstructed tracks.

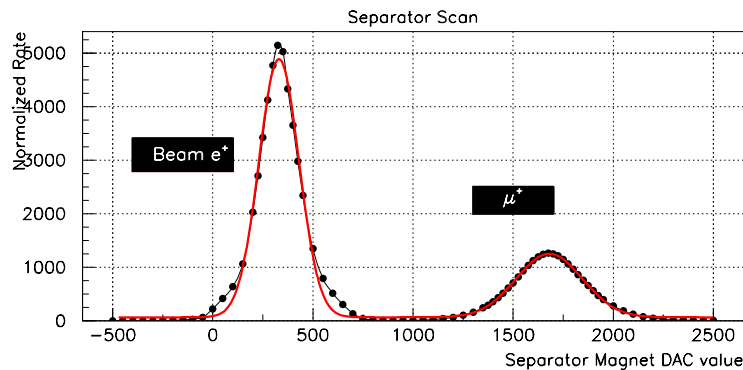


FIG. 12: Separator scan plot, measured post collimator system. The black dots represent on-axis intensity measurements at a given separator magnetic field value during the scan, for a fixed electric field value of -195 KV. The red curve represents a double Gaussian fit to the data points, with a constant background. A separation of  $8.1 \sigma_\mu$  muon beam  $\sigma$ s is found, corresponding to more than 12 cm separation of beam-spot centres at the collimator. The raw muon peak, measured at low threshold, also contains a contribution from Michel  $e^+$  due to decays in the detector, these can be eliminated by also measuring at high threshold

## B. Beam Line and Target Upgrade Potential

There also exists the potential of enhancing the sensitivity of the experiment by possible improvements to the beam line and target system. As already explained in section I, the optimal signal sensitivity for the current experiment is achieved for a muon stopping rate of  $3 \cdot 10^7$  Hz, approximately a factor of 3 lower than the maximal rate achievable. However, an increased muon rate must be accompanied by increased detector efficiencies, while at the same time minimizing accidental backgrounds by improving the experimental resolutions.

Several scenarios combining a higher beam intensity with various target thicknesses, ranging from a 250  $\mu\text{m}$  thick active scintillating fibre target down to a thin 100  $\mu\text{m}$  passive target version have been investigated. The former version not only has the potential of improving the positron momentum resolution but also improving the angular resolutions associated with the positron, mainly due to overcoming the multiple scattering restriction of the vertex determination on the target plane when back-projecting the track. A detailed status of the Active-Target study ATAR is given later. Also, the use of a lower momentum “sub-surface” muon beam in combination with the various target types was investigated. For a thicker target, this would allow the possibility of tuning the muon straggling distribution to minimizing the multiple scattering of the out-going positrons, while in the case of thinner targets a higher stopping quality (target stops versus ranging-out particles) could be achieved.

## C. Use of a Sub-surface Muon Beam

Surface muons [21], or low-energy muons derived from stopped pion decay close to the surface of the production target, have a unique momentum of 29.79 MeV/c due to the 2-body decay kinematics. However, due to the finite momentum-byte of the channel and the requirement to maximize the muon intensity, the central momentum is chosen to be approximately 28 MeV/c, thus selecting muons originating from a target surface layer of thickness equivalent to a few hundred microns. The range of such muons is of the order of  $120 \text{ mg cm}^{-2}$  and so must be degraded in order to stop them in an ultra-thin target.

The target thickness is governed by the requirements to have a maximal stopping density, i.e. maximal stopping rate in the thinnest possible target, while minimizing the multiple scattering and photon background production possibilities of the out-going positrons on the one hand and on the other, minimizing the amount of material seen by the photon travelling in the opposite direction. Hence these requirements are directly related to the amount of range-straggling of the muon beam. The total range-straggling is comprised of two components, one from energy-loss straggling of the intervening material, mainly the target, degrader,

vacuum window and He-gas and the other component being due to the momentum-byte of the beam. At these muon momenta ( $\sim 30$  MeV/c) the energy-loss component amounts to a constant contribution of about 9% of the range [21], while the range varies strongly with momentum  $P$  and is proportional to  $a \cdot P^{3.5}$ , where the factor “a” is a material constant. Hence the total range straggling is given by:

$$\Delta R_{TOT} = a \cdot \sqrt{((0.09)^2 + (3.5\Delta P/P)^2) \cdot P^{3.5}} \quad (4)$$

From Eq. 4 it can be seen that the most efficient way of reducing the straggling and hence the target thickness, is by reducing the beam momentum, rather than making the momentum-byte smaller. By reducing the beam momentum to 25 MeV/c, which constitutes a so-called “sub-surface” muon beam, since the muon acceptance layer in the production target now lies below the surface, as demonstrated by the measured muon momentum spectrum shown in Fig. 13.

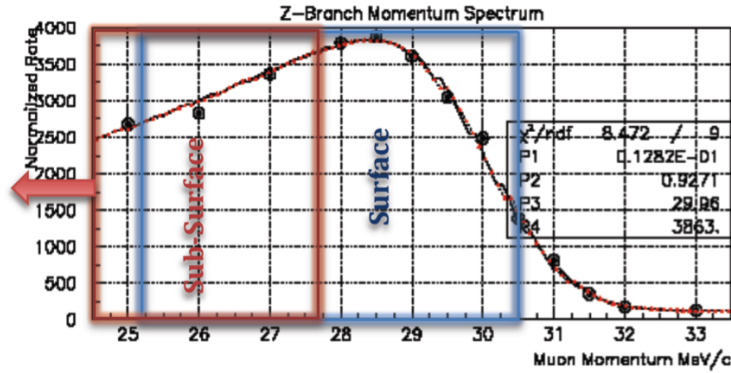


FIG. 13: Shows the measured muon momentum spectrum from the  $\pi E5$  channel with the momentum slits fully “open”. The red curve is a fit to the data of a theoretical  $P^{3.5}$ -distribution folded with a Gaussian resolution function corresponding to the momentum-byte plus a constant cloud-muon background. The blue and red boxes show the full momentum-byte for surface and sub-surface muons respectively.

This was obtained during commissioning by tuning the entire beam line to match the central momentum of each point. Here the momentum slits are fully “open”. The kinematic edge, smeared by the momentum resolution and defined by the momentum-byte can clearly be seen together with the characteristic  $P^{3.5}$  empirical behaviour of the spectrum towards lower momenta. The blue and the red (truncated) boxes show the full  $\pm 3\sigma$  momentum-byte for surface and sub-surface muons, respectively  $\pm 2.7$  MeV/c and  $\pm 2.5$  MeV/c. The spectrum fit shows that the muon rate also falls-off with  $P^{3.5}$  consistent with a more recent set of measurements made in  $\pi E5$  and summarized in Tab. III.

In order to take advantage of either reduced range-straggling and therefore a potentially thinner target, or the ability to optimize the position of the straggling distribution within a thicker target, a careful balance of

rate, sensitivity and background reduction are mandatory. The basic scenarios studied for a MEG upgrade strategy are summarized in Tab. IV and involved the use of either a surface or sub-surface muon beam with target thicknesses ranging from 100 - 250  $\mu\text{m}$ . The muon stopping numbers are from Monte-Carlo simulations based on real phase space measurements, while the target stopping rates are scaled from measured muon intensities.

TABLE III: Shows a series of beam measurements taken at the intermediate collimator position and at the centre of COBRA (CC), for a sub-surface muon beam of 25 MeV/c. No Degradator was used and the rates at CC are those of muons arriving at the centre, for a proton beam intensity of 2.0 mA.

Slit opening	Collimator position			COBRA center		
	$R_\mu$ (Hz) at 2mA	$\sigma_x$ (mm)	$\sigma_y$ (mm)	$R_\mu$ (Hz) at 2mA	$\sigma_x$ (mm)	$\sigma_y$ (mm)
250/280	$9 \cdot 10^7$	21.8	18.6	$7 \cdot 10^7$	9.6	10.1
115/115	$3.5 \cdot 10^7$	21.4	15.5	$2.9 \cdot 10^7$	8.9	8.8
70/70	$6.5 \cdot 10^6$	20.4	15.8	$5.8 \cdot 10^6$	8.4	8.3

TABLE IV: Monte-Carlo results for a Surface and Sub-surface muon beam + various target combinations based on a proton beam intensity of 2.3 mA.

Beam	Target Thickness ( $\mu\text{m}$ )	Target Angle (deg)	US (%)	Tg (%)	DS (%)	Stop Rate 2.3mA ( $\times 10^7\text{Hz}$ )	Stopping Efficiency (%)	Stopping Quality Factor SQF	Measuring Time (yrs)					
										Whole Target				
Surface	250	20.5	8.4	75.3	16.2	9.6	82.3	3.0	2.2					
Surface	205	20.5	7.2	65.9	26.8	8.4	71.1	1.7	2.5					
Surface	180	20.5	7.3	61.6	31.0	7.8	66.5	1.4	2.7					
Surface	160	20.5	9.3	57.5	33.2	7.3	63.4	1.2	2.9					
Surface	140	20.5	13.7	53.4	32.8	6.8	62.0	1.0	3.1					
Surface	100	20.5	23.6	41.8	34.5	5.3	54.8	0.6	4.0					
Surface	180	15.0	5.7	64.9	29.3	8.2	68.9	1.5	2.6					
Surface	160	15.0	7.6	62.3	29.9	7.9	67.6	1.3	2.7					
Surface	140	15.0	7.5	59.4	33.0	7.5	64.3	1.2	2.8					
Surface	120	16.0	9.7	52.8	37.4	6.7	58.6	0.9	3.1					
Sub-Surf	250	20.5	5.8	78.4	15.7	8.2	83.4	3.5	2.6					
Sub-Surf	205	20.5	5.3	70.2	24.3	7.3	74.3	2.1	2.9					
Sub-Surf	140	20.5	17.3	60.7	22.0	6.3	73.4	1.4	3.3					
Sub-Surf	100	20.5	32.5	47.8	19.7	5.0	70.8	1.1	4.2					
Sub-Surf	180	15.0	4.8	69.6	25.6	7.2	73.1	1.9	2.9					
Sub-Surf	160	15.0	5.5	66.6	27.8	6.9	70.6	1.6	3.0					
Sub-Surf	140	15.0	7.2	64.8	27.8	6.7	69.6	1.4	3.1					
Sub-Surf	120	16.0	9.7	59.1	31.0	6.1	65.6	1.1	3.4					

In summary, the results show that both surface and sub-surface beams yield solutions within a reasonable measuring time span of 3 years. The estimated stopping rate at a proton beam intensity of 2.3 mA is also

shown, as is the estimated running time for each scenario, relative to the baseline sensitivity goal solution of  $7 \cdot 10^7$  muons/s and three years of running. The stopping quality (SQF-factor), as defined in the table, is the ratio of target stops to stops elsewhere. As expected, a better stopping quality, in the case of a sub-surface beam is demonstrated in Fig. 14, which shows the relative virtue of each beam-target combination for muons stopping in the target compared to muons stopping elsewhere. As one goes to smaller target angle orientations ( $15^\circ$ ), shown by the dashed lines in the figure, a higher gain is achieved in the surface case compared to the sub-surface case.

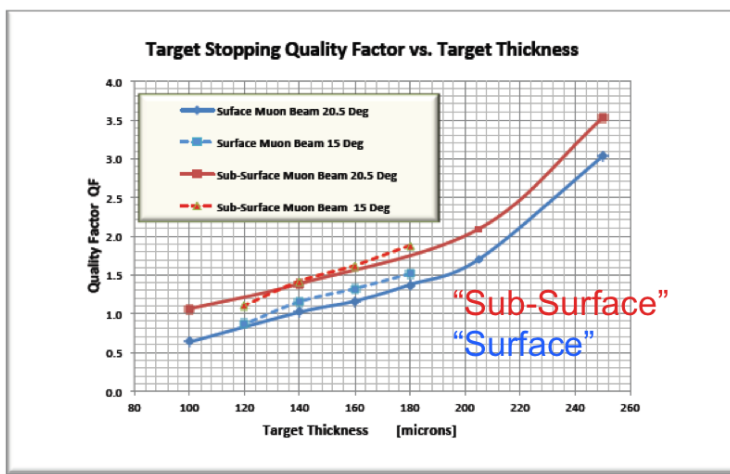


FIG. 14: Shows the stopping quality, a factor based on the maximization of the muon stops in the target and the minimization of potential background, caused by muons stopping elsewhere, for the case of a surface and sub-surface beam.

This can be understood since the sub-surface straggling width is closer to being optimal than in the case of the surface beam, such that the effect of going to smaller angles is larger for a surface beam. A further asset of the sub-surface muon beam is that the separation between muons and beam positrons in the Wien filter, as shown in Fig. 12, should also be enhanced due to the larger velocity difference.

In order to select a beam/target solution that will provide the optimal sensitivity many factors must be considered such as stopping-rate, which will influence the statistics, the central momentum and the momentum-byte, which determine the stopping distribution and optimal target size. This in-turn, dictates the amount of material encountered by both the in-coming muon and the out-going positron and photon. Restrictions of minimal multiple scattering and hence better positron tracking resolutions on the one hand and minimal probability for background photon processes such as annihilation-in-flight or Bremsstrahlung on the other, dominate the choice for a baseline solution for the MEG upgrade. This basically allows two possible solutions, achievable within a time of 3 years, namely:

- Surface Muon Beam, 140  $\mu\text{m}$  thick Target, placed at  $15^\circ$
- Sub-surface Muon Beam, 160  $\mu\text{m}$  thick Target, placed at  $15^\circ$

Until the full background simulations of the two scenarios have been compared in detail, the former surface muon beam version with the thinner target is taken as the baseline solution, for the reasons already mentioned.

## VI. POSITRON DETECTOR

The positron detector, shown schematically in Figure (15), consists of a low mass stereo drift chamber (DC) followed by a multi-tile scintillation timing counter (TC) for a precise determination of the particle momentum and production time.

Both detectors are placed inside COBRA, the gradient field magnet specifically designed for the MEG experiment. As in the MEG experiment the positron tracker is located at a large radius ( $r > 18$  cm) so low energy positrons are swept out of the magnet by the magnetic field without crossing the sensitive volume; positrons with momentum larger than  $\sim 45$  MeV/c, on the other hand, are tracked until they reach the TC tiles, with minimum presence of passive material.

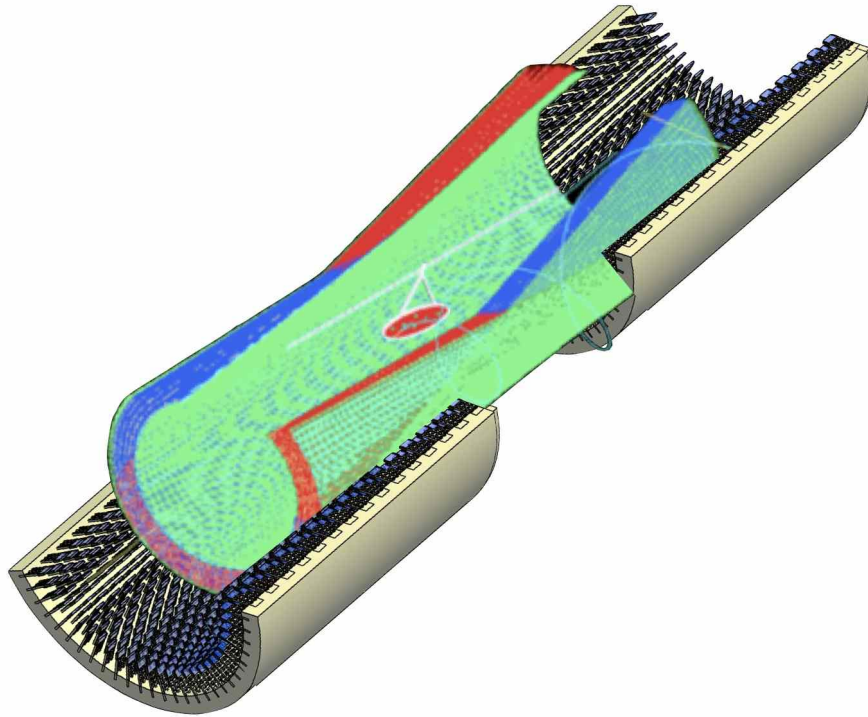


FIG. 15: Schematics design of the positron spectrometer

### A. The positron tracker

The positron tracker is a unique volume, cylindrical wire drift chamber, with the axis parallel to the muon beam, inspired by the one used in the KLOE experiment [22]. The external radius of the chamber is constrained by the available room inside COBRA, while its length is dictated by the necessity of tracking

positron trajectories until they hit the TC. This minimizes the contribution of the track length measurement to the positron timing resolution and increases the positron reconstruction efficiency avoiding any material along the positrons path to the TC. The requirements are satisfied for a chamber of  $\sim 180$  cm length.

The DC is composed of 10 criss-crossing sense wire planes with wires extending along the beam axis with alternating stereo angles in order to reconstruct the coordinate along the axis of the chamber by combining the information of adjacent layers. The stereo angle varies from  $8^\circ$  in the outermost layers to  $7^\circ$  in the innermost ones. There are alternate field planes and planes containing sense wires. The field planes are common to the two  $\pm$ stereo views and are stringed in both directions, creating a ground mesh between sense planes of alternating stereo view. In this way the chamber takes the shape of a rotation hyperboloid, whose surface is given by the envelope of the wire planes (see Fig. 16). Drift cells have an almost square shape (eight field wires surrounding the central anodic wire). The side of each cell is 7 mm in order to guarantee a tolerable occupancy of the innermost wires, which are placed at roughly 18 cm from the beam axis where the rate is  $\sim 1$  MHz for a stopping rate of  $7 \times 10^7 \mu/s$ . With a maximum drift time of  $\sim 150$  ns, *e.g.* with the same gas mixture of KLOE (He/Isobutane 90:10), this corresponds to a  $\sim 15\%$  occupancy of the innermost wires.

The distribution of cells inside the magnet volume is dictated by the angular coverage of the calorimeter. Fig.17 shows the pattern of anodic wires for three 52.8 MeV/c tracks originating from the target and with no momentum component out of the plane. The number of anodic wires is  $\sim 1200$  while the cathode wires are  $\sim 6400$ .

To minimize multiple scattering the DC runs with a low  $Z$  gas mixture. A (90:10) helium-isobutane (He: $iC_4H_{10}$ ) is presently foreseen, with the possibility to increase the isobutane fraction to meet the best compromise between track resolution and multiple scattering. In Tab. V we show the average contribution to the multiple scattering of the various materials for tracks contained in a plane perpendicular to the beam axis. The corresponding total number of radiation lengths for the new chamber is smaller to that of the current MEG drift chamber ( $\approx 1.7 \times 10^{-3} X_0$ ). This is crucial to keep the multiple scattering contribution to the momentum and angular positron resolutions under control, and also the rate of background photons in the electromagnetic calorimeter generated by positron annihilation in the chamber.

### 1. Mechanics

A first evaluation of the mechanical feasibility of the DC was done simulating, with a commercial Finite Elements Analysis program (FEA) [23], a model composed of two circular aluminum end-plates with an equivalent thickness of 20 mm (corresponding to a 30 mm end-plate with slots for PCB cards where wires

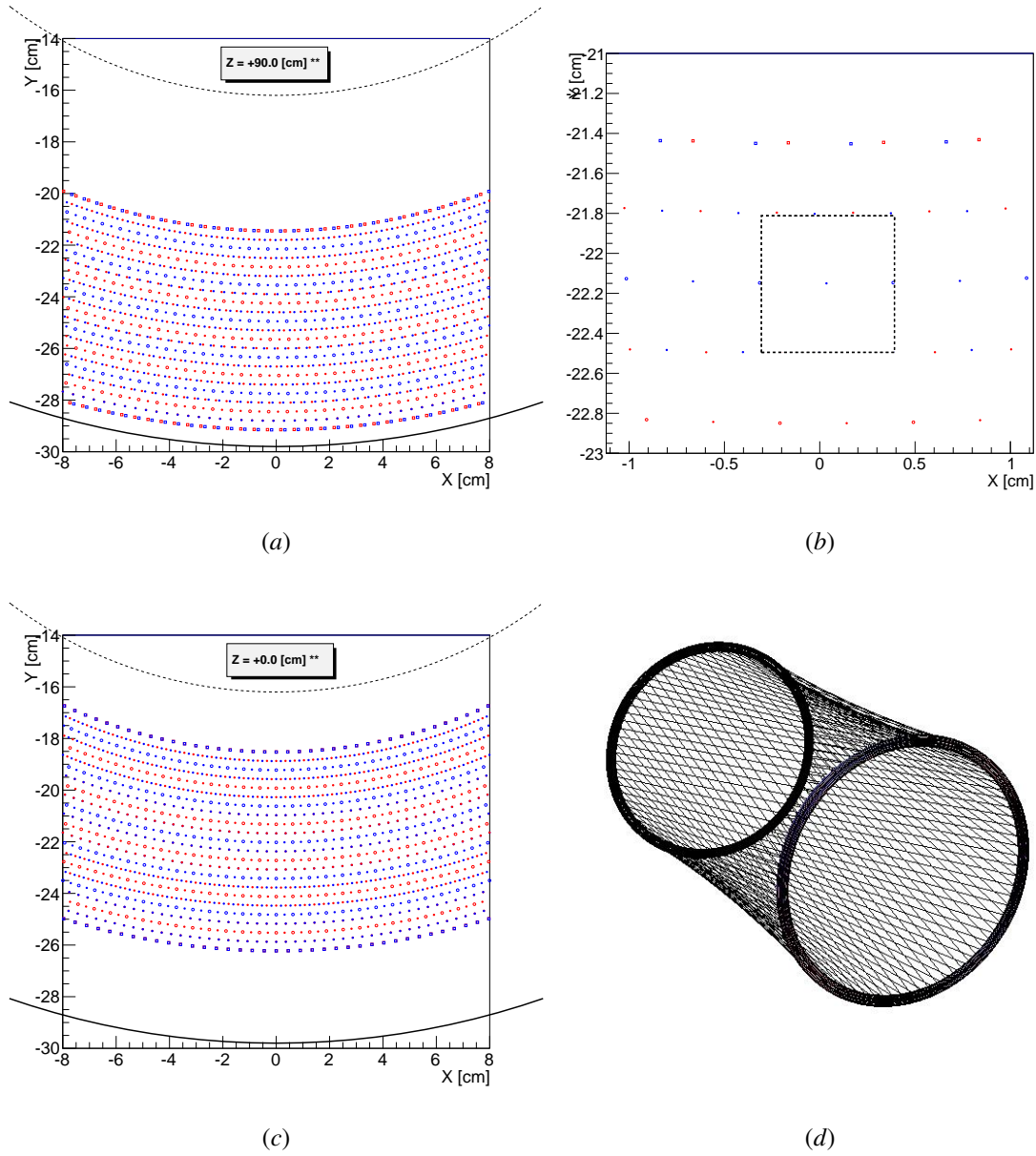


FIG. 16: Schematic distribution of field and anode wires in the proposed DC. Blue and red colors correspond to  $\pm$ stereo angles. Sense wires are drawn as open circles, while closed dots are field wires. Guard fields are depicted as square markers. (a) at the end-plate anchor point, (b) a zoomed version where a single  $7 \times 7 \text{ mm}^2$  cell is outlined. (c) the wire configuration at the centre of the COBRA magnet ( $z = 0$ ). (d) is a schematic representation of one of the hyperbolic mesh ground planes.

are soldered) kept in position by a 180 cm long, 2 mm thick, external carbon-fiber cylinder, made of 16 intermediate high-module (E460-MJ46) pre-preg layers, as in Fig. 18. Fig. 19 shows the simulation result when end-plates are loaded with a total wires pressure of 6000 N, uniformly distributed over  $300^\circ$  end-plate sectors. The maximum deflection is 0.37 mm which is tolerable given the stretching of the wires at

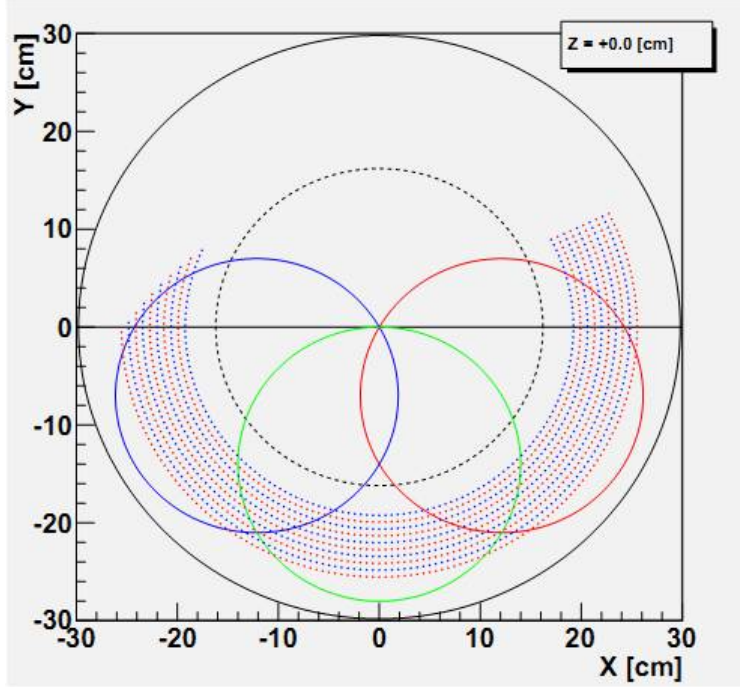


FIG. 17: The pattern of anodic wires with three tracks originating from the central target superimposed

Item	Description	Thickness ( $10^{-3}X_0$ )
Target	(140 $\mu\text{m}$ Polyethylene)	0.21
Sense wires	(25 $\mu\text{m}$ Ni/Cr)	0.16
Field wires	(40 $\mu\text{m}$ Al)	0.38
Protective foil	(20 $\mu\text{m}$ Kapton)	0.14
Inner gas	(Pure He)	0.06
Tracker gas	He/iBut. 85:15 (90:10)	0.50 (0.36)
Total	One full turn w/o target	1.24 (1.10)

TABLE V: Material budget of the new MEG drift chamber along one track. Note that the decay positron crosses only part of the polyethylene target. Two options for the gas composition are shown.

the proposed mechanical tension. In Fig. 20 it is also shown that the linear buckling of the carbon-fiber cylinder happens at about 85 times the nominal tension, indicating that distortions are kept within good safety margins.

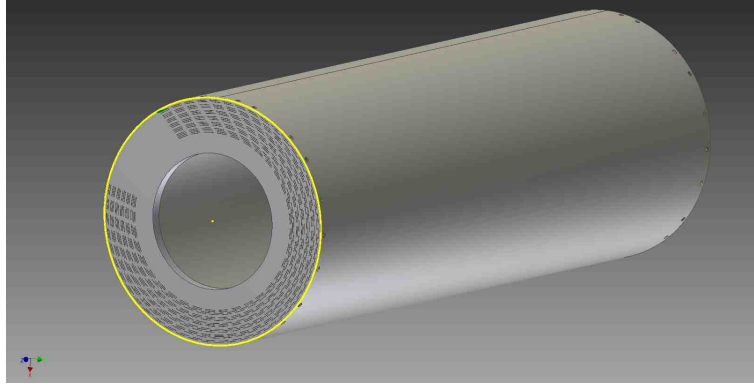


FIG. 18: Model of the new drift chamber used in FEA simulation

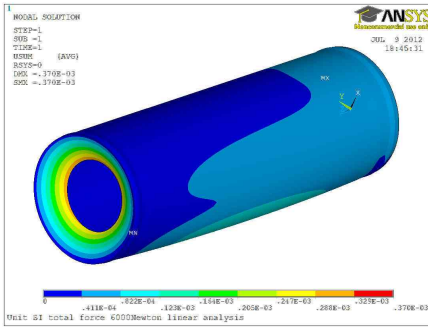


FIG. 19: Simulated end-plates deflection

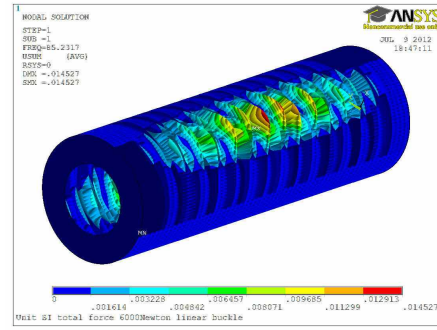


FIG. 20: Simulated cylinder linear buckling

## 2. Ageing tests

During the entire acquisition time of the upgraded MEG experiment the total charge collected by the innermost cells of the new DC was evaluated to be  $\leq 0.4$  C/cm for a gain of  $1 \times 10^5$  and a muon rate of  $7 \times 10^7 \mu^+/\text{sec}$  (see Table VI). This represents a huge amount of charge collected on anode and cathode and therefore a study of the DC ageing is mandatory. DC ageing induces gain loss, excessive chamber current, self-sustained discharges, sparking, high voltage instability, and it is thought to be predominantly caused by free radical polymerization [24]. In test set-ups ageing is usually accelerated by irradiating a DC prototype

$\mu^+$ rate = $7 \times 10^7 \mu^+/\text{sec}$	Maximum positron rate = 45 kHz/cm <sup>2</sup> at $10^8 \mu^+/\text{sec}$
Innermost Radius = 17.6 cm	Cell size = 7 mm <sup>2</sup>
DC gain = $1 \times 10^5$	Years of run = 3
DAQ days/year = 210	electrons/MIP $\approx 20/\text{cm}$

TABLE VI: Operating conditions for the DC of the positron tracker, used to evaluate the possible detector ageing.

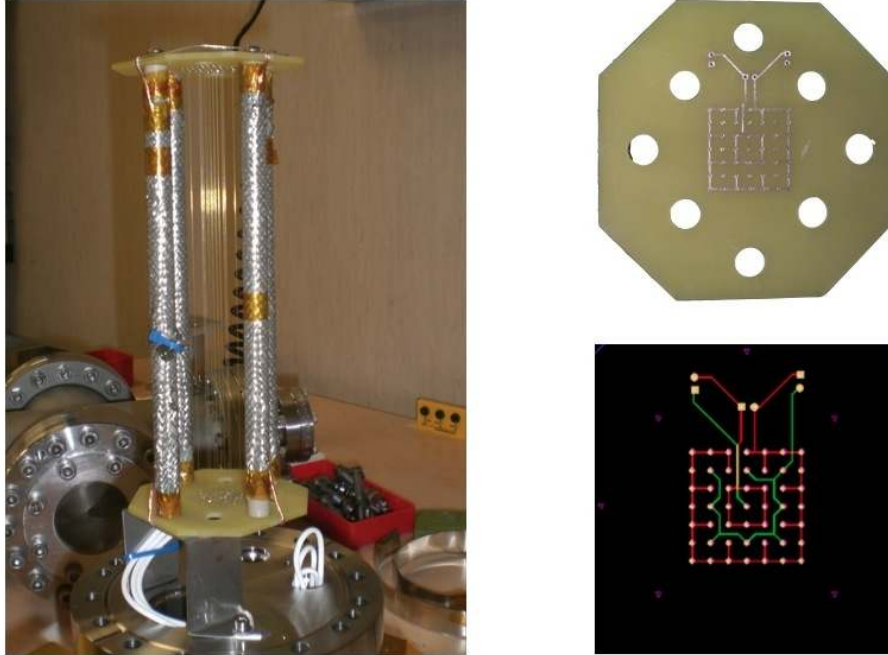


FIG. 21: DC prototype used for ageing test. The PCB and its layout are also shown.

with high intensity sources, and the chamber gain is monitored as a function of the total integrated charge.

A DC prototype of 20 cm length was prepared, which implements a single  $7 \times 7 \text{ mm}^2$  cell surrounded by field shaping wires that mimic the presence of all other cells. All wires are gold-coated tungsten wires; the central sense is  $25 \mu\text{m}$  diameter, the field and shaping wires are  $80 \mu\text{m}$  diameter (see Figure 21). An  $^{241}\text{Am}$   $\alpha$ -source of  $\sim 1 \text{ Bq}$  activity is placed on the prototype supporting structure to provide large ionization signals visible in the very light  $\text{He}:\text{iC}_4\text{H}_{10}$  mixture.

The DC prototype is placed in a stainless-steel chamber of 3500 cc volume, made of standard CF100 high vacuum components, equipped with HV and signal feed-throughs as well as two  $150 \mu\text{m}$  thin windows in order to let ionizing radiation through. The wires are soldered on a FR4 printed circuit board (PCB) and all internal connections other than the ones on the PCB are made with PTFE-coated coaxial cables. We work in a shifted-potential configuration, *i.e.* negative HV is applied to the field wires while the central (signal) wire is grounded through a Keithley 2635 picoammeter in order to read the DC current. The central signal can be also used to monitor the pulses seen by the DC. The measuring set-up is placed inside a lead/aluminum box for radiation safety.

A commercial MKS gas system was assembled to deliver the gas from bottles containing pre-mixed (90:10) helium-isobutane into the test chamber. The gas can be sampled by a residual gas analyzer (RGA) to monitor the gas composition at the percent level. Gas is flushed at  $50 \text{ cc/min}$  to provide a complete

volume exchange in one hour.

A 2.5 cm long portion of the central wire is irradiated with a MOXTEK Magnum 40 keV reflection source X-ray gun able to provide  $> 10^{11}$  X-rays/sec/sterad (see Figure 22 for a sketch of the measurement set-up). The stability of the source is monitored by means of a NaI X-ray detector preceded by a 0.6 mm diameter lead collimator. Its rate was measured to be linear with the X-ray source current.

Due to the lightness of our gas mixture most of the energetic X-rays go through the sensitive volume undetected. A fraction of X-rays ionizes the gas in the cell region and contributes to the DC current.

We conducted the ageing test at an initial DC current of 120 nA/cm, *i.e.* 20 times the maximum current foreseen in normal experimental conditions. This represents also the ageing acceleration factor: in ten days we collect the equivalent charge of one entire running year. We operated the DC prototype at  $-1250$  V

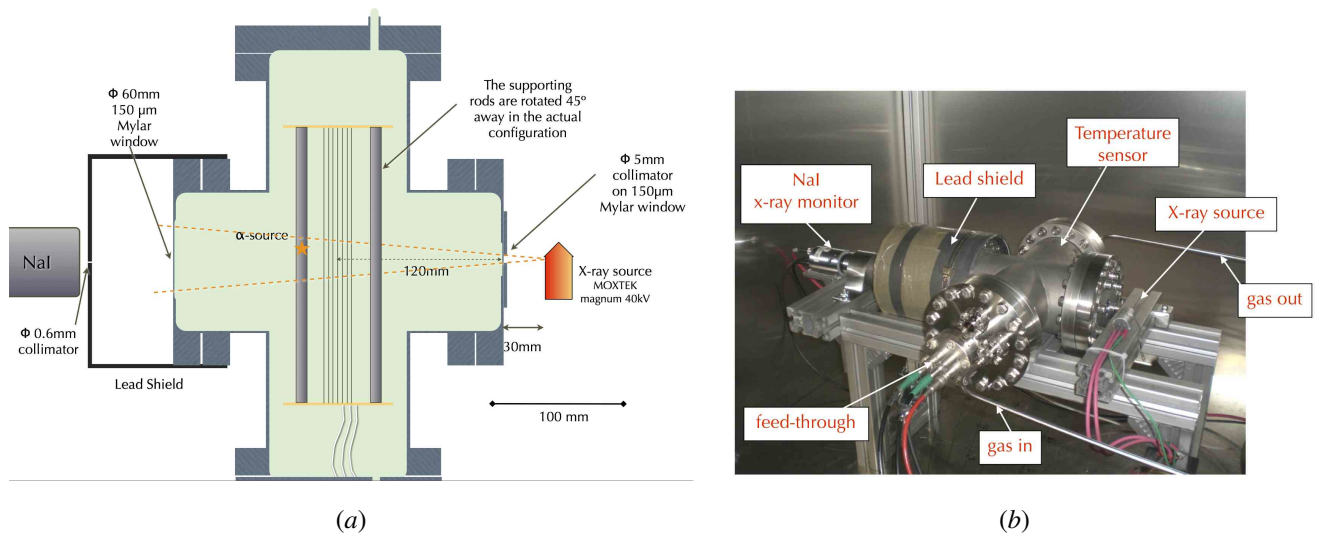


FIG. 22: Schematics (a) and picture (b) of the ageing measurement setup.

corresponding to a gain of  $\sim 10^4$ . X-rays and  $\alpha$ -particle signals are clearly visible on the oscilloscope with no need of preamplification. The prototype was irradiated for 15 days continuously, and Figure 23 shows the gain loss as a function of the time. Daily temperature oscillations induce a density variation which, in turn, is reflected in the gain oscillation observed. We measured the gain-density relation by modifying the system pressure (see Figure 23b) and applied the corresponding factor to correct the temperature-induced oscillations (black line in Figure 23a). Variations of the X-ray source were measured to be well below 1%. Every day we checked for possible sparks and discharges.

These preliminary tests showed that a yearly gain drop of  $< 25\%$  is expected at the hottest spot of the innermost DC wire; the large fraction of the DC is subject to a  $< 10\%$  gain drop per year (see Figure 24). This represents a good working point, where further optimization, such as material selection and different

gas flow rate, is possible.

### 3. Monte Carlo simulation

The response of the new chamber to 52.8 MeV/c positrons from  $\mu \rightarrow e\gamma$  decay was studied by means of a full Monte Carlo simulation program. We show in Fig. 25 the output of a simulated positron track in the spectrometer.

The most probable number of wires hits is  $\sim 60$ , a factor of 3 larger than the present MEG DC system.

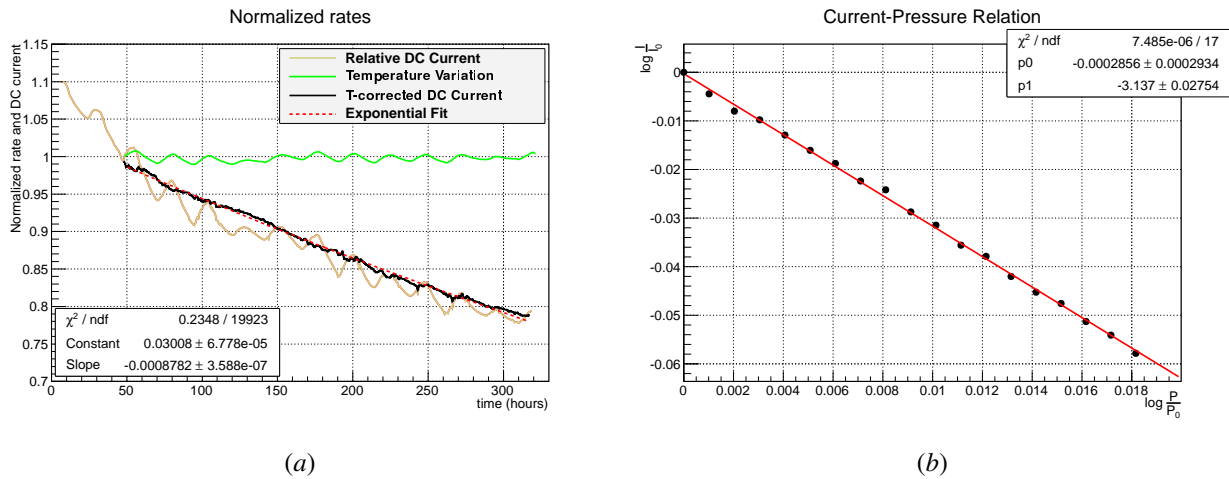


FIG. 23: (a) Variation of the current collected by the anode wire as a function of the time. 250 hours of accelerated ageing correspond to 1 PSI DAQ year. (b) The current-pressure relation used to correct for the temperature oscillations.

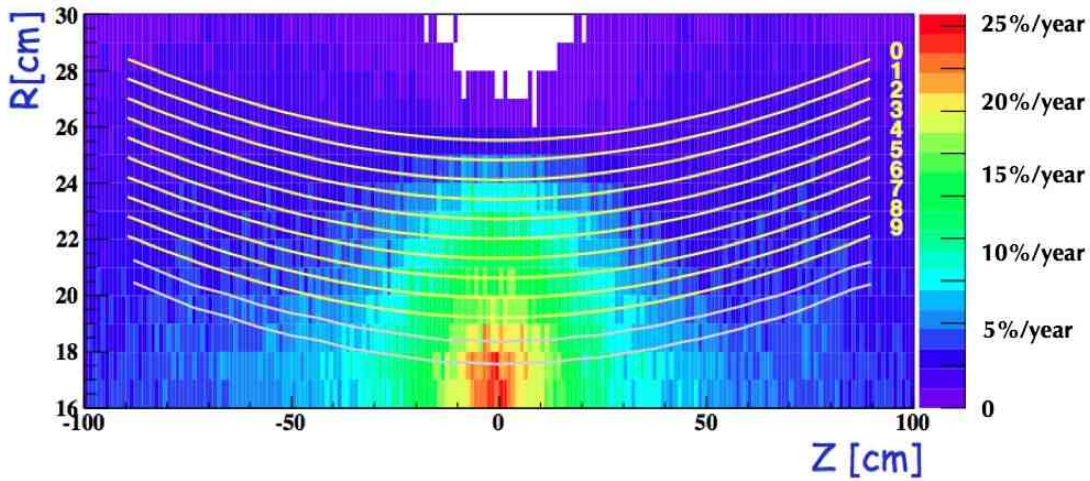


FIG. 24: Gain drop in 1-year od DAQ time at  $7 \times 10^7 \mu^+/\text{sec}$ .

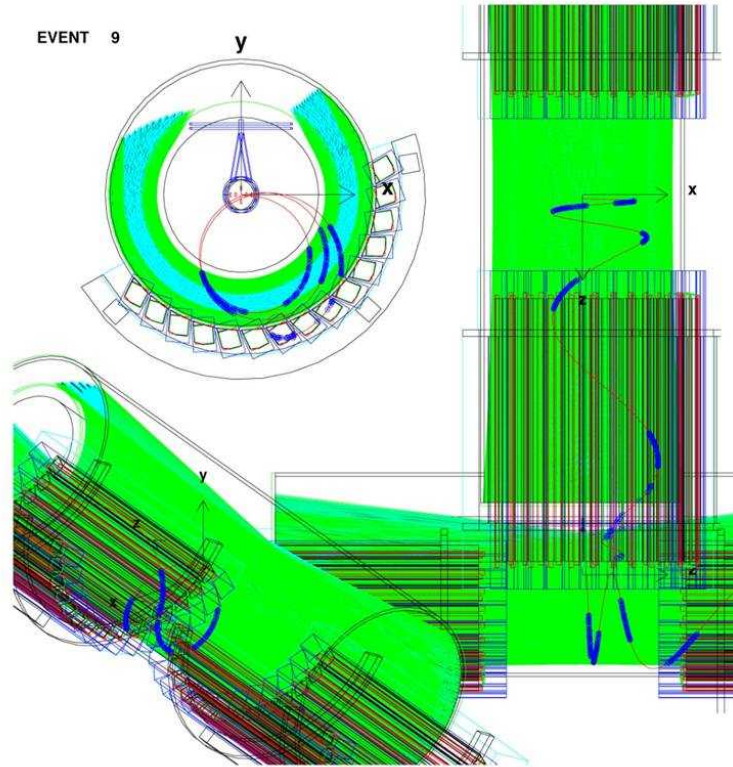


FIG. 25: Simulation of a 52.8 MeV/c positron track in the new drift chamber

This represents a big improvement for the reconstruction efficiency and for the momentum and angular resolutions, as well as a formidable help for pattern recognition in a high occupancy environment.

The resolution in the measurement of the drift distance to the anode wires is extrapolated from the measurements performed by the KLOE experiment [25] (which are shown in Fig.26) and confirmed by measurements in a test set-up (see section VIA 5). With reference to KLOE results in Figure 26, both the electronic (indicated as "electronic noise" in the picture) and the "primary ionization" components can be reduced by using a fast electronic chain and the "cluster timing technique" as explained in the next section. A preliminary hit reconstruction algorithm finds the point of closest approach to the wire, from the arrival time of the first avalanche cluster, with a resolution of about  $120 \mu\text{m}$  independently of noise level, while charge division gives the rough  $z$ -coordinate along the wire in the range  $1.3 \div 5.5 \text{ cm}$  with noise of  $1 \text{ mV} \div 3 \text{ mV}$  respectively. With this information, and the wire stereo angle, a simple track finder looks for groups of hits clustering into straight lines in the  $\phi$  vs  $z$  plane. The Hough Transform of the conformal X/Y mapping of the hit clusters found is used to remove outliers (see Fig. 27). We performed the tracks reconstruction by assuming an average resolution of  $120 \mu\text{m}$  in the measurement of the drift distance to the anode wires with a worsening similar to that in Figure 26 as a function of the impact parameter. The

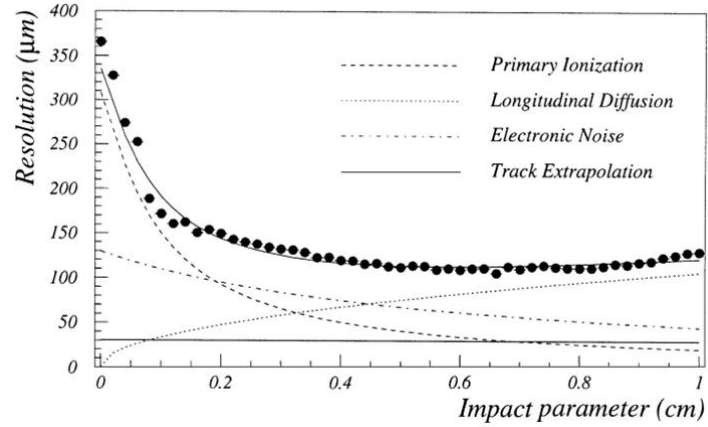


FIG. 26: Resolution on the drift measurement as a function of the impact parameter measured by the KLOE experiment [25]. The estimated individual contributions to the final measured values are shown in the picture.

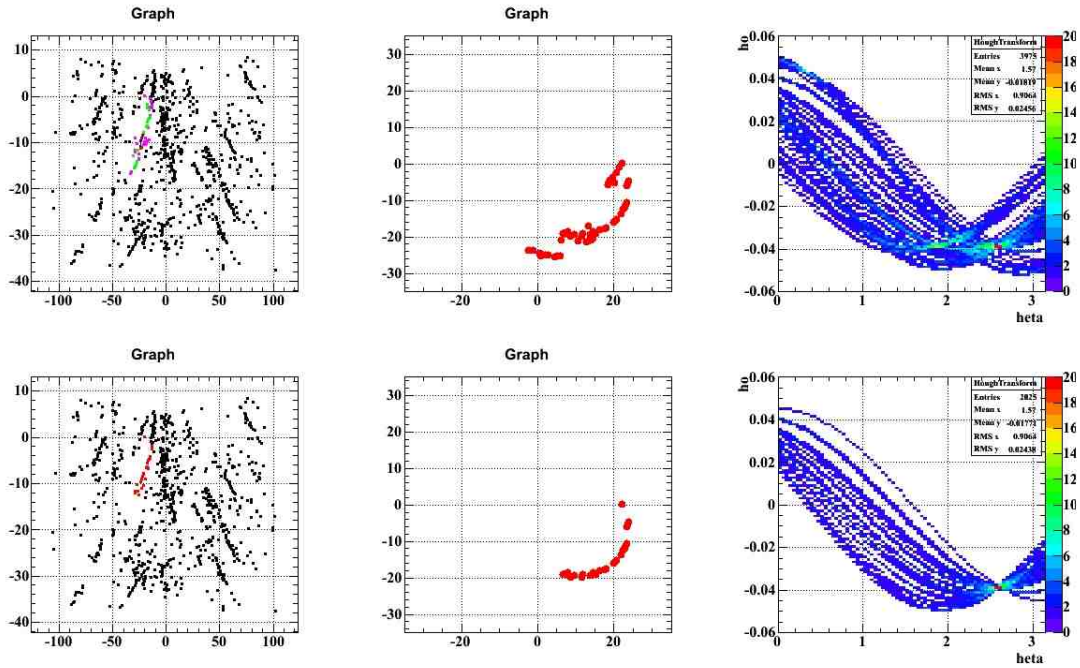


FIG. 27: A simple hit-finder, track-finder algorithm is capable of finding the signal track among the hits recorded in one event.

momentum and angular resolutions obtained from the simulation are:

$$\Delta\phi_e \Big|_{\phi=0} = 3.7\text{mrad}; \quad \Delta\theta_e = 5.3\text{mrad}; \quad \Delta P_e = 130 \text{ keV} \quad (5)$$

for a  $140 \mu\text{m}$  target thickness, with  $15^\circ$  slanting angle.

The positron reconstruction efficiency (tracks reconstructed in the DC with a corresponding hit on the

TC) is larger than 85% due to the chamber's ability to track the positrons up to the DC-TC interface. Furthermore read-out preamplifiers, cables and the structure supporting the wires are placed in regions which are off the positron paths (the efficiency is 40% for the present MEG positron spectrometer).

#### 4. Fast read-out and the cluster timing technique

The use of a low Z gas mixture such as He/Isobutane (90/10) is essential for minimizing the effects of multiple scattering. The average number of ionization clusters produced by the passage of a 52.8 MeV positron in this gas mixture is lower than in the present MEG DCs (about 12.5 per cm of track instead of  $\sim 30/\text{cm}$ ), leaving a bias in the measurement of the distance of closest approach (impact parameter) of a particle from the anode wire (see Fig. 28). We propose to use the cluster timing technique [26] to

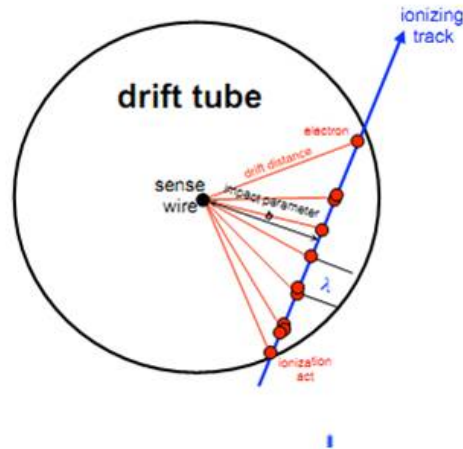


FIG. 28: Bias in the minimum distance measurement for low number of clusters per cm

eliminate this bias and aim at reaching possible resolutions even below the  $120\ \mu\text{m}$  previously assumed. This technique, as opposed to the traditional determination of the impact parameter, which uses only the arrival time of the first cluster, consists in measuring the timing of all the individual clusters and produce a bias free estimator using also the timing of the clusters following the first one.

The cluster counting/timing technique needs very fast frontend electronics for signal acquisition, the temporal separation between signals produced by the different ionizations clusters being a few nanoseconds; therefore, in order that the acquired signal shows temporally separated pulses without overlapping, it is necessary to have frontend electronics characterized by a large bandwidth. An analysis of the spectral density of signals, done using a single 8 mm diameter drift tube with a 90% – 10% mixture shows that signal bandwidth is on the order of 1 GHz [27]. Fig. 29 shows both a typical waveform acquired using

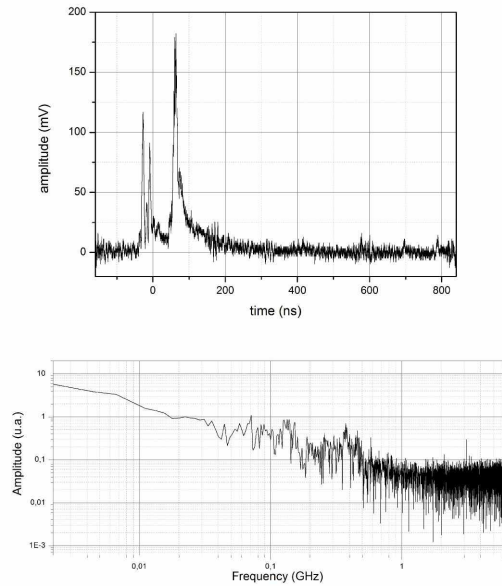


FIG. 29: Typical waveform (above) and Fourier transform (below) for an 8 mm diameter drift tube.

that detector and its Fourier transform. This result is used to set the overall bandwidth that the frontend electronics must ensure. We are developing a multistage low noise and low distortion frontend (Fig. 30)

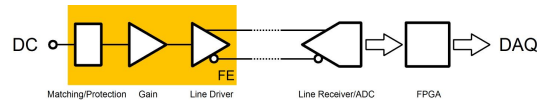


FIG. 30: Low noise and low distortion front-end scheme

that provides a total voltage gain on the order of 10 with a suitable bandwidth. The output of the frontend is differential to improve the noise immunity and is connected to the digitization stage through a twisted pairs line. To implement the frontend we use commercial components such as fast operational amplifiers that provide a gain-bandwidth product on the order of 1 GHz. Through a careful survey of available devices on the market, a preliminary frontend was developed using a low noise and low distortion high speed operational amplifier (AD8099 from Analog Devices) as the first stage and a wideband low noise and low distortion fully-differential amplifier (THS4509 from Texas Instruments) as the second stage/line driver. A schematic diagram of this frontend is shown in Fig. 31. A 3-channels frontend based on that schematic was assembled and tested using both signals from a pulse generator and from a setup of 3 aligned 8 mm diameter drift tubes 30 cm long (Fig. 32 left). With this setup an integral non-linearity  $< 1.5\%$  was measured (Fig. 32 right). In the usual operative conditions (90% – 10% mixture, 1.5 kV high voltage supply) the acquired

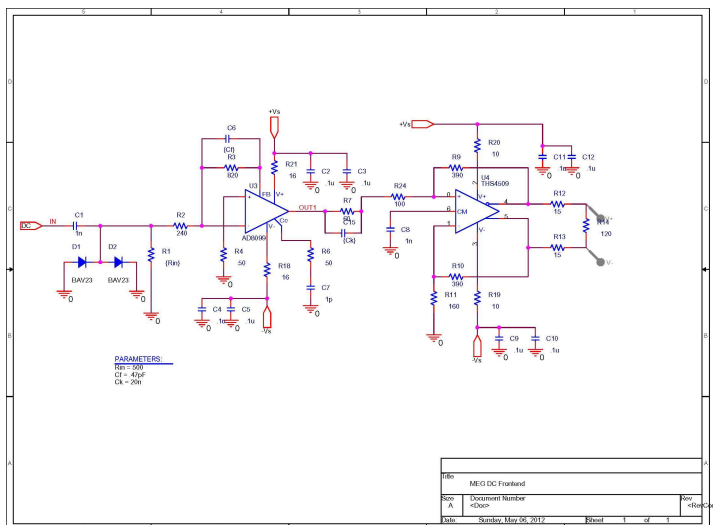


FIG. 31: Schematics of the front-end developed for the new MEG drift chamber

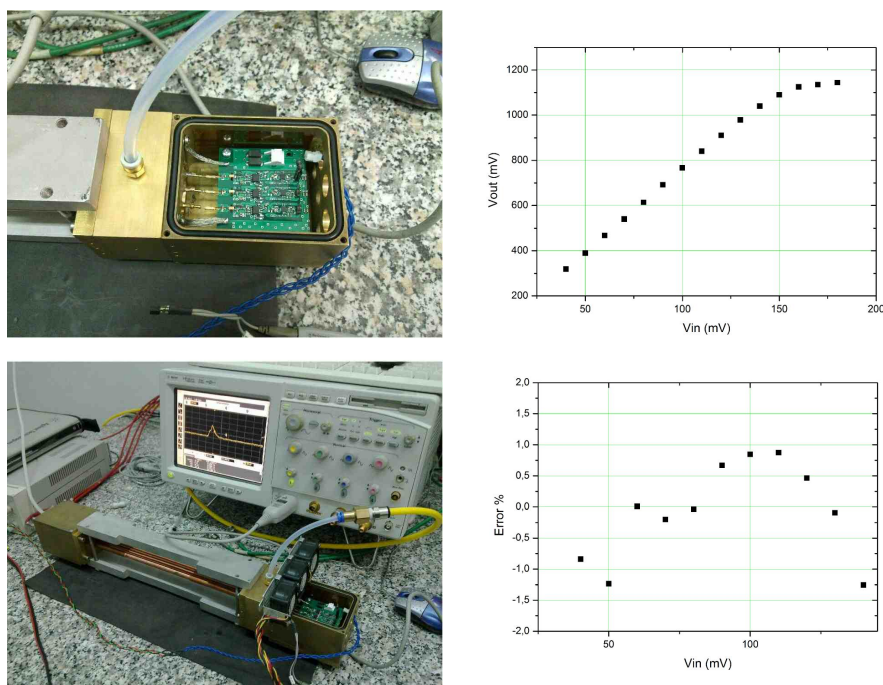


FIG. 32: Test set-up photograph (left) and measured non linearity (right) of the front-end prototype

signal shows a total drift time/number of clusters per pulse compatible with that expected ( $\sim 200 \div 250$  ns /  $\sim 10$ ) and an R.M.S. noise amplitude  $< 2$  mV (Fig. 33 left). A very compact version of PCB for that frontend with a 7 mm pitch, was designed (Fig. 33 right) and successfully tested.

The DRS digitizer, developed for MEG, which can work at digitizing frequencies up to 2.3 GHz, will be used for digitizing the chambers signal. Modifications of the current boards are necessary, as will be dis-

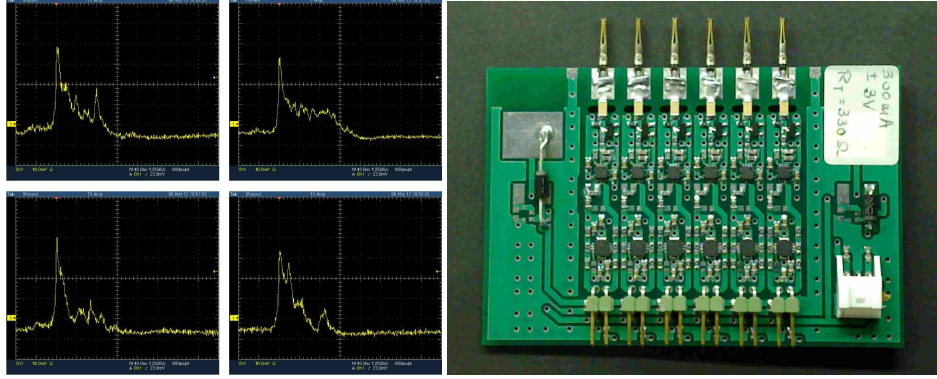


FIG. 33: Time distribution of clusters (left) and PCB (right) of the 6-channel front-end prototype

cussed in section VIII, in order to increase the input bandwidth, as requested by the cluster timing technique, and to cope with the increased number of channels needed by the upgrade.

#### 5. Tests for spatial resolution studies

The set-up in figure 32 was used to give an estimate of the spatial resolution attainable, as a function of the gas mixture. Three 8 mm drift tubes are vertically aligned, the central one being slightly displaced ( $\sim 500 \mu\text{m}$ ) on one side. In this configuration, for vertical cosmic rays, it is possible to show that the combination of the drift distances in the three tubes

$$\pm \Delta = (d_1 + d_2)/2 - d_2 \quad (6)$$

gives the displacement of the central cell up to a sign ambiguity due to the particle crossing trajectory with respect to the three anode wires (double-peak distribution). The width of the two peaks is related to the single hit resolution by the formula

$$\sigma_{\Delta} = \sqrt{\frac{2}{3}} \sigma_{\text{singlehit}}. \quad (7)$$

Figure 34 shows the double-peak distribution for two representative gas mixtures, while the single hit resolutions are reported in Table VII, where the contribution of multiple scattering on the CR muons from the copper tubes is included. The resolution ranges from  $150 \mu\text{m}$  for a 90 : 10 mixture to  $120 \mu\text{m}$  for a 75 : 25 mixture. In these measurements only information from the first cluster is used.

A larger prototype was designed and built to perform extended resolution studies: Its body is  $50 \times 20 \times 20 \text{ cm}^3$ , made of aluminum and hosts  $8 \times 8$  square cells (see Fig. 35) with 7 mm side. The top and bottom longitudinal sides of the prototype are made of  $50 \mu\text{m}$  Kapton windows to minimize multiple scattering effects. For each cell a  $25 \mu\text{m}$  gold plated tungsten sense-wire is surrounded by eight  $80 \mu\text{m}$  field

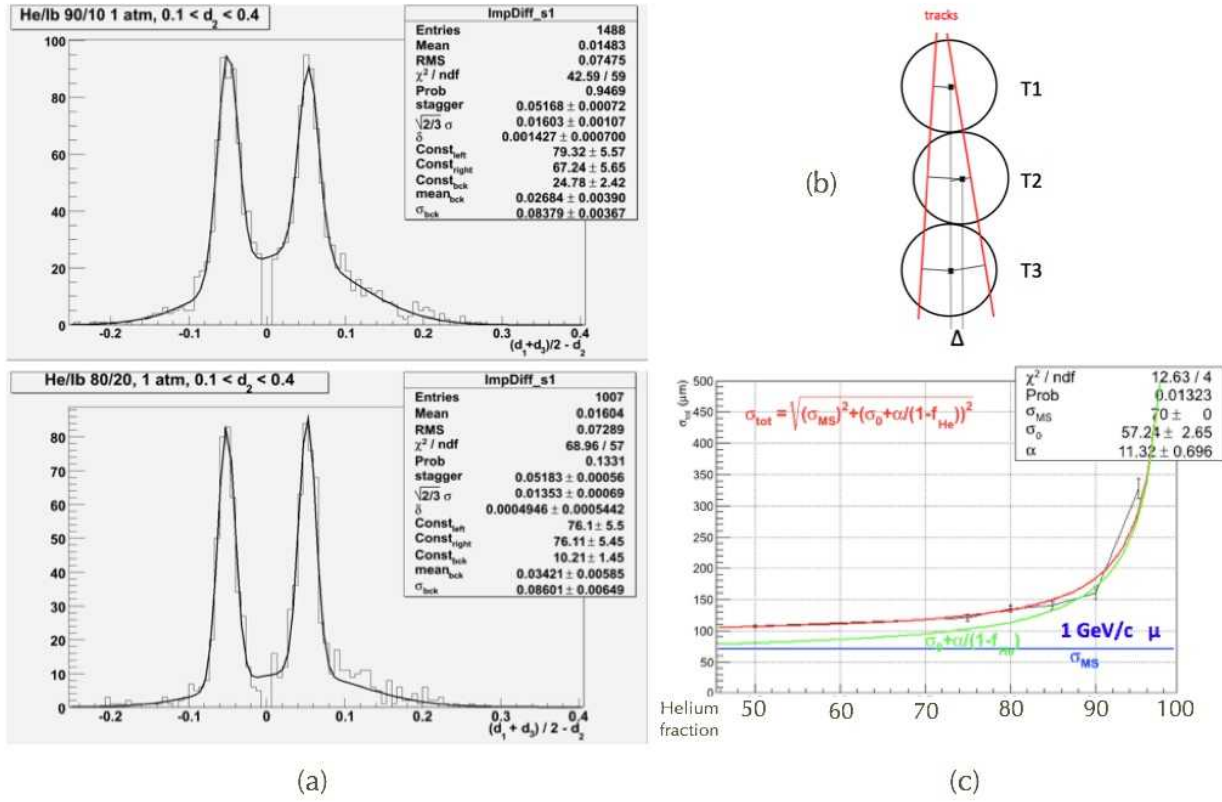


FIG. 34: (a) Distribution of the double peak in equation 6 for two representative gas mixtures. (b) A sketch of the three-tube set-up. (c) Statistical deconvolution of the contribution of multiple scattering on the three-tube set-up copper walls.

Mixture (He:iC <sub>4</sub> H <sub>10</sub> )	Resolution ( $\mu\text{m}$ )
5:95	$330 \pm 20$
10:90	$160 \pm 11$
15:85	$140 \pm 7$
20:80	$135 \pm 7$
25:75	$120 \pm 6$
50:50	$110 \pm 7$

TABLE VII: Summary of the resolutions obtained with the three-tube set-up. The single hit resolutions contain the contribution of CR multiple scattering on the four  $200 \mu\text{m}$  thick copper walls.

wires, also made of gold-plated tungsten. We use the sense wires feed-throughs made for the BaBar[28]

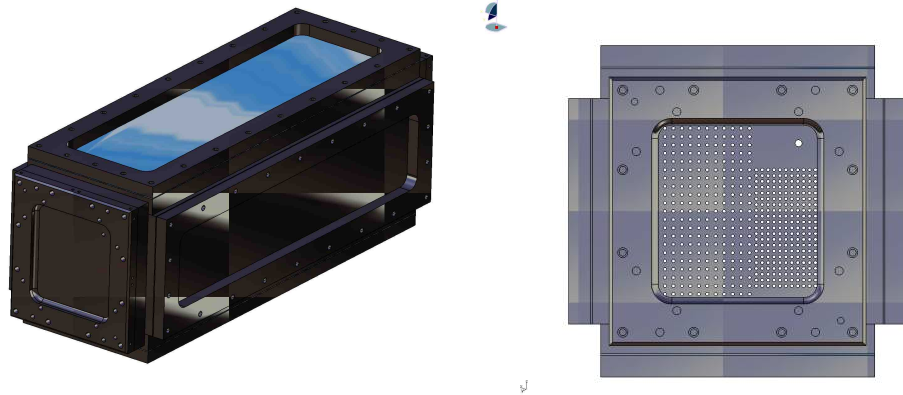


FIG. 35: the chamber body (left) and the end cap with the hole pattern (right)

drift chamber, whereas for the field wires, due to the limited space available, we designed new ones with smaller diameter (0.15 mm internal hole, 1.2 mm overall diameter) feed-throughs. Extensive studies on the achievable spatial resolutions with the proposed chamber geometry were made by using the GARFIELD package [29]. We plan to equip the central region of the detector with the newly designed high bandwidth readout electronics described in the previous section whereas the remaining wires will be read-out by using the KLOE electronics. Signals will be digitized by the MEG DRS digitizer.

In parallel, we are building a telescope for cosmic rays as a test facility of the performances of our prototype. This telescope consists, as shown in Fig.36, of an assembly of four double-side silicon layers of SVT, the former vertex detector of the BaBar experiment. With strip sizes of 50 and 100  $\mu\text{m}$  respectively for the transverse and the longitudinal view, this apparatus is suited to provide a reference for position reconstruction for the prototype detector. The single hit resolution is of the order of 20  $\mu\text{m}$  for the transverse and 40  $\mu\text{m}$  for the longitudinal view which correspond in the case of vertical crossing, to an accuracy  $\sim 10 \mu\text{m}$  (one order of magnitude better than the expected position resolution of the prototype detector) on the intercept of the cosmic ray tracks with the detector plane. Two Aluminum boxes, designed to provide proper servicing (clean air, temperature control, darkness) to silicon hybrids, host two layers each and are located above and beneath the test detector. To ensure adequate mechanical stability, these modules are stuck to a section-bar frame equipped with machine-controlled holes; this allows us to move the two boxes away, depending on the size of the detector prototypes, with comparable precision. The whole structure is eventually mounted on the top of a 15-cm thick granite table.

The trigger of through-going cosmic muons is accomplished by the coincidence of two scintillation counters, which are also used to provide the time reference for the measurement of the electron drift in

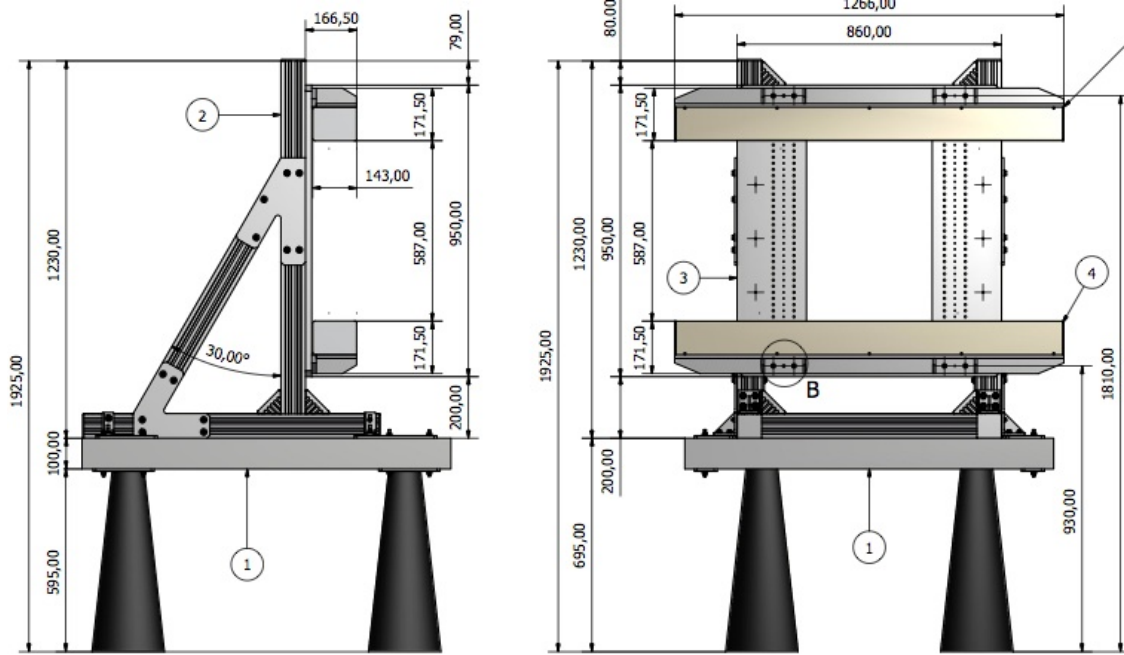


FIG. 36: Technical design of the telescope assembly for the test of detector prototypes.

every detector cell. An old-fashioned DAQ system, once used in BaBar to handshake with silicon hybrid chips, was replaced by custom designed boards (conceived as an interface with the hybrids) coupled with an acquisition front-end PC through commercial FPGA evaluation boards.

## B. Pixelated Timing Counter

### 1. Foreword and Status of the Art

The present timing counter showed an excellent intrinsic time resolution of 40 ps in beam tests before the experiment. The base design was based on multiple, tilted and parallel thick scintillator bars to make more uniform the response to circular positron tracks and improve the signature with multiple hits on contiguous bars. But, the best operating time resolution on the experimental floor has been measured to be worse, 65 ps, which includes the electronics time jitter. The main issues that cause this worsening are summarized below:

- the spectrometer magnetic field increases the PMT TTS (5%) and reduces the gain (up to factor 30): the consequent lower pulse amplitude causes larger time-walk effects: the statistical fluctuation of the residuals of the time walk corrections are calculated to contribute for about 20 ps;
- the scintillation pulse width is increased by the large  $z$  projection of the tracks that gives an excess

time spread of 20 ps;

- the electronic time jitter contributes for about 40 ps.

The sum of these contributions accounts for the above mentioned operating timing resolution. Further, since our PMTs work at the far edge of the performance vs. single event rate (1 MHz per PMT), the expected increase of a factor 3 of the muon decay rate requires a segmentation of at least the same factor with respect to the present design, i.e., 90 bars and 180 PMTs, in order to preserve the proper PMT working point. An improved concept of the upgraded timing counter that overcomes these limits must have:

- magnetic field insensitive photo-sensors with lower TTS and higher quantum efficiency;
- a design that is insensitive to the Z projection of tracks;
- a higher level of segmentation;

Here we present a new pixelated timing counter that meets these requirements.

## 2. *Concept of New Detector*

The pixelated timing counter is composed of two sets of semi-cylindrical shape scintillation detectors similarly to the current timing counter, but each detector is highly segmented as shown in Fig. 37. Each segment pixel is a small ultra-fast scintillator plate with silicon photomultiplier (SiPM) readout. There are a lot of advantages in this detector concept over the current timing counter as follows.

- The single plate is expected to have a good timing resolution since ambiguity in the positron path length inside the plate and also in the scintillation light propagation time to the photo-sensor is small. It should be noted that a good performance was already proved with a counter with a similar configuration in early studies for the PSI  $\mu$ SR detector [30][31].
- Most of the signal positrons passes through more than one pixels. Proper averaging of the times measured at the hit pixels gives more precise estimation of the positron impact time.
- The hit rate at each segment pixel is lower than 1 kHz even at a high beam rate of  $10^8 \mu/\text{sec}$ . The pileup probability is quite low.
- The multiple pixel hits can provide additional track information.

- For the current timing counter, a positron sometimes leaves double hits in a single timing counter bar, which produces a tail component in the timing response function. This problem will not happen in the pixelated timing counter.
- The proposed photo-sensor (SiPM) is insensitive to magnetic field. Note that the detector is placed in the bore of the spectrometer magnet COBRA.
- The detector is operational in the COBRA bore filled with helium gas in contrast to the current detector with PMTs, which is now housed in a helium-tight plastic bag constantly flushed with dry air.
- Flexible detector layout is possible since the position and angle of each pixel module can be adjusted individually.

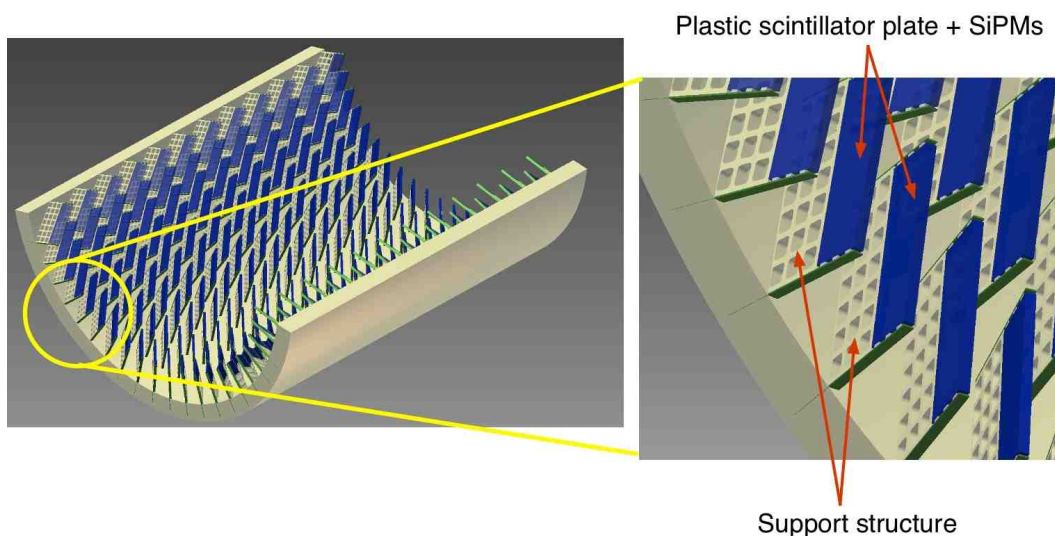


FIG. 37: Pixelated timing counter composed of many small scintillator plates.

### 3. Pixel Module Design

Fig. 38 shows a possible design of the single pixel module. The geometry of the scintillator plate is not fully optimized yet, but the typical dimension can be  $30$  (width)  $\times$   $90$  (length)  $\times$   $5$  (thickness)  $\text{mm}^3$ . The scintillation light is collected by three or four SiPMs at either end of the scintillator plate. The SiPMs at each end are connected in series and the summed signal is directly sent to a waveform digitizer module,

which is described in Sec. VIII. The positron impact time for the single pixel is obtained by averaging the times measured at both sides.

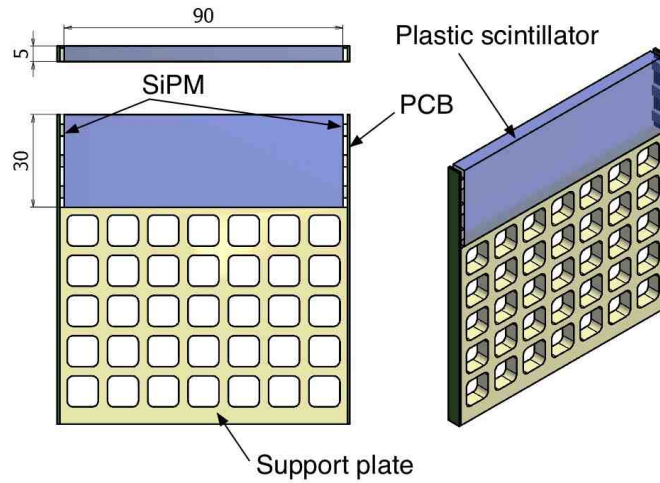


FIG. 38: Possible design of the single pixel module.

#### 4. Scintillator

The choice of the scintillator material is crucial to achieving the best time resolution. The parameters to be considered are light yield, rise time, decay time and emission spectrum of the scintillation. The possible candidates of the scintillation materials are the ultra-fast plastic scintillators from Saint-Gobain listed in Table VIII [32]. The scintillation light emission spectra are shown in Fig. 39 BC-422 would be the best for the timing measurement for a small size plate (shorter than several cm) because of its short rise time but with a relatively short attenuation length, while BC-418 or BC-420 would be better for a longer plate because of its longer attenuation length and higher light yield.

Single crystal *p*-Terphenyl is under study as another candidate for the scintillator material with potentially better timing performance, which is described in detail in Appendix XIII E.

#### 5. Silicon Photomultiplier (SiPM)

Silicon photomultiplier (SiPM) is a new type of semiconductor photo-sensor, which is considered as a possible replacement of the conventional PMT because of its excellent properties as listed below.

- Compact size

TABLE VIII: Properties of ultra-fast plastic scintillators from Saint-Gobain (BC-418, 420, 422) [32]. The properties of BC-404, which is used in the present timing counter bar, is also shown for comparison.

Properties	BC-418	BC-420	BC-422	BC-404
Light Output [% Anthracene]	67	64	55	68
Rise Time [ns]	0.5	0.5	0.35	0.7
Decay Time [ns]	1.4	1.5	1.6	1.8
Wavelength of Max. Emission [nm]	391	391	370	408
Bulk Light Attenuation Length [cm]	100	110	8	140

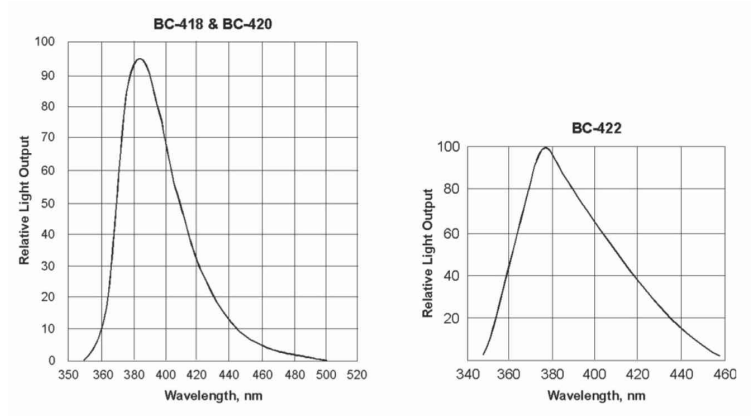


FIG. 39: Scintillation light emission spectra of Saint-Gobain BC418, BC420 and BC422 [32].

- Sensitive to single photon
- High internal gain ( $10^5$ – $10^6$ )
- High photon detection efficiency peaked at  $\lambda \sim 450$  nm
- Insensitive to magnetic field
- Low bias voltage ( $< 100$  V)
- Excellent time resolution ( $< 100$ ps for single photo-electron)
- low power consumption
- No avalanche fluctuation (excess noise factor  $\sim 1$ – $1.5$ )

TABLE IX: Specifications of Hamamatsu MPPC S10931-50P [33].

Active area	$3 \times 3 \text{ mm}^2$
Pixel pitch	$50 \times 50 \mu\text{m}^2$
Number of pixels	3600
Geometrical fill factor	61.5%
Peak wavelength	440 nm
Operating voltage	$70 \pm 10 \text{ V}$
Temperature coefficient of breakdown voltage	$56 \text{ mV}/^\circ\text{C}$
Gain	$7.5 \times 10^5$
Dark count rate	6 Mcps

It should also be the best solution to the scintillation readout for the pixel module of this detector. The candidates for the SiPM for the detector are Hamamatsu S10931-050P [33], FBK-AdvanSiD ASD-SiPM3S-P-50 [34], KETEK PM3350 [35]. The specifications of Hamamatsu MPPC S10931-050P are listed in Table IX as an example. The photon detection efficiency (PDE) as a function of wavelength is shown in Fig. 41, which is reasonably matched to the scintillation emission spectra of the Saint-Gobain plastic scintillator shown in Fig. 39.

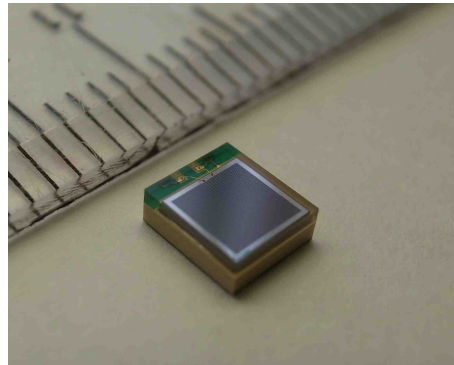


FIG. 40: Hamamatsu MPPC S10931-050P.

### 6. Support Structure

The requirement for the precision of the pixel alignment is not so severe. A precision of 1 mm, which correspond to the misalignment in time of a few ps, is good enough. Possible design of the support structure for the pixelated timing counter is seen in Fig. 37. Each pixel module is supported by a 5 mm-thick and

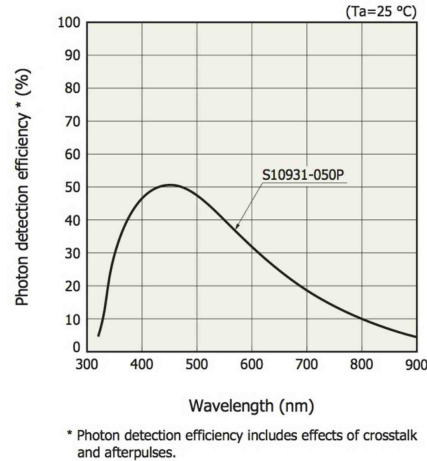


FIG. 41: Photon detection efficiency (PDE) as a function of wavelength for Hamamatsu MPPC S10931-050P [33].

40 mm-high plastic plate with the same length as the pixel module, which is fixed to a 40 mm-thick semi-cylindrical base made of plastic. Several holes are punched on the support plate to minimize undesirable multiple scattering of the positron. The possible candidate of the support structure material is Delrin plastic (polyoxymethylene).

### 7. Test with Pixel Counter Prototype

A good performance of a scintillator counter with a similar configuration was already demonstrated in the early studies for the PSI  $\mu$ SR facility [30][31]. Nevertheless, a couple of prototype counters are built in order to measure and to optimize the performance of the single pixel counter with the realistic configuration in our experiment.

Fig. 42 shows one of the prototype counters, where a plastic scintillator (BC422) of  $30 \times 90 \times 5 \text{ mm}^3$  is mounted in a supporting frame made of Delrin plastic. Three SiPMs, which are connected in series, are optically coupled to each end of the scintillator plate with optical grease (OKEN6262A).

A typical setup of the measurement is shown in Fig. 43. The prototype counter is irradiated by electrons from  $^{90}\text{Sr}$  with an energy up to 2.28 MeV. A counter with a small plastic scintillator (BC422,  $5 \times 5 \times 5 \text{ mm}^3$ ) readout by a single MPPC, whose timing resolution is measured to be 28 ps in  $\sigma$ , is placed behind the prototype counter for the triggering and the collimation of the electrons from  $^{90}\text{Sr}$ . The output signals from the two SiPM chains in the prototype counter are amplified with an optimum signal shaping in a voltage amplifier developed at PSI and are then readout by a waveform digitizer (DRS4), which is also in-house developed at PSI [1]. In the final detector the signals from the pixel counters are transmitted with a coaxial

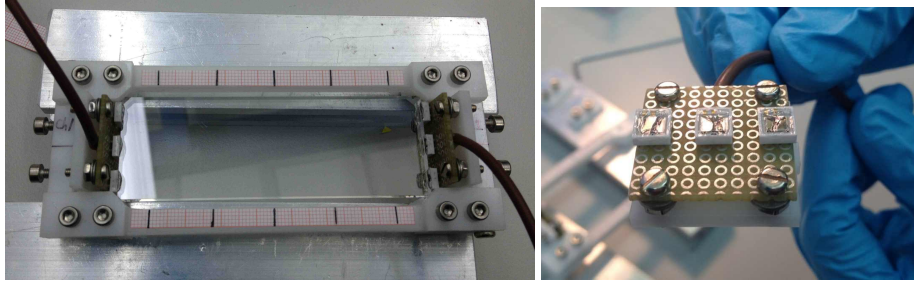


FIG. 42: (Left) pixel counter prototype with a plastic scintillator (BC422,  $30 \times 90 \times 5 \text{ mm}^3$ ) and six MPPCs (Hamamatsu S10362-33-050C). (Right) three SiPMs mounted on PCB. Optical grease is put on the sensor surface.

cable as long as 7 m directly to the readout electronics without any amplification. The measurements with the prototype counters are performed with a RG178-type coaxial cable of 7.4 m long between the SiPMs and the amplifier to simulate the realistic condition in the final detector.

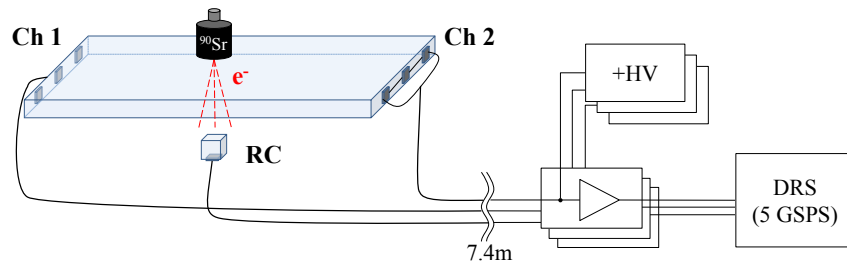


FIG. 43: Typical setup of the measurement with the pixel counter prototype where RC denotes the reference counter.

The waveforms as shown in Fig.44 are analyzed offline to estimate the electron impact time. The waveform time is extracted by the constant-fraction method. The electron impact time is then calculated by taking the difference between the average of the waveform times measured at both sides ( $t_0$  and  $t_1$ ) and the time measured at the reference counter ( $t_{\text{ref}}$ ), namely  $(t_0 + t_1)/2 - t_{\text{ref}}$ , without any correction.

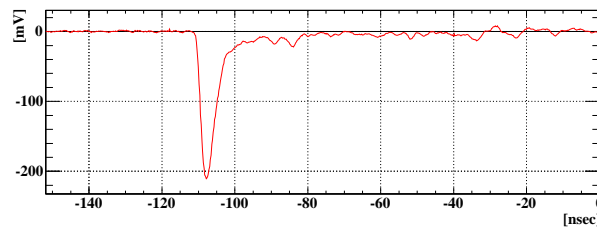


FIG. 44: Typical waveform from the prototype counter (BC422 of  $30 \times 90 \times 5 \text{ mm}^3$ , six MPPCs).

We are trying to find an optimal configuration of the single pixel counter by testing the prototype counters

with different conditions such as scintillator types and geometries, reflector types and number of SiPMs. Hamamatsu MPPC S10362-33-050C is used for the following measurements although we plan to compare the performance of SiPMs from different manufacturers.

Fig. 45 shows the time resolution in  $\sigma$  as a function of the over-voltage per single SiPM. The resolution improves as the over-voltage increases up to about 2.3 V, and then deteriorates at a higher over voltage due to the increased dark noise. The following measurements are performed around the optimum over-voltage.

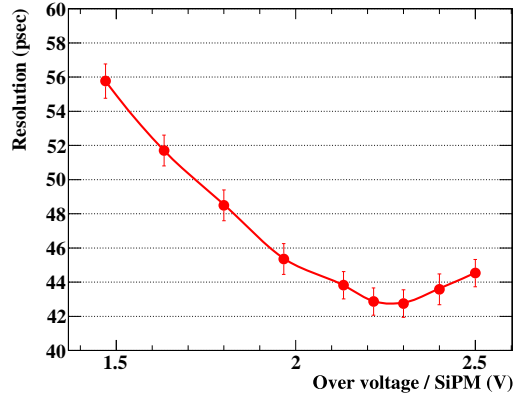


FIG. 45: Typical over-voltage dependence of the timing resolution ( $\sigma$ ) of a prototype counter (scintillator: BC422,  $30 \times 60 \times 4.5 \text{ mm}^3$ , SiPM: 3 MPPCs on each side, reflector: 3M radiant mirror film), where the contribution from the timing resolution of the reference counter (28 ps in  $\sigma$ ) is already subtracted.

Different types of reflectors such as no reflector, Teflon tape, aluminized Mylar and 3M radiant mirror film are tested with a scintillator plate (BC422,  $30 \times 60 \times 4.5 \text{ mm}^3$ ). The timing resolutions are measured at different positions on the scintillator plate. The measured resolution maps are shown in Fig. 46. The best timing resolution of 42.3 ps is obtained with 3M radiant mirror film although a little larger position dependence is observed. This non-uniformity is due probably to the unstable wrapping of the reflector. A stabler wrapping method is now under study.

The geometry of the scintillator has to be optimized by the balance between the cost and the detector performance such as the overall timing resolution and efficiency. The single pixel timing resolutions are measured with different sizes of scintillator plates (BC422). Fig. 47 shows the timing resolutions measured for scintillators of three different lengths with six SiPMs and no reflector. The deterioration of the timing resolution for longer pixel is not so dramatic at least up to 120 mm.

We also tested a wider scintillator plate with a width of 40 mm instead of 30 mm. The average timing resolution is measured to be 54.1 ps in  $\sigma$  for a BC422 scintillator plate of  $40 \times 60 \times 5 \text{ mm}^3$  with six SiPMs and no reflector, while the resolution of 44.6 ps is obtained with the 30 mm-wide pixel at the same condition.

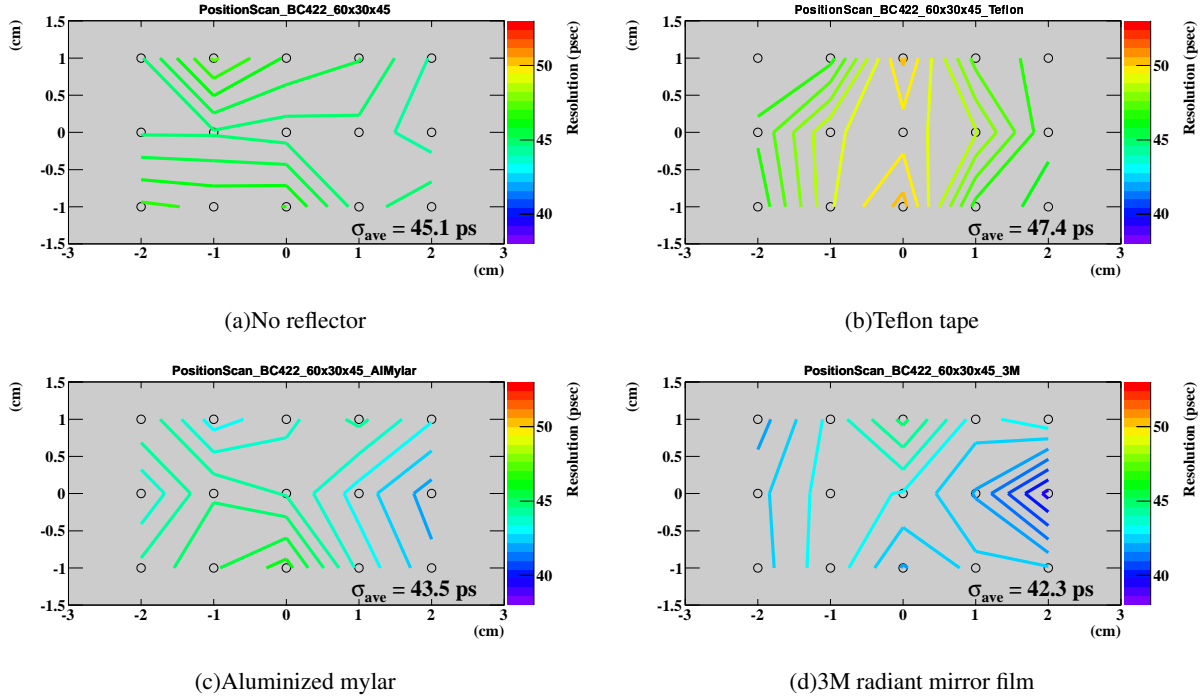


FIG. 46: Single pixel timing resolutions measured with BC422 of  $30 \times 60 \times 4.5$  mm<sup>3</sup> and six SiPMs wrapped with different types of reflectors. The resolution is measured at fifteen positions on the scintillator plate as shown as circles in the figure. The average timing resolution in  $\sigma$  is also shown in each figure.

The difference in the resolutions can be mostly explained by the difference in the sensor coverage at the cross-sectional area of the scintillator plate.

We also measured the performance of the counter with four SiPMs at each side instead of three. A scintillator plate of BC422  $30 \times 60 \times 5$  mm<sup>3</sup> without reflector is used for the measurement. The timing resolution is found to be improved from 44.6 ps to 43.3 ps. The improvement is slightly worse than expected from the increased sensor coverage.

Another type of scintillator, BC418, which has higher light yield and longer attenuation length but a slower rise time as described in Sec. VIB 4, is also tested. The timing resolution for BC418 of  $30 \times 90 \times 5$  mm<sup>3</sup> with six SiPMs and no reflector is measured to be 55.9 ps, which is worse than the timing resolution of 47.0 ps obtained for BC422 at the same condition.

The study on the single pixel configuration is still in progress and the above-mentioned results are quite preliminary. Nevertheless, we already achieved a reasonably good timing resolution for the single pixel counter even with a relatively long scintillator plate.

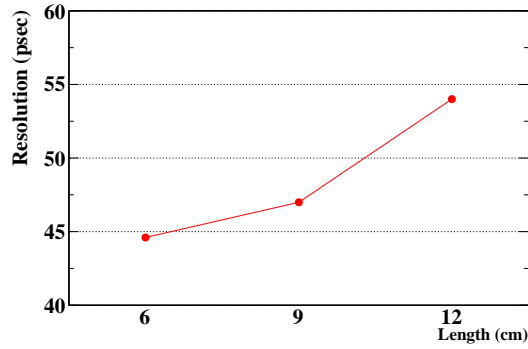


FIG. 47: Single pixel timing resolutions in  $\sigma$  measured with scintillator plates (BC422) of three different lengths.

### 8. Expected Performance

The positron impact time can be precisely measured by averaging the positron hit time over the multiple hit pixels after correcting for the positron travel time between the pixels as illustrated in Fig. 48. The positron path length between the hit pixels is estimated using the positron track extrapolated from the track reconstructed by the positron tracker. Since the positron is tracked by the new tracker up to the entrance of the timing counter, the uncertainty in the extrapolation of the track to the timing counter should be small. The accuracy of the estimation of the path length between the pixels is degraded by multiple scattering in the hit pixels.

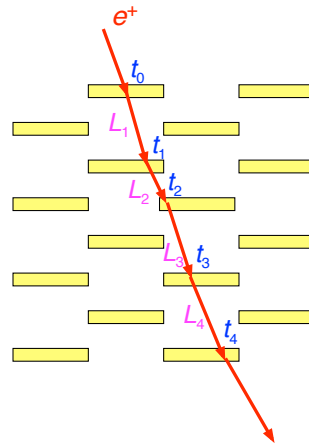


FIG. 48: Positron passing through more than one pixels. The positron impact time ( $t_0$ ) can be measured by averaging the hit time over the hit pixels after correcting for the traveling time between the hit pixels.

The overall timing resolution for a given number of hit pixels ( $N_{\text{hit}}$ ) can be expressed as,

$$\sigma_{\text{overall}}^2 = \frac{\sigma_{\text{single}}^2}{N_{\text{hit}}} + \frac{\sigma_{\text{inter-pixel}}^2}{N_{\text{hit}}} + \sigma_{\text{MS}}^2(N_{\text{hit}}). \quad (8)$$

$\sigma_{\text{single}}$  is the timing resolution of the single pixel.  $\sigma_{\text{inter-pixel}}$  is the contribution from mis-alignment in time or time-jitter between pixels, which is estimated to be 30–40 ps for the planned electronics and is expected to be improved in the new system as discussed in Sec. VIII. The first two terms are reduced as  $N_{\text{hit}}$  increases.  $\sigma_{\text{MS}}$  is the contribution from the multiple scattering, which depends on  $N_{\text{hit}}$ . The positron track deviates from the extrapolation from the track reconstructed by the positron tracker due to multiple scattering on the hit pixel. The angular spread due to multiple scattering on each hit pixel is estimated to be about 35 mrad for 5 mm-thick pixel, which corresponds to  $\sim 5$ ps uncertainty in the correction for the positron flight time between the adjacent hit pixels. Since the uncertainty is added up every pixel hit,  $\sigma_{\text{MS}}$  increases for larger  $N_{\text{hit}}$  and the improvement of the overall time resolution is saturated for larger  $N_{\text{hit}}$ .

The overall performance of the pixelated timing counter is evaluated by means of a MC simulation based on Geant4, where the single pixel timing resolution measured with the prototype counter (see Sec. VI B 7) is taken into account. In the following simulation studies, no positron tracker is placed in front of the timing counter in order to establish its performance. The support structure is not also taken into account, but the effect on the performance is expected to be small. Each pixel module is rotated on  $z$ - $\phi$  and  $r$ - $\phi$  planes with  $10^\circ$  and  $45^\circ$ , respectively, as shown in Fig. 49 such that the angle of the incident signal positron to the scintillator pixel is minimized and thus the acceptance of the pixel is maximized. The overall timing resolution is estimated for different geometries and layouts of the pixel module to find an optimal configuration.

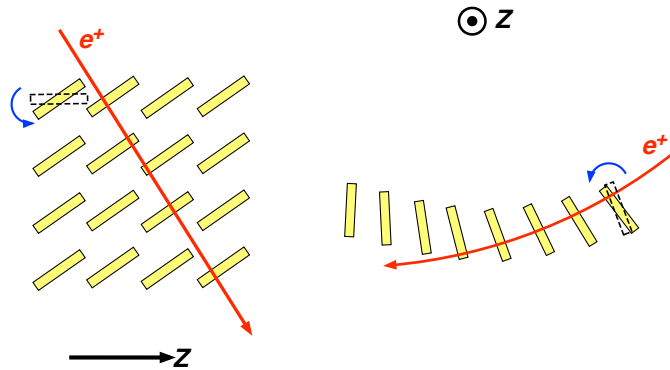


FIG. 49: Rotation of pixel modules on (left)  $z$ - $\phi$  plane and (right)  $r$ - $\phi$  plane.

Fig 50 shows a simulated signal positron with 598 pixel modules with BC422 of  $30 \times 90 \times 5$  mm<sup>3</sup> each and the pixel spacing of 75 mm along  $z$  and 0.13 rad along  $\phi$ . The signal positron hits five pixel modules in

this event.

The left plot in Fig. 51 shows how the estimated overall timing resolution improves as the number of hit pixels increases. The right plot shows the distribution of the number of hit pixels for the signal positrons in this setup. The double-peak structure in the distribution comes from the hit-position dependence of the positron incident angle. The average overall timing resolution is estimated to be 35 ps in  $\sigma$ .

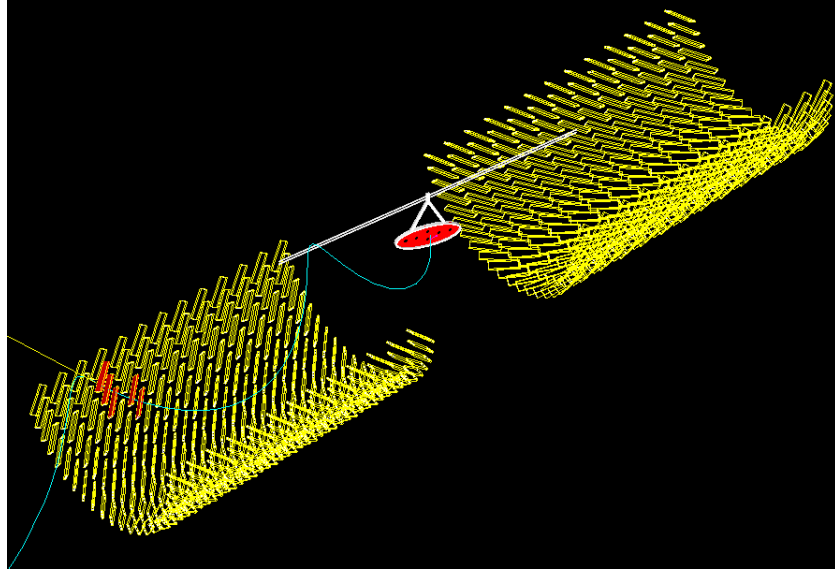


FIG. 50: Simulated signal positron with the pixelated timing counter.

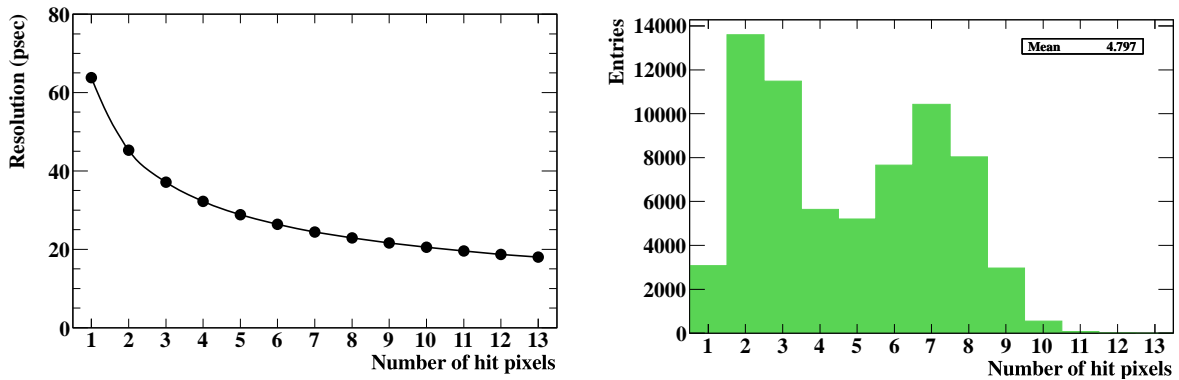


FIG. 51: (Left) Overall timing resolution in  $\sigma$  as a function of the number of hit pixels and (right) distribution of the number of hit pixels for signal positron.

The effect of the geometry and the spacing of the pixel module on the overall detector performance is studied. The left plot of Fig. 52 shows the overall timing resolution and efficiency as a function of the length of the pixel counter with the total number of pixel counters fixed to about 600. The improvement in the

overall timing resolution for longer pixel is because of the increase of the number of hit pixels. The detector performance is compared in terms of a relative sensitivity in the left plot of Fig. 52, where the sensitivity is calculated by Punzi's method [36]. It tends to suggest that longer pixel counter is better from the sensitivity viewpoint. However we may suffer from the pileup and double-hit in a high rate environment if the pixel counter is too long. The effect is now under study.

Another advantage of the longer pixel counter is a possible cost reduction. Fig. 53 shows the total number of pixels necessary to achieve a given fixed sensitivity for the three different lengths of the pixel counter. The total number of pixels can be significantly reduced with longer pixel counter, but again the effect of the pileup and double-hit has to be carefully studied.

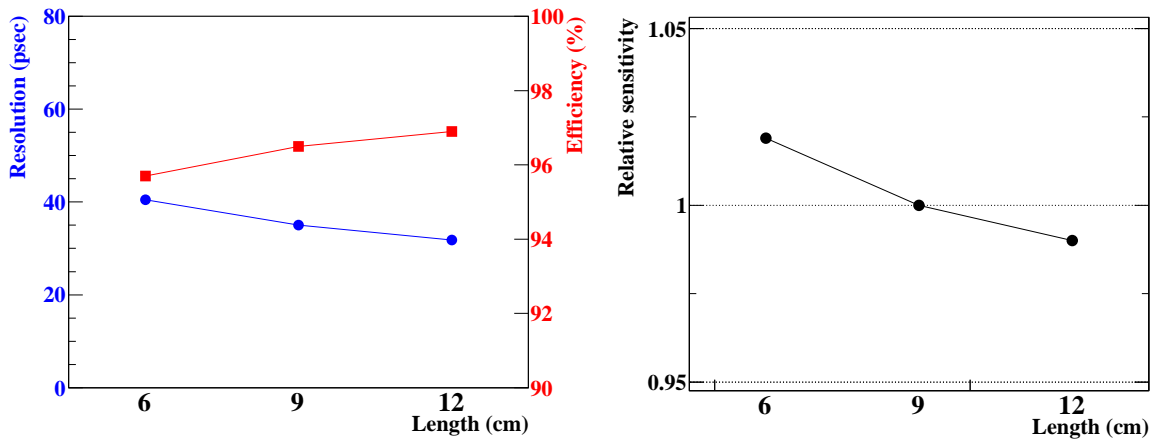


FIG. 52: (Left) Overall timing resolution in sigma and efficiency and (right) relative sensitivity as a function of the length of the pixel counter.

### 9. Calibration

Since SiPM is sensitive to single photoelectron, the gain can be easily calibrated using the single photoelectron peak. Furthermore the output of the pixel module can be equalized by using the Landau peak from the Michel positrons or cosmic ray muon.

It is also quite important to precisely synchronize all the pixel modules although the misalignment in the time of the pixels can be diluted by taking the average over the multiple hit pixels. Two schemes are under consideration for the inter-pixel time-alignment.

- Michel positrons

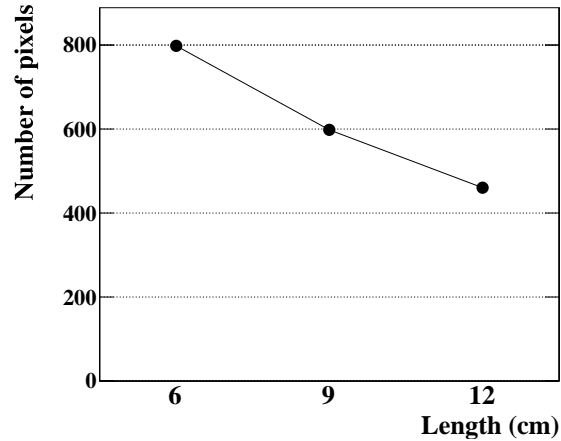


FIG. 53: Total number of pixel counters necessary to achieve a given fixed sensitivity for three different lengths of the pixel counter.

High momentum Michel positrons can also pass through more than one pixel similarly to the signal positrons. The multiple hits should allow the time-alignment between adjacent pixels after correcting for the positron travel time between the hits.

- Laser

The time-alignment can also be done by distributing light pulse from a single laser system to all the pixels through optical fibers of the same length. The candidate for the light source is Hamamatsu picosecond light pulser (PLP10-040), with emission wavelength of 405 nm, pulse width of 70 ps (typ.) and peak power of 100 mW (typ.) [37]. Approximately  $10^7$  photons are emitted from the light pulser in a short pulse. A fast light pulse with about thousand photons can, therefore, be delivered to each pixel module for the time calibration.

### 10. Other Issues

Other issues for the pixelated timing counter are discussed here.

The modest radiation hardness of SiPM is considered as a weak point of SiPM. Increase of the dark current and change of the gain of SiPM are typical effects after certain irradiation. The SiPM in the pixelated timing counter will be irradiated by many Michel positrons during the experiment. The integrated fluence of the Michel positrons during three-years running is estimated to be about  $5 \times 10^9$  positrons/cm<sup>2</sup>. The PSI  $\mu$ SR group performed irradiation tests for a scintillator counter with a similar configuration using Michel positrons as shown in Fig. 54 [38]. The SiPMs of the same type as the one which we plan to use coupled to

a small plastic scintillator are irradiated by Michel positrons of fluence up to  $2.5 \times 10^{11}/\text{cm}^2$  which is more than one order of magnitude higher than our case. They observed a significant increase of the dark current by a factor of six and a 15% gain decrease. Interestingly the timing resolution is unchanged even with the highest fluence. The SiPMs are irradiated also by neutrons and  $\gamma$ -rays in our experiment. The effect is discussed in detail in Sec. VII B 2 for the SiPM planned to be used for the LXe detector and it turns out not to influence the performance of SiPM. The radiation damage of SiPM should, therefore, not be an issue in our case.

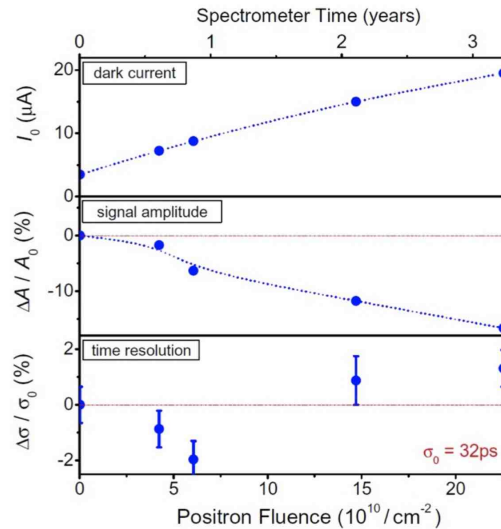


FIG. 54: Results from the irradiation tests of Hamamatsu MPPC (S10362-33-050C) performed by the PSI  $\mu\text{SR}$  group. Significant increase of dark current (top) and 15% gain decrease (middle) are observed, while the timing resolution is unchanged (bottom). Courtesy of Dr. A. Stoykov of Paul Scherrer Institut.

Another issue would be the temperature stability of the SiPM. The temperature coefficient of the breakdown voltage for Hamamatsu MPPC S10931-050P is  $56 \text{ mV}/^\circ\text{C}$ . The MPPC gain at an overvoltage of 1 V is, therefore, changed by 5.6% for a temperature change of  $1^\circ\text{C}$ . The effect of the gain variation on the timing performance should be carefully studied, but in the worst case the gain has to be stabilized either by controlling the SiPM temperature or by adjusting the bias voltage. The temperature coefficient of the gain of the KETEK SiPM is smaller than  $1\%/^\circ\text{C}$  [35]. If the timing resolution with the KETEK SiPM is found to be competitive, it can be a good option to resolve the possible issue of the temperature stability.

We plan to connect outputs in parallel from two or three pixels located apart from each other in order to reduce the number of channels. This operation will considerably reduce the number of electronics channels. The timing performance might be deteriorated by the smearing of the waveform due to the increased output capacitance in the parallel connection. The longer fall time should be irrelevant because of the low pileup

rate, while it would be an issue if the leading edge of the waveform is smeared. We may also suffer more noise on the waveform with the increased capacitance.

### *11. R&D Plan*

A good timing performance of the single pixel module up to 120 mm long is already proved experimentally as described in Sec. VI B 7. Development of dedicated waveform analysis to obtain the best timing resolution is also planned. Further optimization of the single pixel performance is still in progress. Once the geometry of the single pixel module and the readout scheme are optimized, we will build a prototype detector using a small number of pixel modules and perform a beam test in order to demonstrate the improvement of the timing resolution with multiple hits. The schedule of the R&D and the construction will be described in detail in Sec. XI.

## VII. GAMMA DETECTOR

### A. Concept of Upgrade

The liquid xenon (LXe)  $\gamma$ -ray detector is a key ingredient of the experiment to suppressing the background in  $\mu \rightarrow e\gamma$  search. It is, therefore, crucial to substantially improve the detector performance for the upgrade of the experiment. The current detector is the world's largest LXe scintillation detector with 900  $\ell$  LXe surrounded by 846 photomultiplier tubes (PMTs) submerged in the liquid to detect scintillation light in the VUV range ( $\lambda = 175 \pm 5$  nm) (Fig 55). The 2-inch PMT (Hamamatsu R9869) used in the detector is UV-sensitive with a photo-cathode of K-Cs-Sb and a synthetic quartz window. The quantum efficiency (QE) is about 15% for the LXe scintillation photon at LXe temperature of 165 K.

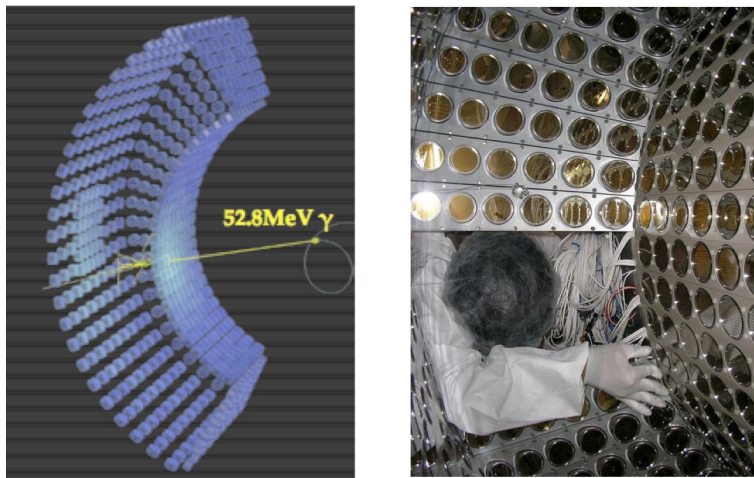


FIG. 55: Current LXe  $\gamma$ -ray detector with 900  $\ell$  LXe surrounded by 846 UV-sensitive PMTs.

The  $\gamma$  entrance face is covered by 216 PMTs with a minimum spacing between adjacent PMTs. The photo-cathode of the PMT is, however, round-shaped with a diameter of 46 mm which is smaller than the interval of the adjacent PMTs of 62 mm. The performance of the current detector is limited due to this non-uniform PMT coverage. Fig 56 shows the efficiency of scintillation light collection as a function of the depth of the first interaction for signal  $\gamma$ -ray of 52.8 MeV. The collection efficiency strongly depends on the incident position. The non-uniform response is partly corrected in the offline analysis, but it still deteriorates the energy and position resolutions due to event-by-event fluctuation of the shower shape, especially for the shallow events.

The main concept of the upgrade of the LXe detector is to reduce this non-uniform response by replacing the PMTs of the  $\gamma$  entrance face with smaller photo-sensors as shown in Fig. 57. Fig. 58 shows a comparison of how the event would look like in two cases with the current PMTs and smaller photo sensors ( $12 \times$

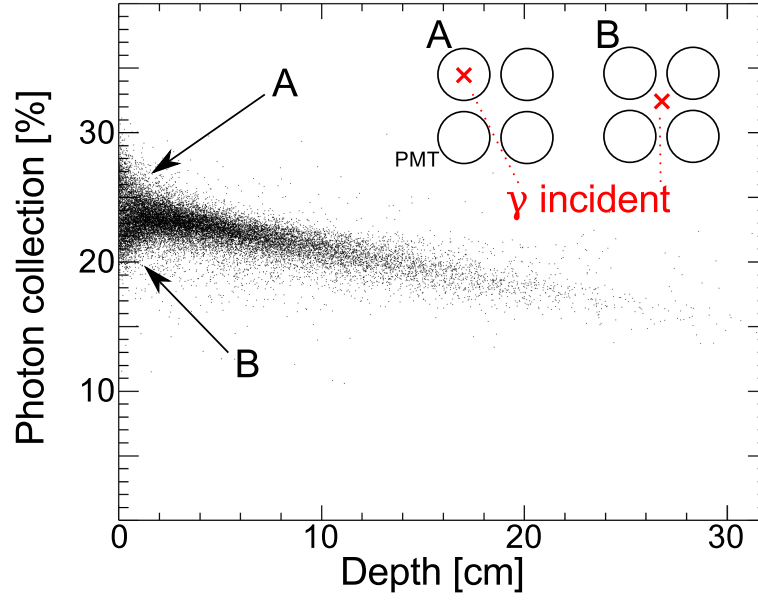


FIG. 56: Efficiency of the scintillation light collection estimated by MC simulation as a function of the depth of the first interaction for signal  $\gamma$ -ray of 52.8 MeV.

12 mm<sup>2</sup>) on the  $\gamma$  entrance face. The imaging power is greatly improved with smaller photo sensors. For example, two local energy deposits in the same shower are clearly separated in the event shown in Fig. 58. It turns out that both the energy and position resolutions greatly improves especially for the shallow events as shown in Sec. VII D.

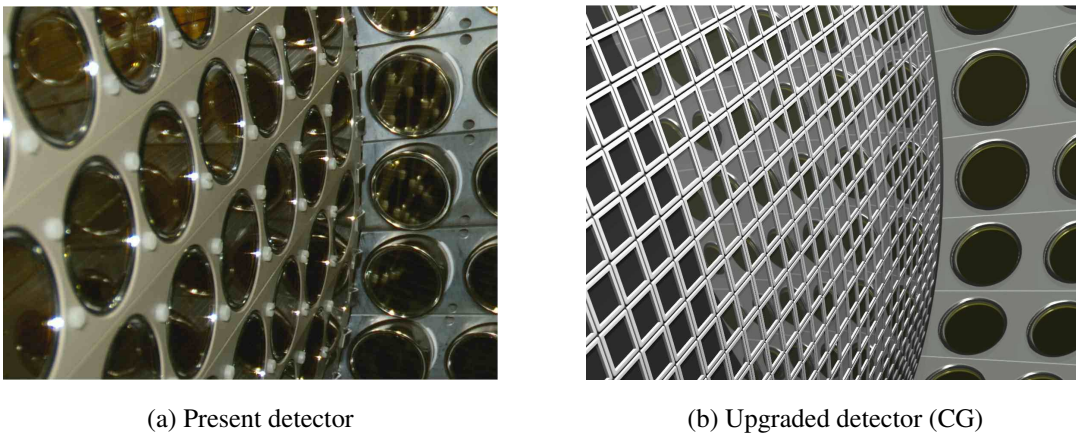


FIG. 57: Possible replacement of 216 PMTs in the  $\gamma$ -entrance face with smaller photo-sensors (about 4000 MPPCs with  $12 \times 12$  mm<sup>2</sup> area each).

The possible candidates of the smaller photo-sensor as a replacement of the current PMT are

- SiPM

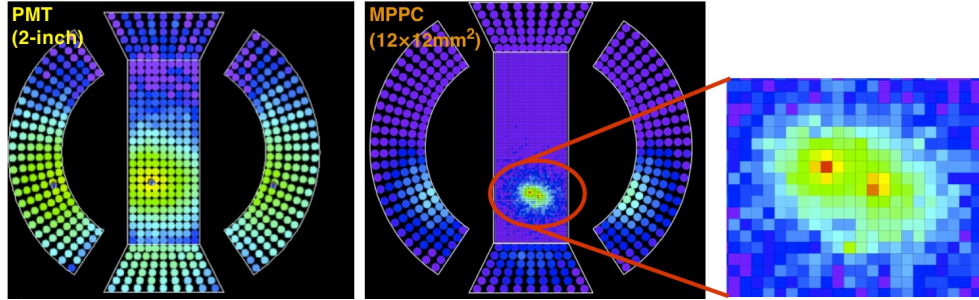


FIG. 58: Typical examples of scintillator light distribution seen by photo-sensors in case of (left) PMTs and (right) smaller photo sensors ( $12 \times 12 \text{ mm}^2$ ) on the  $\gamma$  entrance face.

- 1-inch square-shape PMT
- 2-inch flat panel multi-anode PMT,

where the leading candidate is SiPM as discussed in the following sections, while the development of the PMT is described in the Appendix section (Sec. XIII F). The signal  $\gamma$ -ray traverses the photo-sensors on the entrance face. The material in front of the active LXe volume can be substantially reduced in case of using SiPM which is much thinner than PMT. The  $\gamma$  detection efficiency is estimated to be improved by 9% as discussed in Sec. VII D.

We plan to use PMTs of the same type as the current one for the other faces than the entrance face. It turns out by detailed MC studies developed during the current MEG data analysis that further improvements are possible by modifying the layout of the PMTs on the lateral faces. Fig. 59 illustrates the modified layout viewed on a given  $r$ - $z$  plane.

The  $\gamma$  entrance face is extended along  $z$  to outside of the acceptance by 10% at each side. The extended volume reduces the energy leakage for the event near the lateral wall. The PMTs on the lateral faces are tilted such that all the photo-cathodes lie on the same plane. This operation minimizes the effect due to shower fluctuation for the events near the lateral wall. The energy resolution is thus improved especially for the events near the lateral wall.

## B. Development of VUV-sensitive MPPC

### 1. MPPC Advantage

The MPPC (Multi-Pixel Photon Counter) is a new type of photon counting device produced by Hamamatsu Photonics K.K, which is one of the SiPM families. The MPPC has a lot of excellent features suited

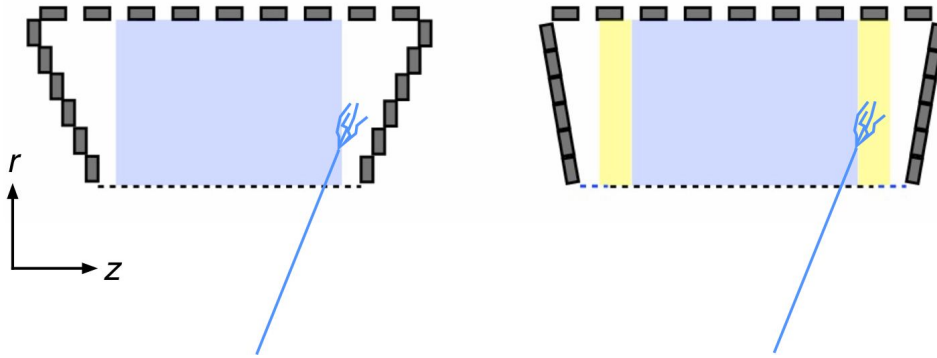


FIG. 59: Current (left) and modified (right) layouts of the PMTs viewed on a given  $r$ - $z$  plane.

for the MEG experiment as discussed in Sec. VI B 5. Moreover, a finer granularity of the scintillation readout with MPPCs allows us to reconstruct shallow events more precisely. Less material budget before LXe active region results in a higher detection efficiency.

## 2. Issues

There are a few issues to be addressed to realize a detection of the LXe scintillation light by MPPC.

The first issue is the photon detection efficiency (PDE) for VUV light. There are two types of the layer structures for the SiPM, p-silicon on a n-substrate (p-on-n) and n-on-p. In general, since the ionization coefficient for electrons is higher than that for holes, the breakdown initiation probability of electrons is always higher than that of holes. Blue light is absorbed close to the SiPM surface, and electrons initiate the avalanche breakdown in the p-on-n case, which results in a higher sensitivity in the blue light region. The MPPC uses the p-on-n structure, which is suitable to detect the blue light. The PDE of the MPPC for VUV light is, however, nearly zero for commercial products since VUV photons can not reach a sensitive layer due to a protection coating layer made of epoxy resin or a silicon rubber and an insensitive contact layer with no electric field. An anti-reflection (AR) coating layer is not optimized to the refractive index of LXe at the scintillation light wavelength (175 nm).

The second issue is the MPPC size. The current largest single MPPC commercially available is  $3 \times 3 \text{ mm}^2$ , which is still too small to cover the inner face of the LXe detector because too many readout channels will be necessary for the small sensor. It is desirable to develop a large area MPPC with  $10 \times 10 \text{ mm}^2$  or larger. However, the larger size of MPPCs could causes a larger dark count rate, larger gain non-uniformity, and larger capacitance (a longer tail in the waveform, a larger noise etc.).

A UV-sensitive MPPC is under development in collaboration with Hamamatsu Photonics to be used for

the upgrade LXe  $\gamma$ -detector. We will describe the performance of the prototype sample in the following sections.

### 3. Setup

We built a test facility at PSI which consists of a 2  $\ell$ -LXe cryostat with a pulse tube cryocooler and a xenon gas purifier to measure basic characteristics of MPPC samples in LXe. There are three stages in the cryostat, each of which can mount a few MPPC samples as shown in Fig. 60.

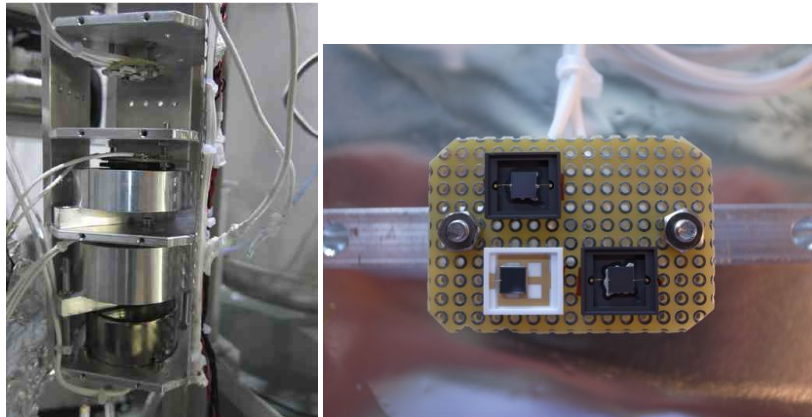


FIG. 60: Test setup for the UV-sensitive MPPC prototype. The left picture shows three stages to mount MPPC samples in the cryostat. The right figure shows three MPPC samples mounted on a stage. The size of the sample in this picture is  $3 \times 3 \text{ mm}^2$ ,

We install  $\alpha$  sources for the absolute PDE measurement, LEDs for calibration and a UV-sensitive PMT for triggering on  $\alpha$  events inside the cryostat. The MPPC mounting stages are surrounded by a wall with a special coating to suppress the reflection of the VUV scintillation light. About one thousand photons from an  $\alpha$  source reach the active area of the MPPC ( $3 \times 3 \text{ mm}^2$ ).

### 4. PDE

Prototypes ( $\sim 40$  samples up to now) optimized for VUV detection are produced by Hamamatsu, which have no protection coating, a thinner contact layer, or optimized AR coating with different parameters.

We succeeded to detect the LXe scintillation photons from  $\alpha$  event by using the prototype sample. Fig. 61 shows signal waveforms from the MPPC sample (upper figure) and a UV-sensitive PMT (lower one) for the same  $\alpha$  event.

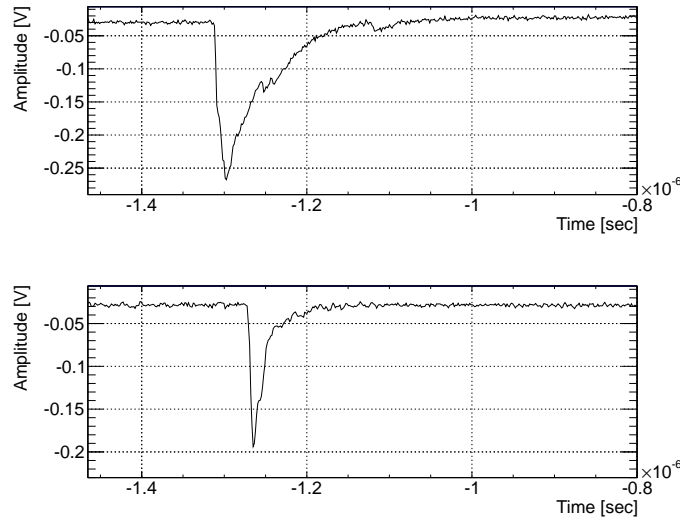


FIG. 61: A MPPC signal waveform (upper) and a PMT signal waveform (lower) for the same  $\alpha$  event taken with a waveform digitizer. A sampling frequency of the digitizer is 700MHz.

The number of detected photoelectrons for  $\alpha$  event is calculated from the ratio of the observed charge to that obtained for a single photoelectron event. The PDE is then estimated from the ratio of the detected number of photoelectrons to the expected number of incoming scintillation photons from  $\alpha$  event. This PDE still contains contributions from cross-talk, after-pulse, and the infrared component of the LXe scintillation light. The contribution from the infrared component is estimated to be  $\sim 1\%$  indirectly by using the signal observed with a commercial MPPC (S10362-33-100C), is supposed to be insensitive to VUV component.

Fig. 62 shows the measured PDEs for four MPPC samples after correcting for the contributions from cross-talk and after-pulse. There is roughly 30% uncertainty in the PDE measurement which comes from the uncertainty in the estimation of the cross-talk + after-pulse probability. The best sample shows a PDE higher than 10% PDE in LXe. It is somewhat smaller than the QE for the UV-sensitive PMT of the current detector ( $\sim 16\%$ ). However since the sensor coverage on the inner face is increased by 50% using MPPCs, the total photoelectron statistics would not be changed. Note that the energy resolution of the current detector is not limited by the photoelectron statistics.

The measured gains are also shown in Fig. 62. This can be measured directly by using a single photoelectron charge distribution. All the samples show the gains higher than  $10^6$  at a reasonable overvoltage, which is high enough for our purpose.

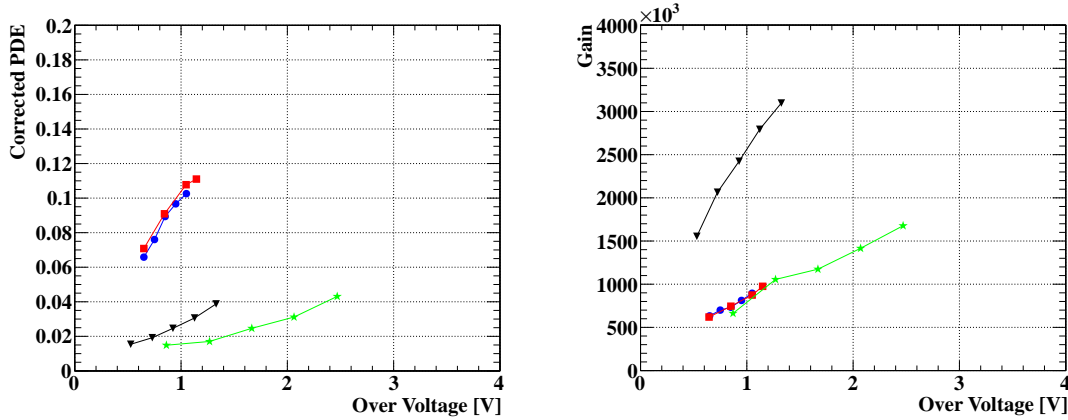


FIG. 62: (Left) Measured PDEs and (right) gains as a function of the over-voltage. In the right plot, the sample with black triangles shows a higher gain and larger slope. It is due to the different pixel pitch ( $100\ \mu\text{m}$  for the black triangle and  $50\ \mu\text{m}$  for the others).

### 5. Transit Time Spread

The transit time spread (TTS) of commercially available MPPC is about 100 psec. It is better than that of PMT, which is typically about 750 psec. The single photoelectron time resolution of MPPC is, therefore, better than that of PMT. However TTS of VUV MPPC has never been measured. The attenuation length VUV light in silicon is very short ( $\sim 5\ \text{nm}$ ); VUV photons therefore generate electron-hole pairs near the surface of silicon. The statistical fluctuation of the travel time of electrons reaching the multiplication layer would be a source of the time-jitter.

The time resolution is evaluated by measuring the time difference of two MPPCs looking at the same  $\alpha$ -event. Since the number of photoelectrons observed in the test-setup is about 100, the width of the time-difference is limited by the photoelectron statistics. In order to estimate TTS, the contribution of the photoelectron statistics is deconvolved from the time-difference distribution. As a result, TTS is estimated to be about 150 psec. The contribution of TTS to the time resolution of the MEG LXe detector is, therefore, negligible because the total number of photoelectrons for the signal  $\gamma$ -ray is the order of  $10^5$ .

### 6. Temperature Dependence

Thermally generated free carriers in a depleted layer produce dark counts. The typical dark count rate is 100 kHz-10 MHz per  $\text{mm}^2$  at room temperature. It is known that the dark count rate is suppressed by five orders of magnitude at LXe temperature (165 K) [39]. Our test measurements confirm that the dark count

rate is reduced down to 1 Hz -100 Hz for  $3 \times 3 \text{ mm}^2$  samples at LXe temperature as shown in the left figure in Fig.63.

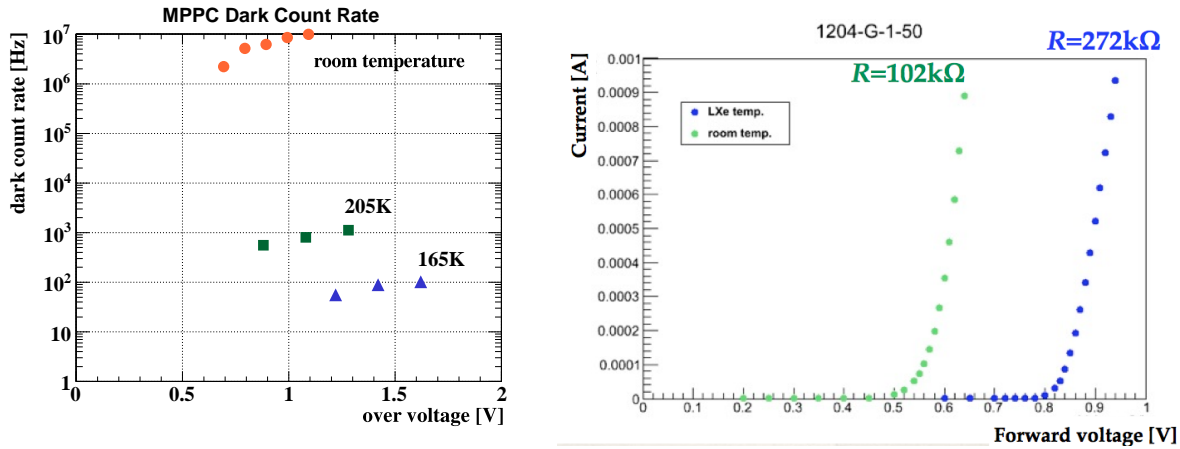


FIG. 63: (Left) The dark count rate measured at different temperatures (room temperature, 205 K and 165 K). (Right) Resistance of poly-silicon quench resistor measured at LXe and at room temperatures by applying forward voltages.

Polysilicon resistors are commonly used for quenching the breakdown in MPPC. The resistivity of the polysilicon changes with temperature. The right figure in Fig. 63 shows the measurement of the quench resistance at LXe and at room temperatures. The resistance at LXe temperature is measured to be more than a factor of two higher than that at room temperature. There is a linear correlation between the resistance of the quench resistor and the falling time of MPPC signal; a higher resistance leads to a longer waveform tail. The quenching resistance has to be reduced for the use at LXe temperature.

The breakdown voltage of MPPC is known to have a relatively large temperature coefficient and the gain and PDE of MPPC can, therefore, be easily shifted depending of the temperature. It could be an issue of the stability of the detector performance. The temperature coefficient of the gain is measured for the UV-sensitive MPPC. Fig.64 shows the temperature dependence of the amplitude of the single photoelectron signal. The LXe temperature is controlled by changing the pressure in this measurement. The measurement is performed at the pressures of 0.115, 0.135, 0.15, and 0.19 MPa which correspond to temperatures of 165,169,171 and 176K, respectively. At each temperature condition, the gain measurement is done for different bias voltages. We measure the temperature coefficient of the gain to be  $-2 \text{ \%}/\text{K}$  independently of the bias voltage. On the other hand, the LXe temperature stability of the current detector is measured to be smaller than 0.15K (RMS), which is most likely to be dominated by the precision of the temperature measuring device. The fluctuation of the MPPC gain in the final detector is, therefore, expected be smaller than 0.3% (RMS). The temperature dependence of the PDE is not yet measured, but is likely to have the

same temperature coefficient as the gain. This means that the fluctuation of the overall gain of the MPPC in the final detector should be smaller than 0.6%, which is smaller than the expected energy resolution of the final detector as described in Sec. VII D.

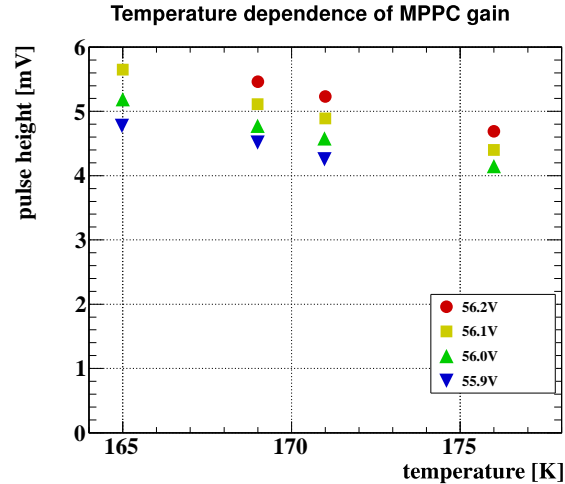


FIG. 64: Temperature dependence of MPPC gain.

### 7. Radiation Hardness

Radiation produces defects in the silicon bulk or at the Si/SiO<sub>2</sub> interface of SiPM. As a result, some parameters of SiPM such as the breakdown voltage, leakage current, dark count rate, gain, and PDE may change after irradiation. There were a lot of previous works to study the radiation hardness of the SiPMs by irradiating the SiPM with  $\gamma$ -rays, neutrons, protons, or electrons.

An increased dark count rate was observed at more than  $10^8$  neutrons/cm<sup>2</sup>, and a loss of single p.e. detection capability was observed at more than  $10^{10}$  neutrons/cm<sup>2</sup> [40]. From the neutron flux measured at the MEG experimental area, the total neutron fluence is estimated to be less than  $1.6 \times 10^8$  neutrons/cm<sup>2</sup> in the MEG upgrade.

Increased leakage current was observed with a  $\gamma$ -ray irradiation of 200 Gy [41], while the  $\gamma$ -ray dose in the MEG upgrade is estimated to be 0.6 Gy.

This means that the radiation damage should not be an issue for the MPPC for the MEG upgrade.

### 8. Linearity

SiPM shows a non-linear response when the number of incident photons is large compared to the number of pixels of the device. The optimal condition is that the number of incident photons be much smaller than the number of pixels without any localization. Fig.65 (left) shows the measured response functions for the SiPMs of  $1 \times 1 \text{ mm}^2$  with the different total numbers of pixels illuminated by 40 ps laser pulses [42]. For the LXe detector in the MEG upgrade, the expected number of photoelectrons reaches up to 12000 p.e. on  $12 \times 12 \text{ mm}^2$  sensor area ( $\sim 20\%$  of the total number of pixels, 57600) for very shallow signal events. The expected non linearity is, therefore, not a big issue and can be corrected by a careful calibration.

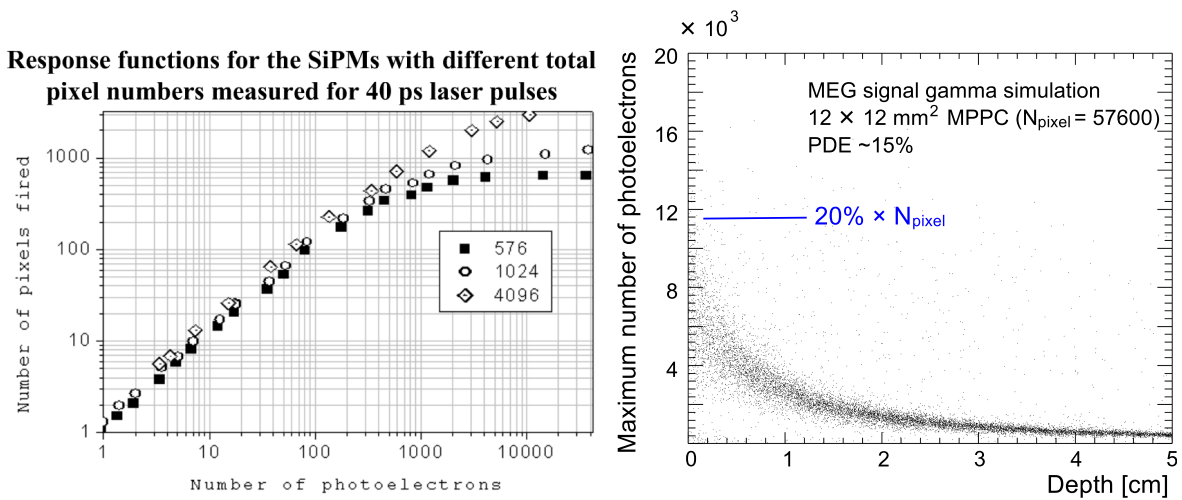


FIG. 65: (Left) Response functions for the SiPMs with different total pixel numbers measured for 40 ps laser pulses [42]. (Right) The number of photoelectrons expected with  $12 \times 12 \text{ mm}^2$  MPPC in the MEG Monte Carlo simulation

### 9. Large Area Samples

The current largest MPPC ( $3 \times 3 \text{ mm}^2$ ) is still too small for the MEG LXe detector, and we need at least  $\sim 10 \times 10 \text{ mm}^2$  to replace the PMTs. When we construct a larger size of sensors, we have to pay attention to a possible increase of the dark count, gain uniformity over the sensor area, and an increase of the sensor capacitance. We study the possible issues of the large area MPPC by using a commercial monolithic array MPPC (non UV-sensitive), which is composed of  $4 \times 4$  separate sectors with  $3 \times 3 \text{ mm}^2$  active area each (Hamamatsu S11827-3344MG, the left picture in Fig 66). All 16 sectors are connected in parallel so that the module can work as a single large-area MPPC with an active area of  $12 \times 12 \text{ mm}^2$ . Single photoelectron

peak is clearly resolved in the charge distribution observed for the dark noise (the right figure in Fig 66). The dark count rate of the module is measured to be 720 Hz at LXe temperature, which is low enough for the MEG LXe detector. We observe a longer fall-time and a larger noise caused by the increase of the sensor capacitance compared to the  $3 \times 3 \text{ mm}^2$  MPPC.

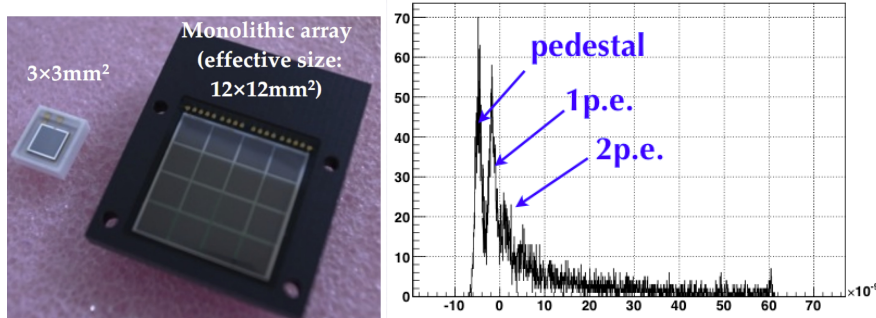


FIG. 66: (Left) Monolithic array MPPC produced by Hamamatsu (S11827-3344MG). (Right) Charge distribution of dark counts measured by the monolithic MPPC. 1 p.e. peak is clearly resolved.

Recently, Hamamatsu has provided us with large area MPPC samples with VUV sensitivity. The MPPC parameters are the same as that for the previous small sample with the best PDE (see Sec. VII B 4), and the size is  $12 \times 12 \text{ mm}^2$ . This sample is being tested in our test setup, and the  $\alpha$  source events are successfully observed. The measurements are still going on, and the careful checks for this sample will be done later. The characteristics of the large-area samples are still being investigated in detail but the preliminary measurement shows that the PDE is consistent with the best small samples.

#### 10. Possible Further Improvements of MPPC Performance

Hamamatsu Photonics has recently developed a new type of MPPC with a significantly improved performance [43]. The new features are the followings.

- Double metal trace structure
- Metal quench resistor
- Optimized layer structure

The double layer structure of the metal trace line connecting pixels enables more uniform and lower resistance without losing the geometrical fill factor. This leads to a significant improvement of the inter-pixel jitter from 300 ps to 150 ps.

TABLE X: Performance improvement for the new type of MPPC [43].

	<b>Standard MPPC</b>	<b>New MPPC</b>
Dark Count	2.7 Mcps	1.7 Mcps
After-pulsing	> 100%	3%
PDE	38%	43%
Overvoltage range	1.5-2.5 V	2-3.5 V
Timing resolution	250 ps	140 ps

A poly-silicon quench resistor is used for the conventional MPPC. The drawbacks of the poly-silicon quench resistor are that it has a large negative temperature coefficient and the per-pixel variation of the resistance is relatively large due to grain boundaries of the resistor structure. We, therefore, suffer from high resistance of the quench resistor especially at low temperature, which causes slow pixel recovery and a long signal tail. A metal quench resistor is used in the new MPPC to overcome these problems. The uniformity of the resistance is found to be improved by more than a factor of two. The temperature coefficient is measured to be smaller by a factor of five.

The probability of the after-pulsing is greatly reduced by an optimized layer structure in the new MPPC. Thanks to the dramatic suppression of the after-pulsing, an operation at a much higher overvoltage is now possible. This will improve the performance of the MPPC such as the gain, PDE, temperature stability and timing resolution.

The performance of the new MPPC is summarized in Table X. All the above-mentioned features can be applied to the MEG MPPC too and thus further improvement of the performance is anticipated.

### *11. MPPC in Other Experiments*

There are examples of particle physics experiments that have already successfully implemented a large number of MPPCs as photo sensors and achieved high detector performance. We can learn various aspects of mass production and quality control of MPPCs from these experiments. The T2K experiment is the first experiment to develop a dedicated MPPC (S10362-13-050C) for their purpose. About 64,000 MPPCs of this type are used in the “near detector complex” (ND280) where a magnetic field of 0.2 T exists and the space for the sensor is limited. They developed a system and technique to characterize a large number of MPPCs and successfully managed a quality control [44].

Another example is the First G-APD Cherenkov Telescope (FACT), which is an imaging atmospheric

Cherenkov telescope using 1440 MPPCs (S10362-33-50-C). They succeeded to improve the sensitivity of their instrument, which is currently using PMTs, thanks to the lower operation voltage, robust performance, and higher photon detection efficiency of MPPCs [45].

### C. Detector Design

#### 1. Design of Sensor Package and Assembly

Fig. 67 shows a possible design of the UV-enhanced MPPC package. The sensor chip with an active area of  $12 \times 12 \text{ mm}^2$  is glued on a ceramic base of  $15 \times 15 \text{ mm}^2$ . The ceramic is chosen as a base material because the difference in the thermal expansion rate compared to silicon is relatively small at LXe temperature.

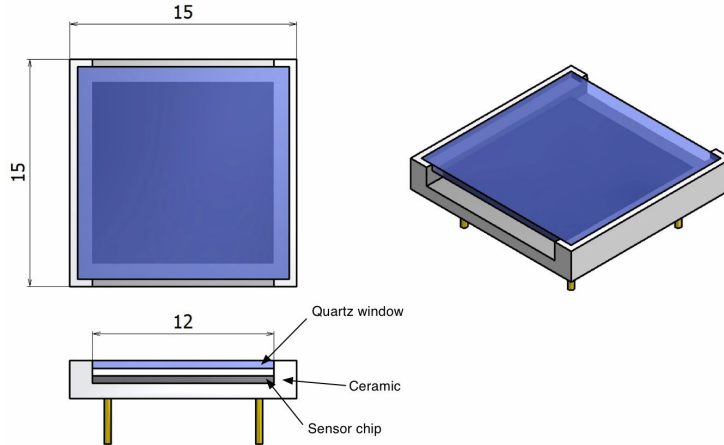


FIG. 67: Possible design of MPPC package.

The sensor active area is covered with a thin quartz window for protection. The window is not hermetic; there is a gap between the sensor and the window where LXe penetrates in during the detector operation. High quality VUV-transparent quartz such as Asahi Glass AQ2 and Shinetsu SUP-P700 is used for the window. Fig. 68 shows the transmission efficiency as a function of wavelength for Asahi Glass AQ2, where we can see that the transmission is quite high for the LXe scintillation light of 175 nm. It should be noted that the reflection loss is smaller than shown in the figure since both sides of the quartz window touch LXe which has the refractive index close to that of the quartz window (LXe: 1.64, quartz: 1.60).

The MPPCs are mounted on a PCB strip as shown in Fig. 69. Each PCB strip has 44 MPPCs in a line along  $z$ -direction and 93 strips are arrayed along  $\phi$ -direction on the inner wall of the detector cryostat (Fig. 70). The total number of MPPCs is 4092. The MPPC package has four electrode pins (two pins

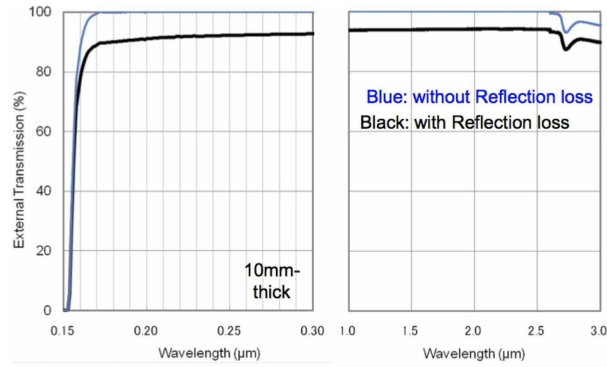


FIG. 68: Transmission efficiency as a function of wavelength for high quality VUV-transparent quartz (Asahi-Glass AQ2).

connected to the sensor chip and two dummy pins just for stable alignment) and is plugged in socket pins on the PCB. This mounting scheme allows easy replacement of the MPPC module in case it is necessary.

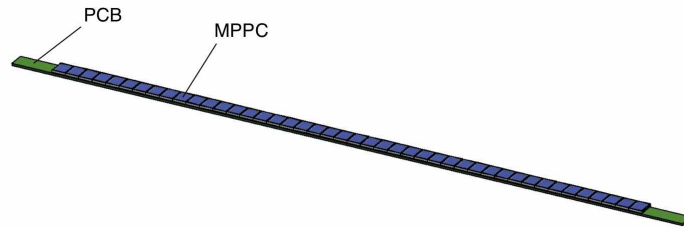


FIG. 69: MPPCs mounted on PCB strip.

The signals from the MPPCs are transmitted on signal lines of the PCB which are designed to be well shielded from both outside and adjacent channels and to have  $50\ \Omega$  impedance. Similar PCBs are used in the feedthrough of the cryostat as described in Sec. VII C 2.

It is important to precisely align the PCB strips on the inner wall of the detector cryostat and to minimize the gap between the strip and the wall since LXe in this gap deteriorates the  $\gamma$ -ray detection efficiency and causes an undesirable low energy tail in the energy response function of the detector. We can have mechanical structures on the cryostat to fix the strips, but only at both ends of the strip, outside the acceptance. Even small distortions of this thin and long PCB strip could, therefore, be an issue. Fig. 71 illustrates a possible scheme to firmly fix the PCB strips on the cryostat wall, where the PCB strips are pressed to the wall by using several thin metal wires stretched along  $\phi$ -direction.



FIG. 70: Assembly of 93 PCB strips on the inner wall of the  $\gamma$  entrance window.

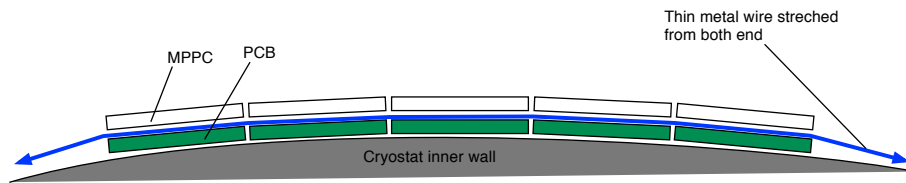


FIG. 71: Possible scheme of alignment of the MPPC PCB strips (cross-sectional view on  $x$ - $y$  plane at a given  $z$ ). The PCB strips are pressed to the cryostat inner wall by thin metal wires stretched along  $\phi$ -direction.

## 2. Signal Transmission

It is not an easy task to transmit about 4000 MPPC signals to DAQ electronics without introducing noise or distortion. We have to pay attention to pickup noise, cross-talk, and limited space in the cryostat and the feed-through etc. In order to overcome such issues, we are developing a multi-layer PCB with coaxial-like signal line structure. It is planned to be used for both the PCB for MPPC mounting and the vacuum feed-through of the cryostat.

As described in Sec. VII C 1, 44 MPPCs are mounted on a PCB strip and 22 signal lines embedded in the strip transmit signals to each end. Fig. 72 shows the possible layer structure of the PCB. There are two signal layers, each of which contains 11 signal lines in 15 mm width. Each signal line is surrounded by ground patterns to minimize cross-talk effect and to be well shielded from outside. In total, six layers (two layers for signal, and four layers for ground) are used. The dimensions of the layers are adjusted to have

50  $\Omega$  impedance.

A prototype of the PCB for MPPC mounting is developed as shown in Fig. 73. The length of 15 cm is much shorter than that of the final PCB strip such that it can be tested in the small LXe test facility. However, the signal line in the PCB has the same coaxial-like layer structure as the final one. The total length of the signal line is about 35 cm, which is also the same as that of the final one. Similarly to the final PCB, MPPCs are plugged in socket pins on the PCB and MMCX (micro-miniature coaxial) connectors are used at the end of the signal line. The prototype PCB is being tested in the LXe test facility using real MPPC signals. The test results will be described in Sec.VII C 3.

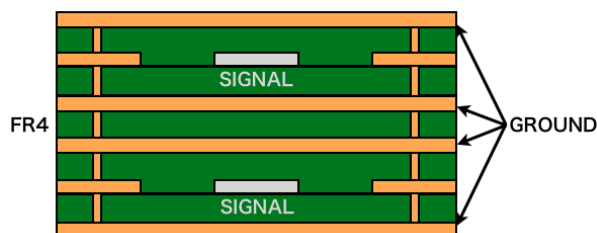


FIG. 72: A cross-sectional view of the possible PCB design in which a signal line is shielded by surrounding ground lines and ground layers. The total thickness of the PCB board is 1.6 mm.

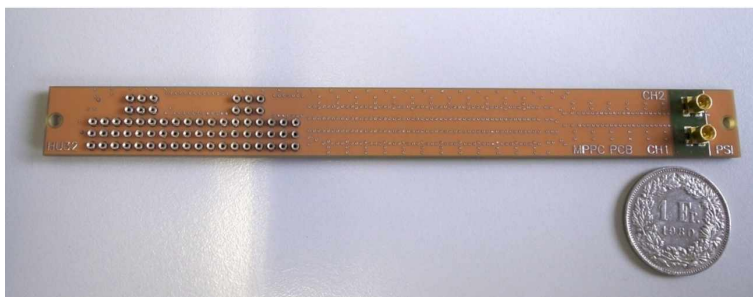


FIG. 73: Prototype of the PCB for MPPC mounting.

The signal lines on the PCB strip are connected to (real) thin coaxial cables either by means of connectors or by soldering them at the edge of PCBs. Then the signals are transmitted to the feed-throughs using thin coaxial cables with a length of at least 3 m. One of the possible candidates for the coaxial cables is Radiall MIL-C-17/93-RG178[46], which is currently used for the drift chamber in the MEG experiment.

The current LXe detector has in total 10 DN160CF flanges for signal and HV cables of 846 PMTs. Since only the 216 inner PMTs will be replaced with 4092 MPPCs and other 630 PMTs will remain in the detector, more feedthrough ports will be necessary. A PCB-type feedthrough similar to the PCB for MPPC

mounting is considered as a possible candidate, which can realize high density signal transmission through vacuum walls and low noise environment. A prototype of the feedthrough is made as shown in Fig. 74. We will soon conduct basic tests with the prototype (vacuum tightness, signal transmission quality) both at room temperature and in LXe.

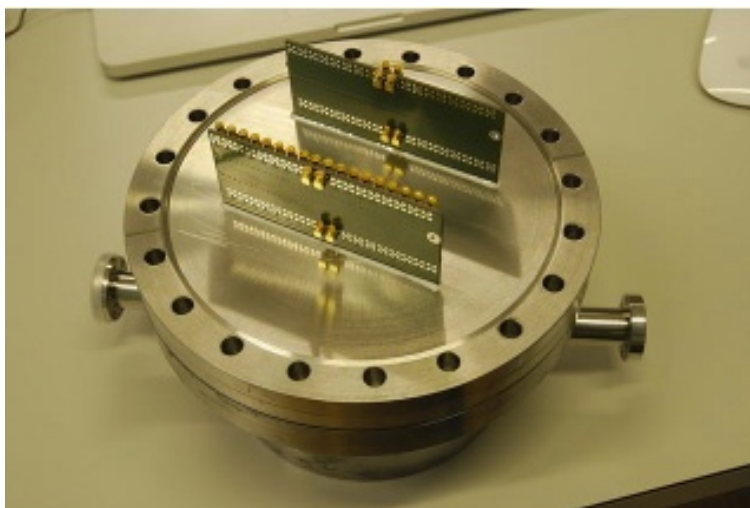


FIG. 74: Prototype of the PCB-type vacuum feedthrough for the MEG LXe detector.

In the final detector, the signal from the feedthrough is transmitted to the electronics using 10 m coaxial cables.

### 3. Test with Cables and Prototype PCBs

A test measurement is performed in order to check the effects of the prototype of the PCB for MPPC mounting, and the Radiall coaxial cable (3 m long) which is a candidate for the MPPC signal cable inside the cryostat as described in Sec.VII C 2). The pulse height, the pulse width and the rise time of the MPPC signal are measured using a commercial MPPC (S10362-33-050C) with the following four different conditions.

1. short cable, without the prototype PCB
2. Radiall cable (3 m), without the prototype PCB
3. short cable, with the prototype PCB
4. Radiall cable (3 m), with the prototype PCB

Fig. 76 shows the measured pulse heights of single photoelectron events at four different conditions.

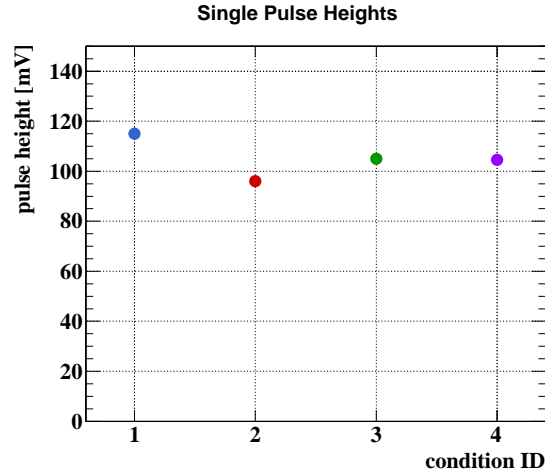


FIG. 75: Pulse heights of single photoelectron events at four different conditions.

No significant deterioration is observed with the prototype PCB nor with the Radiall cable. One notice is that condition 4 was expected to give the worst in these configurations, but it was not the case in this measurement. It indicates that there is some systematic uncertainty in this measurement at the level of 10%.

We plan to send the MPPC signal from the feedthrough to the readout electronics with  $\sim 10$  m-long coaxial cable without any amplification. In order to check the effect of the long cable, we measure the MPPC pulse height, pulse width and the rise time with the Radiall coaxial cables, which is also a candidate for the cable outside the LXe detector cryostat, with different lengths between the feedthrough and the preamplifier.

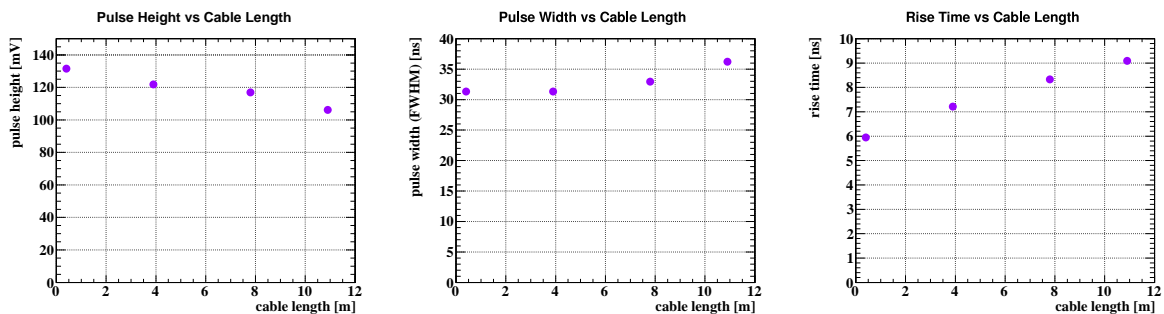


FIG. 76: (Left) Pulse height of single photoelectron events, (middle) the pulse width, and (right) the rise time as a function of the cable length.

The pulse height deterioration is not very large ( $\sim 25\%$ ) with 10 m cable, and we believe this can be recovered using a higher gain at pre-amplifier etc. The transmission of the MPPC signal using 10 m long cable without any amplification seems possible.

#### 4. Readout Electronics

Both the PMTs and MPPCs signals will be readout by DRS4 boards. The size of each readout board is  $10 \times 16 \text{ cm}^2$ , which has 16 input channels with differential DRS driver. Amplifiers are mounted on the board with three switchable gain settings. The difference between adjacent gain stages is about 5 to 10. The different gain stages can then be switched at any time. The higher readout-gain mode is used to detect single photo-electrons for the calibration of MPPCs, while the low readout-gain mode is used to take physics data where a large dynamic range is needed.

No amplifier is installed between the MPPC and the DRS4 board. The bias voltage for MPPC, which is typically 70 V, is supplied from the readout boards through the signal cable.

The signals readout by the DRS boards are used also for the trigger; splitters or additional readout boards are not anymore needed for triggering. All the DRS boards to readout the channels from the LXe detector will be inserted into two 19-inch racks. The place to put the racks would be either near the feedthroughs or at a distance connected with 10 m cables. The use of 10 m cable doesn't seem an issue as discussed in Sec. VII C 3, but the final decision will be made after measuring the noise-level and the signal-attenuation using the prototype detector.

#### 5. Cryogenics

The current cryostat will be re-used for the LXe detector upgrade. In order to cover the increase of the external heat inflow due to  $\sim 4000$  signal cables for the MPPCs, the cooling power of the refrigerator has to be increased either by installing more powerful pulse tube cryocooler or by adding another cryocooler of the same type as the current one. We will evaluate the realistic heat-load through the prototype test. R&D for cooling power upgrade of the refrigerator will be continued in parallel.

### D. Expected performance

The expected performance of the upgrade of the LXe detector is evaluated using MC simulation.

#### 1. Simulation

A full MC simulation code based on Geant4 [47] was developed to compare the performance of the present detector design and the upgrade design. In the simulation, scintillation photon propagation is simulated by Geant4. The reflection of scintillation photons on the MPPC surface was simulated using the

complex refractive index of pure silicon crystal. The reflectance is about 60% typically. In the simulation, the index-number of hit pixel and the arrival time of each scintillation photon are recorded. They are used to make distributions of avalanches in each MPPC. The dark-noise, optical-crosstalk, after-pulsing, saturation and recovering are modeled based on a real measurement and incorporated in the simulation. The waveform of MPPC is simulated by convolving the single photo-electron pulse and the time distribution of avalanches. A simulated random electronics noise is added assuming the same noise level as the present readout-electronics.

The event reconstruction analyses are basically the same as those for the present detector, while the parameters such as waveform integration window and corrections for light collection efficiency depending on the conversion position are optimized for the new design. The non-linear response of the MPPC due to the pixel saturation (see Fig. 65) is taken into account, resulting in a non-linear energy response of the detector. However it is found that the effect on the energy reconstruction is negligible because the fraction of the number of photoelectrons observed by each MPPC is small.

## 2. Results

Fig. 77 shows the position resolutions for signal  $\gamma$ -rays as a function of the reconstructed conversion depth ( $w$ ). In the present detector configuration, the position resolution is worse in the shallow part because of the size of PMTs. The resolution is much better in the upgraded detector configuration. The energy resolution is also much better in the shallow part with the upgraded detector configuration than that with the present detector configuration as shown in Fig. 78 due mainly to the more uniform photon-collection efficiency. The low energy tail is smaller in the upgraded detector configuration because of the lower energy leakage. The resolution is also better in the deepest part because of the modification of the angle of the lateral PMTs. The effect of the electronics noise is studied by changing the random noise level in the simulation. It is confirmed that the effect of the noise is small (Fig. 79) if the noise level stays at the same level as the present detector (0.3-0.4 mV). The measured energy resolution of the present detector (1.7% for  $w > 2$  cm) is worse than that in the simulation (1.0% for  $w > 2$  cm). The reason is not fully understood while the source of the difference can be related to the behavior of PMTs (e.g. gain stability, angular dependence and so on) or optical properties of liquid xenon (e.g. effect of convection). If the former is the case, the difference can become smaller in the upgraded configuration. On the other hand, if the latter is the case, the difference could remain. Figure 80 shows the energy responses with different assumptions; 1: when the additional fluctuation completely vanish in the upgraded detector, 2: when a part of fluctuation remain which corresponds to 1.2% resolution in the present detector configuration. The resolution of 1.2% was

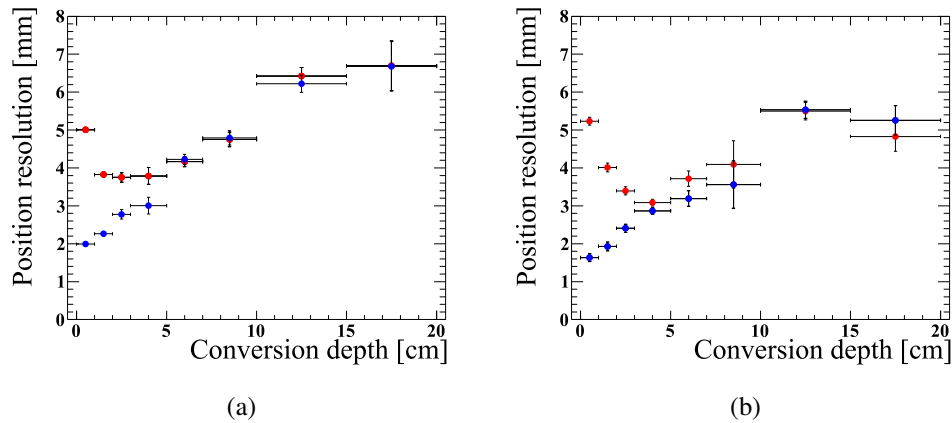


FIG. 77: Position resolutions in the horizontal (a) and vertical (b) directions as a function of the first conversion depth. The resolutions in the present detector configuration are shown in red markers, and those in the upgraded detector configuration are shown in blue markers.

achieved with the MEG LXe large prototype detector., 3: when the fluctuation remain which makes the resolution of the present detector to be 1.7%.

The time resolution of the calorimeter can be limited by six components; the transit time spread (TTS) of photo-sensors, the statistical fluctuation of scintillation photons, the timing jitter of the readout-electronics, the electronics noise, the resolution of the photon conversion point and the finite size and fluctuation of the energy deposits in the LXe. The most of them are common for both in the present and upgraded detectors, however the effect from TTS and electronics noise are different because of the different photo-sensors. The effect of TTS is negligible because it scales as a function of the number of photoelectron, and the light output of liquid xenon is large. The effect of the electronics is larger in the upgraded detector than in the present detector because the leading time of a MPPC pulse for liquid xenon scintillation signal is slower than that of a PMT pulse. In order to estimate the effect, the time resolution of the upgraded detector for signal  $\gamma$  rays is measured in the simulation. The evaluated time resolution with a preliminary waveform and reconstruction algorithms is 84 psec, where the gain of  $2 \times 10^7$  (including the preamplifier gain) and 0.3 mV noise RMS are assumed. In the preliminary analysis, sum-waveforms of 16 adjacent MPPCs are used. The analysis will be improved to use waveform of single MPPC near the  $\gamma$  interaction point. The time resolution could be improved because the small size of MPPCs compared to PMTs makes the fluctuation of the travel-time of scintillation photons from the  $\gamma$  conversion point to a photo-sensor smaller.

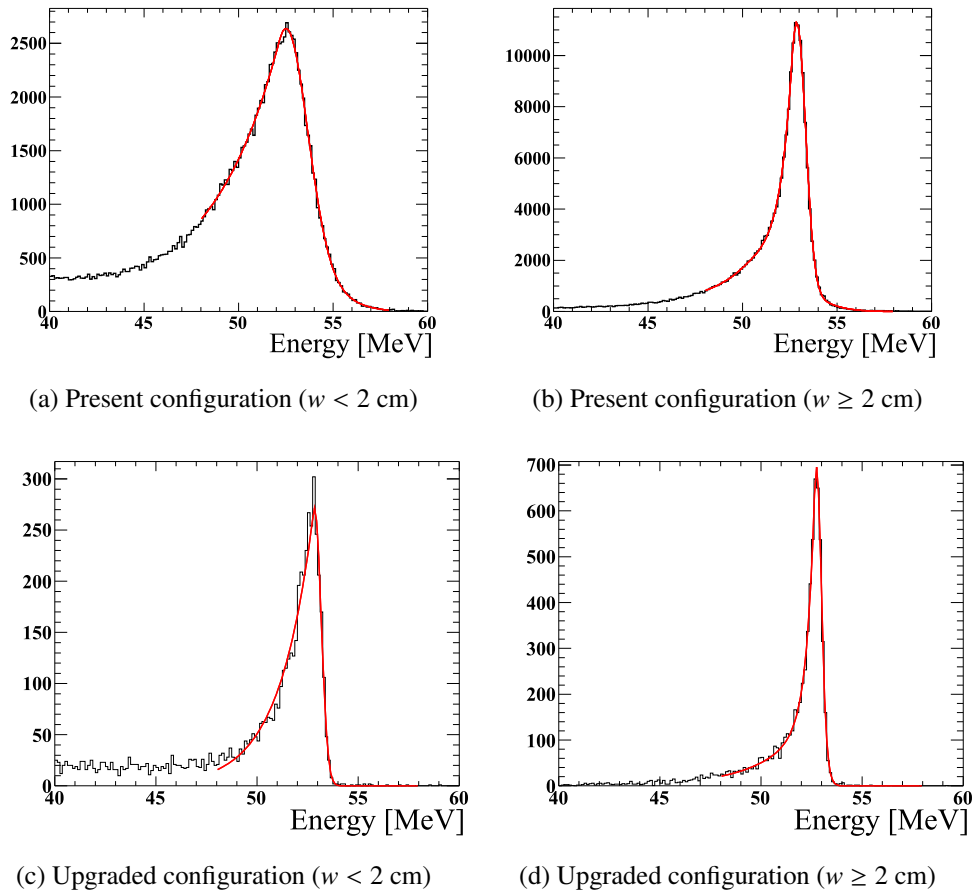


FIG. 78: Energy responses of the LXe detector in the simulation with present (a,b) and the upgraded (c,d) detector configurations. Responses for the shallow (a,c) and deep (b,d) conversion events are shown separately.

### 3. High intensity

The higher background  $\gamma$  rate with the higher muon intensity in the upgraded experiment should not be a problem for photo-sensor operation. On the other hand, the background rate in the analysis energy region would be increased due to pileup. In the analysis for the present detector, the energies of pileup gamma rays are unfolded using the waveform and light distribution on the inner face. In 2011 data acquisition we took data with different beam intensities, 1.0, 3.0, 3.3 and  $8 \times 10^7 \mu/s$ . Figure 81 shows the  $\gamma$ -ray spectrum normalized by the number of events from 48 to 58 MeV; the scaling factors are consistent with the muon stopping rate on the target. The shapes of spectra are almost identical in the analysis region between 48 and 58 MeV after subtracting the energies of pileup  $\gamma$  rays. Since the same analysis can be used also for the upgraded detector, a higher beam rate will not cause additional background rate due to pileup.

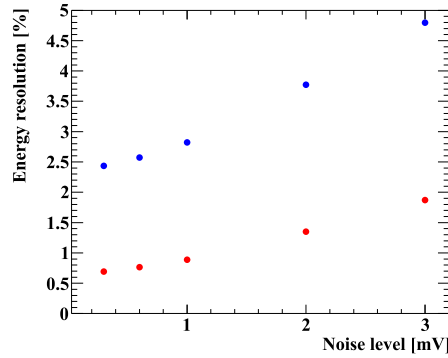


FIG. 79: Energy resolutions as a function of added noise level in the simulation. Effective sigmas of the upper edge (red markers) are obtained by scaling the HWHMs of the upper edge. FWHMs using both edges are shown in blue markers.

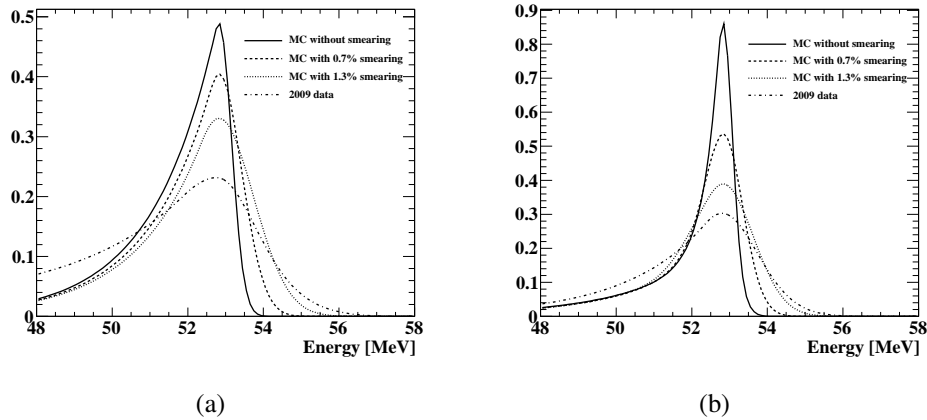


FIG. 80: Energy response functions with various assumptions of additional fluctuation (0, 0.7 and 1.3%) and that of 2009 data.

### E. Prototype Detector

A prototype detector is planned to be built to demonstrate the performance of the LXe detector with MPPC readout on the  $\gamma$  entrance face. The cryostat and some other resources, which were used for the prototype test of the current LXe detector, will be recycled (Fig. 82). A box-shaped LXe with an active volume of approximately  $70 \ell$  is surrounded by 576 UV-MPPCs with  $12 \times 12 \text{mm}^2$  active area each on the  $\gamma$  entrance face and 180 PMTs on the other faces ( $6 \times 6$  PMTs for each face). Since the depth of the active volume is the same as the full-scale detector, this prototype detector is considered as a fraction of the acceptance of the full-scale detector. Either spare PMTs of old version or the PMTs used in the current detector are used in the prototype. For the former case, the construction of the prototype detector can be

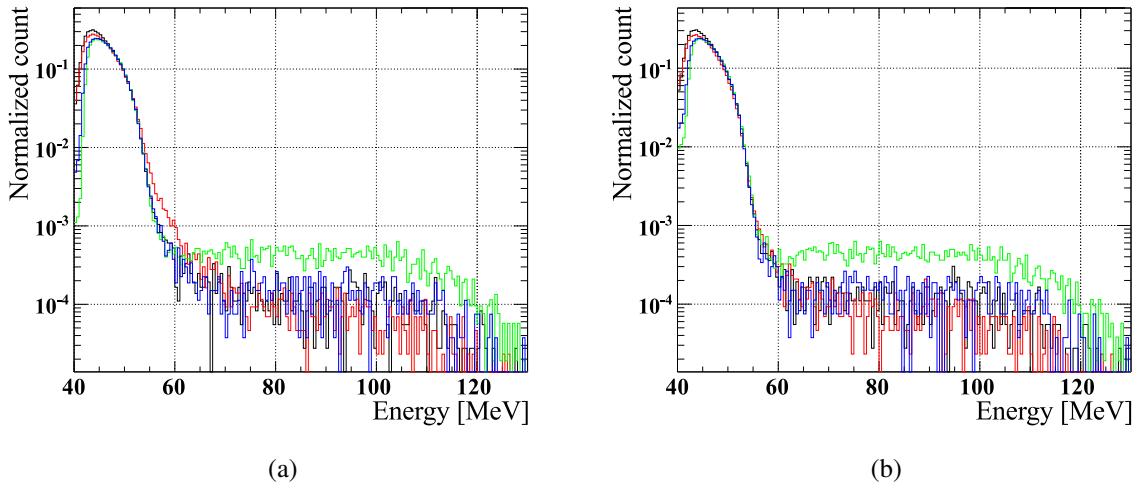


FIG. 81: Reconstructed energy spectrum obtained for different beam intensities. The horizontal axis shows energies without unfolding pileup gamma rays (a), the same after unfolding and subtracting the energy of pileup gamma rays (b), respectively, in GeV. Green, black, blue and red lines show spectrum at muon stopping rate of 1.0, 3.0, 3.3 and  $8 \times 10^7 \mu/s$ , respectively. The spectra are normalized by the number of events from 48 to 58 MeV; the scaling factors are consistent with the muon stopping rate on the target. A difference in the low energy part below 0.045 GeV is due to different effective trigger thresholds; a difference in the high energy part is due to the different ratio between  $\gamma$ -rays backgrounds and the cosmic-ray backgrounds.

started before the current experiment is finished.

We plan to study the performance of the prototype detector with the same techniques as for the current detector, namely using  $\gamma$ -rays with various energies up to 129 MeV from  $(p, \gamma)$ -reaction with a Cockcroft-Walton accelerator,  $\pi^- p$  charge exchange and radiative capture reactions. All components to be developed for the upgrade detector such as the cables, feedthroughs and readout electronics will be tested.

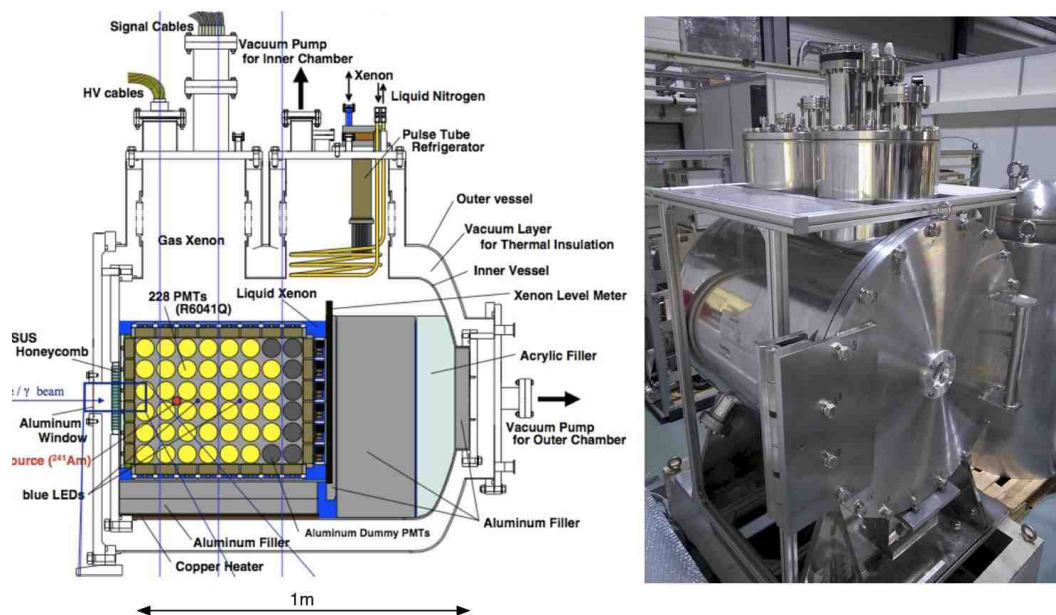


FIG. 82: Prototype of the current LXe detector. The PMTs on the  $\gamma$  entrance face will be replaced with the UV-MPPCs and the depth will be somewhat shortened for the prototype of the upgrade detector.

## VIII. TRIGGER AND DAQ

### A. Requirements

The proposed upgrade of the MEG detector requires two main improvements of the existing DAQ system. On one side more channels are needed both for the DAQ and the trigger systems, and on the other side a higher bandwidth of the waveform digitizing system is required in order to use the algorithms based on cluster timing. While the increase of DAQ channels is moderate and could be fulfilled with the existing system just by using a few more crates, the bandwidth of the old system is limited by the analog front-end of the DRS4 waveform digitizing boards. A cheap and simple scheme has originally been chosen, which uses only a passive transformer to convert the single-ended signal from the drift chambers into the required differential signal needed by the DRS4 chip. This scheme however limits the bandwidth to about 200 MHz.

### B. Proposed DAQ boards—WaveDREAM

We propose a new DAQ board, which combines both the waveform digitizing technology using the DRS4 chip as well as the trigger and splitter functionality of our current system. This way a much more compact system can be constructed, which is necessary given the limited space around our detector.

To overcome the bandwidth limitation, a new active analog front-end has already been designed and tested. This front-end has two switchable gain stages, which can be combined to obtain a post-amplification by a factor one to about 70. The post-amplification can be used to increase the signal amplitude coming from the drift chamber and the SiPM pre-amplifiers which are typical in the order of a few ten millivolts. By increasing the amplitude to a few hundred millivolts, the signal-to-noise ratio inside the DRS4 chip is improved, which allows more accurate charge measurements. Furthermore, the front-end section has been carefully optimized to give an overall bandwidth above 700 MHz. Figure 83 shows the simplified schematic of the new DAQ board.

Several additional features as compared with the current DAQ electronics will be implemented on the new board. Each channel will have a dedicated comparator which can be used to implement a rate counter or a trigger (see subsection below). The board can be operated in a standalone mode, in which a Gigabit Ethernet interface can be used to transfer acquired data directly to a PC. This might be useful for first tests where only a couple of channels will be needed. For the full system, the DAQ boards will be housed in a custom crate especially developed for this purpose. This crate can contain up to 16 boards with a total of 256 channels and a so-called DAQ concentrator board, which collects the data from the 16 DAQ boards, combines them and sends it via Gigabit Ethernet to a PC. The usage of a custom crate as compared with a

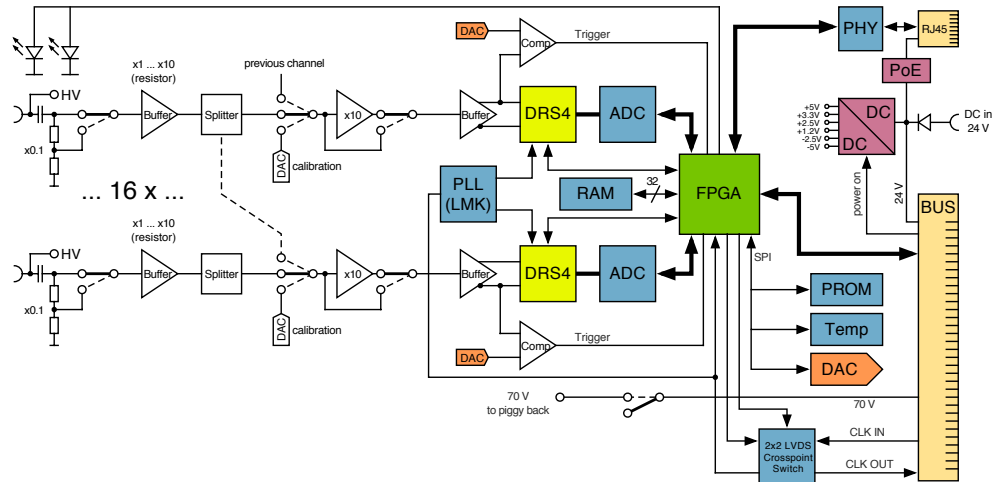


FIG. 83: Simplified schematics of the proposed DAQ board

standard VME system brings a cost saving by a factor of three.

Furthermore, new DRS4 timing calibration methods recently reported on conferences indicate that a significant improvement in the DRS4 timing calibration of up to a factor of three can be achieved. We plan to adapt this new timing calibration to the new boards, which should allow to improve the current timing resolution of 40 ps significantly. This is an important step if the particle detector resolution improves with the upgrade, in which case the electronics contribution would become more significant.

The proposed drift chamber requires the recognition of individual clusters originating from the primary ionization in the chamber gas. In a first phase, this cluster recognition will be done off-line on a PC, which makes it easy to develop and optimize the required waveform analysis algorithms. In a second phase, it is planned to implement the algorithms directly inside the FPGA of the DAQ board. FPGAs with sufficient resources and DSP capabilities have already been selected to support this second phase.

The proposed electronics will be a significant improvement over the current one in terms of channel density and analog bandwidth. It has enough flexibility to adapt itself in terms of selectable gain and FPGA programming to the needs of the new drift chamber system, even if the requirements change during the operation.

### C. Trigger

The functionality of the current MEG trigger system will be integrated into the new DAQ boards. The DRS4 chips operate in the so-called "transparent mode" where their input appears directly at the output. There the connected ADCs can continuously digitize the input to provide data to the trigger. Each ADC digitizes the input signal with 80 MSPS and 12 bits. A potentially poorer determination of the pulse ampli-

tude arising from the slower sampling speed (80 MSPS vs. 100 MSPS), which is relevant for the  $\gamma$ -energy reconstruction, will be eventually compensated by the increased ADC resolution (12 bits vs. 10 bits). A wider dynamic range is in order if we want to fully exploit the improved single photoelectron response of new LXe photosensors<sup>3</sup>. As a result, we don't expect any deterioration of the energy resolution at a trigger level.

Concerning the relative  $e^+ - \gamma$  timing, we will benefit from using the DAQ comparator coupled to each input signal (on both LXe and TC). The estimate due to comparator latch time can be further refined by implementing look-up tables on the FPGA to correct for time-walk effects. Also in this case, the overall resolution is not expected to be spoiled, rather it might be improved up to 1 ns.

Each DAQ board is conceived to operate the same digital algorithm as the current "Type 1" boards: sum of all 16 inputs, maximum pulse amplitude and related index (to provide a coarse determination of  $\gamma$  direction), pulse time. These values are arranged in a 48-bit bus and passed through LVDS serializers to trigger concentrator boards, which are housed at the side of each crate next to the DAQ concentrator boards. These boards are designed to receive and combine all the pieces of information from DAQ boards, thus operating as upper-level trigger boards (a role currently being played by "Type 2" trigger boards, which do not fit in the future design).

#### D. Data reduction

The use of a higher beam intensity as well as the higher number of detector channels than in the current configuration will have the effect of a sizable increase of the data throughput, with severe concerns on both DAQ speed and off-line storage capability. We envisage using two handles to tackle this problem by reducing:

- the event size, by operating a substantial on-line zero suppression;
- the event rate, by exploiting a higher-level trigger based on an on-line track reconstruction.

The first point can be addressed thanks to the sparse occupancy of detector channels. In the case of LXe, for instance, photosensors which are far away from the  $\gamma$ -ray impact point collect very few photons (to be compared to a few thousands being detected by the ones in front of the shower). As their contribution to

---

<sup>3</sup> Let us recall that the C-shape of our LXe detector and the depth of the  $\gamma$ -interaction vertex are such that the bulk of the inner face is shadowed; therefore most of the inner PMTs (namely those which are not just in front of the e.m. shower) use to work in a very few photoelectron regime.

the timing is almost irrelevant, there is no loss of information by recording the sum of groups (4:1 or 9:1) of them.

The basic idea for the reduction of the trigger rate relies on the possibility of using individual signals for each wire end, while in the current trigger configuration we are using overall 32 fanned-in signals (inner and outer wires for each DCs). With so many pieces of information available at DAQ boards, we plan to combine the features of FPGAs and associative memory chips to accomplish both pattern recognition and track filter tasks. This will allow us to strongly suppress the bulk of the events we are currently recording onto the disk, where no condition on track selection is asked for.

Of course any reduction tool should be applied upon condition of no deterioration of signal efficiency and/or resolution.

## IX. FINAL SENSITIVITY

The sensitivity of the upgraded MEG experiment is evaluated by using a maximum likelihood analysis technique developed to extract the upper limit (UL) at 90% C.L. on  $\mathcal{B}(\mu \rightarrow e\gamma)$  in the MEG data analysis [48]. This technique is more efficient and reliable than a simple box analysis, since all types of backgrounds are correctly folded in the global likelihood function and taken into account with their own statistical weights.

An ensemble of simulated experiments (*toy MC*) is created from the probability density functions (PDFs) describing the signal shapes and the background distributions for the photon energy ( $E_\gamma$ ), positron energy ( $E_{e^+}$ ), relative timing and relative angles. The enhanced precision of all upgraded detectors allows a much better separation of the signal from the background and reduces significantly the spill of the gamma and positron background distributions into the signal region, which is mainly due to experimental resolution effects. With a much lower accidental background in the new detector, the muon stopping rate can be higher than the present one: optimization studies are under way, but a muon stopping rate of at least  $7 \times 10^7 \mu/\text{sec}$  is envisaged. The increased muon stopping rate and the enhanced resolutions are taken into account in estimating the number and the distributions of background events expected in the upgraded experiment.

A representative scenario for the detector resolutions and efficiencies is summarized in Tab. XI and compared with the present MEG performance. The efficiency of the positron reconstruction is highly improved with respect to the current one, thanks to the high efficiency of the new tracking system (close to 1) and to the optimized relative position of the tracker and the timing counter.

TABLE XI: Resolution (Gaussian  $\sigma$ ) and efficiencies for MEG upgrade

<b>PDF parameters</b>	Present MEG	Upgrade scenario
$e^+$ energy (keV)	306 (core)	130
$e^+$ $\theta$ (mrad)	9.4	5.3
$e^+$ $\phi$ (mrad)	8.7	3.7
$e^+$ vertex (mm) Z/Y(core)	2.4 / 1.2	1.6 / 0.7
$\gamma$ energy (%) ( $w < 2 \text{ cm}$ )/( $w > 2 \text{ cm}$ )	2.4 / 1.7	1.1 / 1.0
$\gamma$ position (mm) $u/v/w$	5 / 5 / 6	2.6 / 2.2 / 5
$\gamma$ - $e^+$ timing (ps)	122	84
<b>Efficiency (%)</b>		
trigger	$\approx 99$	$\approx 99$
$\gamma$	63	69
$e^+$	40	88

As an example we show in Fig. 84 the  $E_\gamma$  PDF for signal and accidental background events, as simulated in *toy MC*. The expected improvement for the upgrade scenario is visible in comparing these PDF (in blue) with the 2010 MEG data PDF (in black). In the  $E_\gamma$  background PDF various contributions are taken into account: radiative muon decay (RMD), photons from positron annihilation in flight (AIF), or from bremsstrahlung on materials in the detector, pile-up events and resolution effects. The new configuration of the cylindrical drift chamber, with a smaller amount of material close to the electromagnetic calorimeter, reduces the AIF contribution, which is dominant for photon energies  $E_\gamma > 52$  MeV, of about 20% with respect to the present MEG detector. The combined effect of the increased resolution and of the lower high energy background is clearly visible in the right side of Fig. 84.

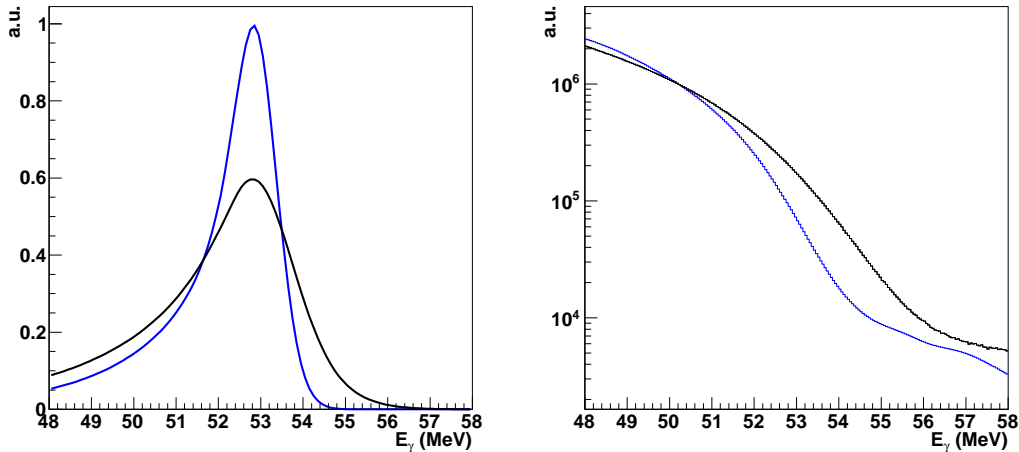


FIG. 84: Comparison of photon energy PDF for signal events (left) and accidental background events (right) based on the resolutions obtained in 2010 data (black) and on the projected value for the upgrade (blue). Differences in relative background contributions between RMD, AIF and pileup are also taken into account.

The *toy MCs* are generated assuming zero signal events and an average number of radiative and accidental events obtained by extrapolating the previous years results and taking into account the new detector performance. The number of radiative and accidental events is then left free to fluctuate, according to Poisson statistics. A maximum likelihood fit is performed and an UL on the number of signal events is determined for each *toy MC*; this value is then converted to an UL on  $\mathcal{B}(\mu \rightarrow e\gamma)$  by using the appropriate normalization factor. We define as *sensitivity* the median of the distribution of the UL obtained on the *toy MCs*.

In Fig. 85 we show the evolution of the sensitivity as a function of the DAQ time (in weeks). With a muon stopping rate on target of  $7 \times 10^7 \mu/\text{sec}$  and a target thickness of  $140 \mu\text{m}$  and assuming 175 DAQ days per year, we expect to reach a final sensitivity of about  $6 \times 10^{-14}$  in 3 years of running. We note that

the sensitivity is calculated based on the improved detector performance shown in Table XI, but it has an approximately 30% ambiguity according to possible different scenarios in the performance improvement.

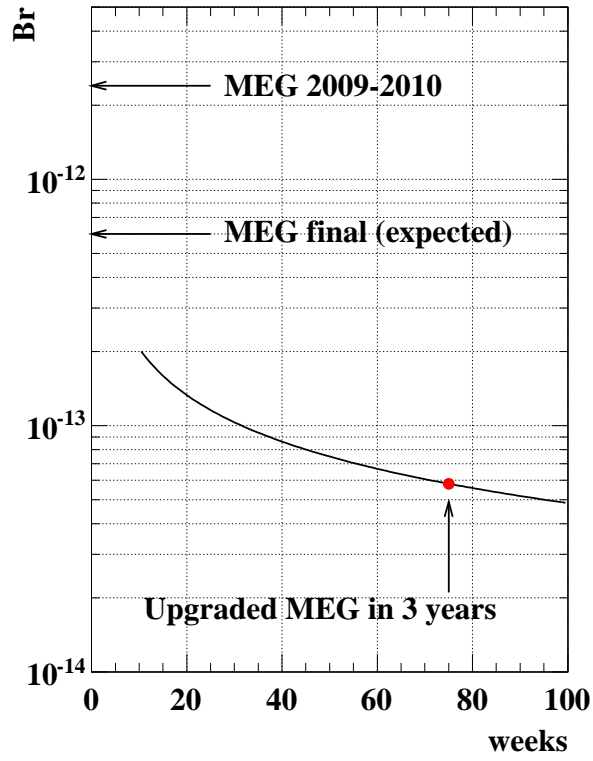


FIG. 85: Expected sensitivity of upgraded MEG as a function of DAQ time in weeks. Assuming 175 DAQ days per year, we expect to reach an UL on  $\mathcal{B}(\mu \rightarrow e\gamma)$  of  $\approx 6 \times 10^{-14}$  in 3 years of running.

## X. COSTS AND RESPONSIBILITIES

We present here detailed cost estimates for the construction of the different parts proposed for this upgrade, namely the upgrade of the xenon calorimeter (Tab. XII), the new timing counter (Tab. XIII), the DAQ upgrade (Tab. XIV) and the new drift chamber (Tab. XV). The proposed subdivision of responsibilities for the construction of the individual items is shown in Tab. XVI.

TABLE XII: Cost estimate for the liquid xenon calorimeter upgrade

Item	Cost (k€)
LXe (180 liters)	340
UV-SiPM	720
Cables	369
Connectors	149
Feedthrough	1
PCB (inner slab)	1
Refrigerator	40
PMT holder (lateral faces)	10
Radiative decay veto	12
<b>Total</b>	<b>1642</b>

TABLE XIII: Cost estimate for the new pixelated timing counter

Item	Cost (k€)
SiPM	68
Scintillator	11
Support structure	20
Cables	47
PCB	2
Connectors	17
Laser for calibration	20
Optical fibers	21
<b>Total</b>	<b>206</b>

TABLE XIV: Cost estimate for the DAQ upgrade

Item	Cost (k€)
Trigger concentrator boards	90
Clock distribution cables and ancillary boards	10
Total Digitizer Cost (7400 channels)	815
<b>Total</b>	<b>915</b>

TABLE XV: Detailed cost estimate for the new Drift Chamber

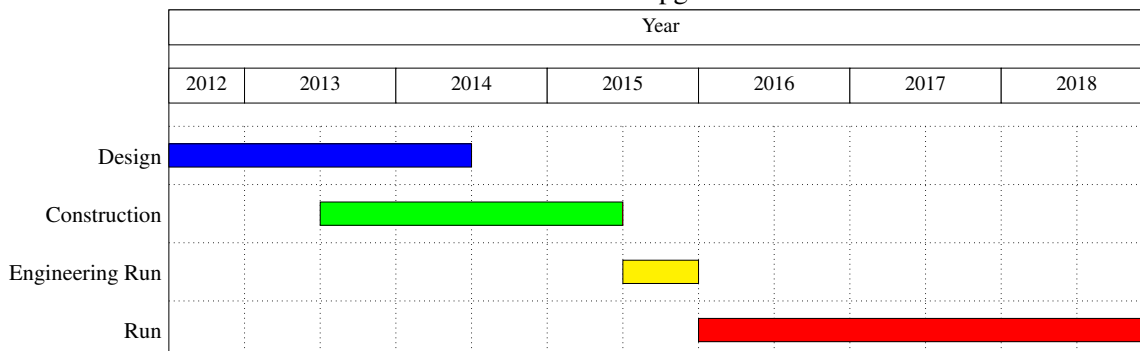
<b>Prototype</b> (full length wedge 128 ch.)		<b>98 k€</b>
Mechanics	<i>endplates (fabrication, machining, drilling)</i>	8
	<i>supports</i>	4
	<i>Testing jig</i>	6
Materials	<i>wires and supports</i>	24
Tools	<i>soldering, cleaning</i>	4
Quality Control	<i>mech. tension, alignment</i>	8
Front End	<i>preampl. + driver, LV power supply cables + connectors</i>	16
HV	<i>power supply + distribution</i>	28
<b>Chamber end plates + support structure</b>		<b>174 k€</b>
Project design	<i>Software licenses + engineering</i>	36
Model construction for end plates		12
E.P. Fabrication		30
E.P.Drilling		16
Measuring	<i>dimensional, stress and deformation checks</i>	10
Inner and Outer Cylinders Fabrication and Machining		40
Support Structure Skeleton		18
Assembling Jig	<i>incl. glueing and gas sealing flanges</i>	12
<b>Chamber Wiring and Construction</b>		<b>160 k€</b>
Clean Room Utilization		20
Mechanical Structure		10
Positioning and Alignment monitoring		10
Full Length Wiring Machine		40
Tools		10
Materials	<i>wires, supports</i>	70
<b>Front-end, Electronics, HV system</b>		<b>260 k€</b>
Front-end (2400 ch.)	<i>preamp., driver, cables, connectors, LV supply</i>	200
HV System	<i>supply + distribution</i>	60
<b>Gas system</b>		<b>94 k€</b>
Flow controller + Mass flow meters + Pressure sensors		32
Infrared analyzer for hydrocarbons		18
O <sub>2</sub> /H <sub>2</sub> O monitor		18
Gas distribution		16
Monitor chamber		10
<b>Total</b>		<b>786 k€</b>

TABLE XVI: Subdivision of the construction responsibilities

<b>Item</b>	<b>Nation</b>	<b>Responsibility</b>
Liquid xenon	Japan	SiPMs, LXe, Cryogenics
Drift Chamber	Italy	End-caps, Wiring, FE electronics, HV
	Switzerland	Mechanical integration, Gas-System
Timing counter	Italy	SiPMs, Support structure
	Japan	Scintillator, Laser system, Cables/Connectors
	UCI	
DAQ	Italy	Trigger boards
	Switzerland	WaveDREAM boards

## XI. TIME SCHEDULE AND MAN POWER

Gantt chart 1: Overall MEG Upgrade Schedule

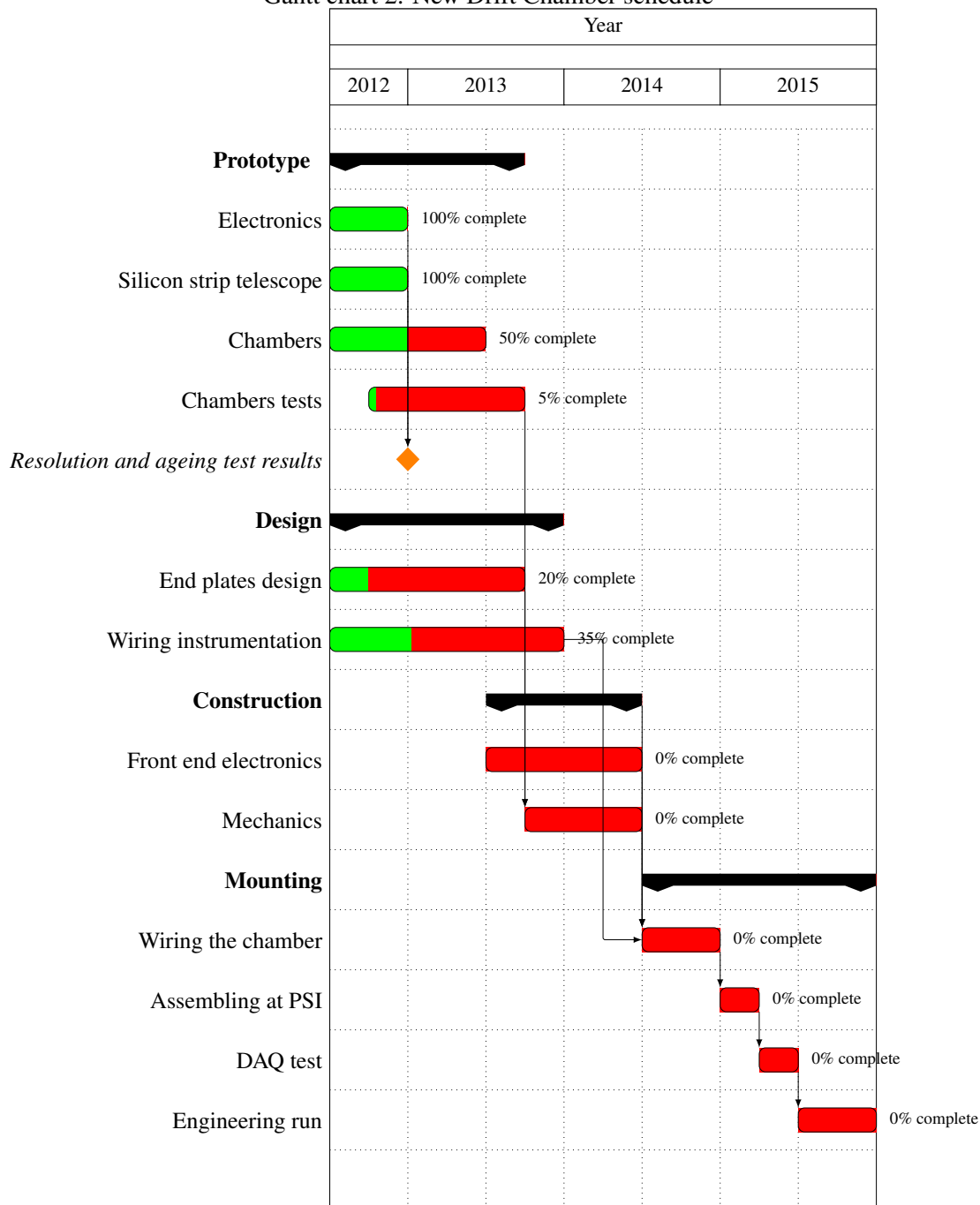


The overall planned schedule for the upgrade and its implementation is shown in figure 1. The initial period of design and construction will be followed by an engineering run in 2015. After that three years of data taking are foreseen.

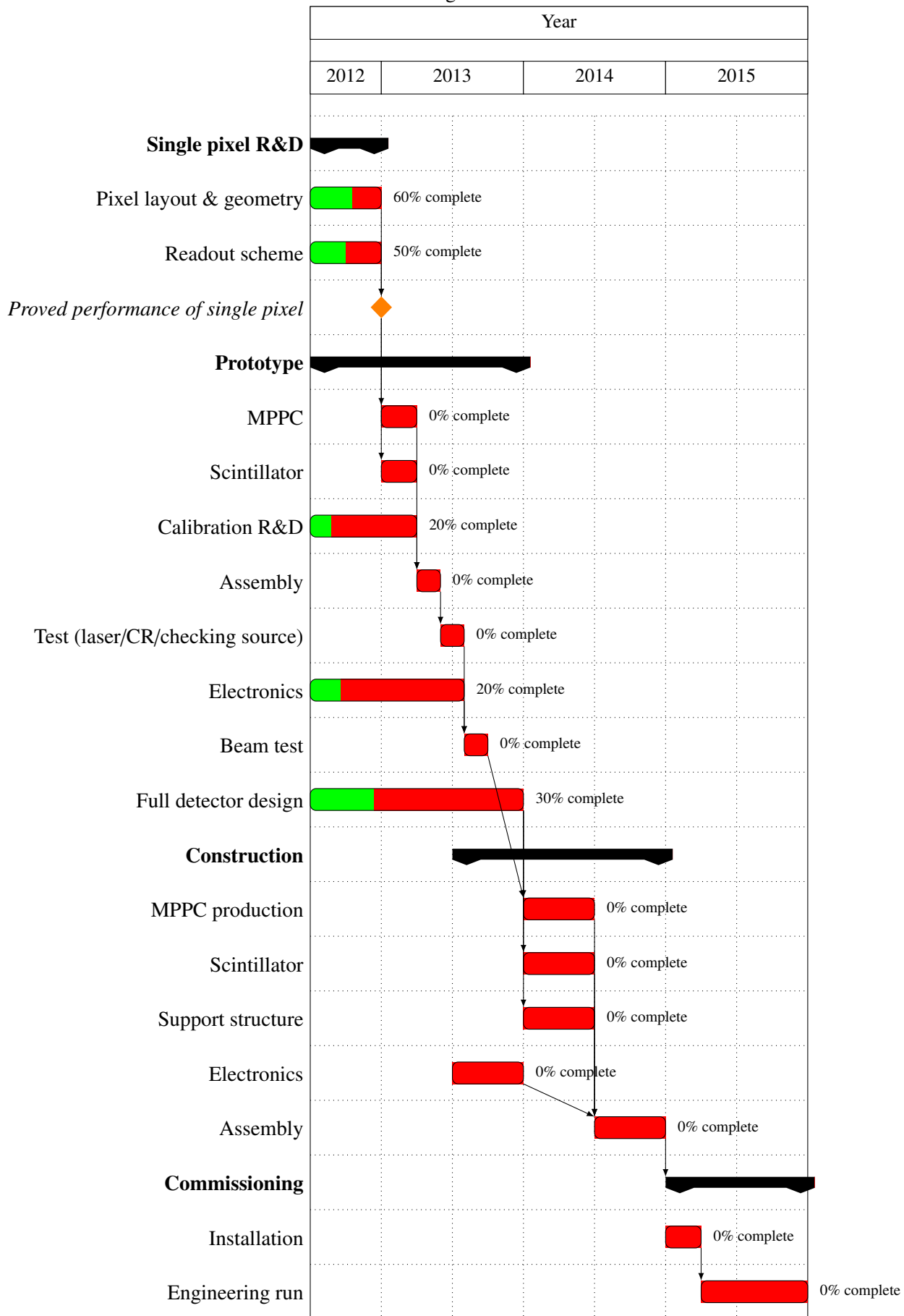
The time schedule for the final R&D tests and construction are presented for the new MEG drift chamber (Gantt chart 2), the new Timing Counter(Gantt chart 3), the modifications to the liquid xenon calorimeter (Gantt chart 4) and the DAQ system (Gantt chart 5). The starting time of these schedules is the time of preparation of this document, namely end of July 2012. We may note that some R&D have already started since some time.

In Table XVII we further show the number of full time equivalent (FTE) researchers for the different construction items as a function of time.

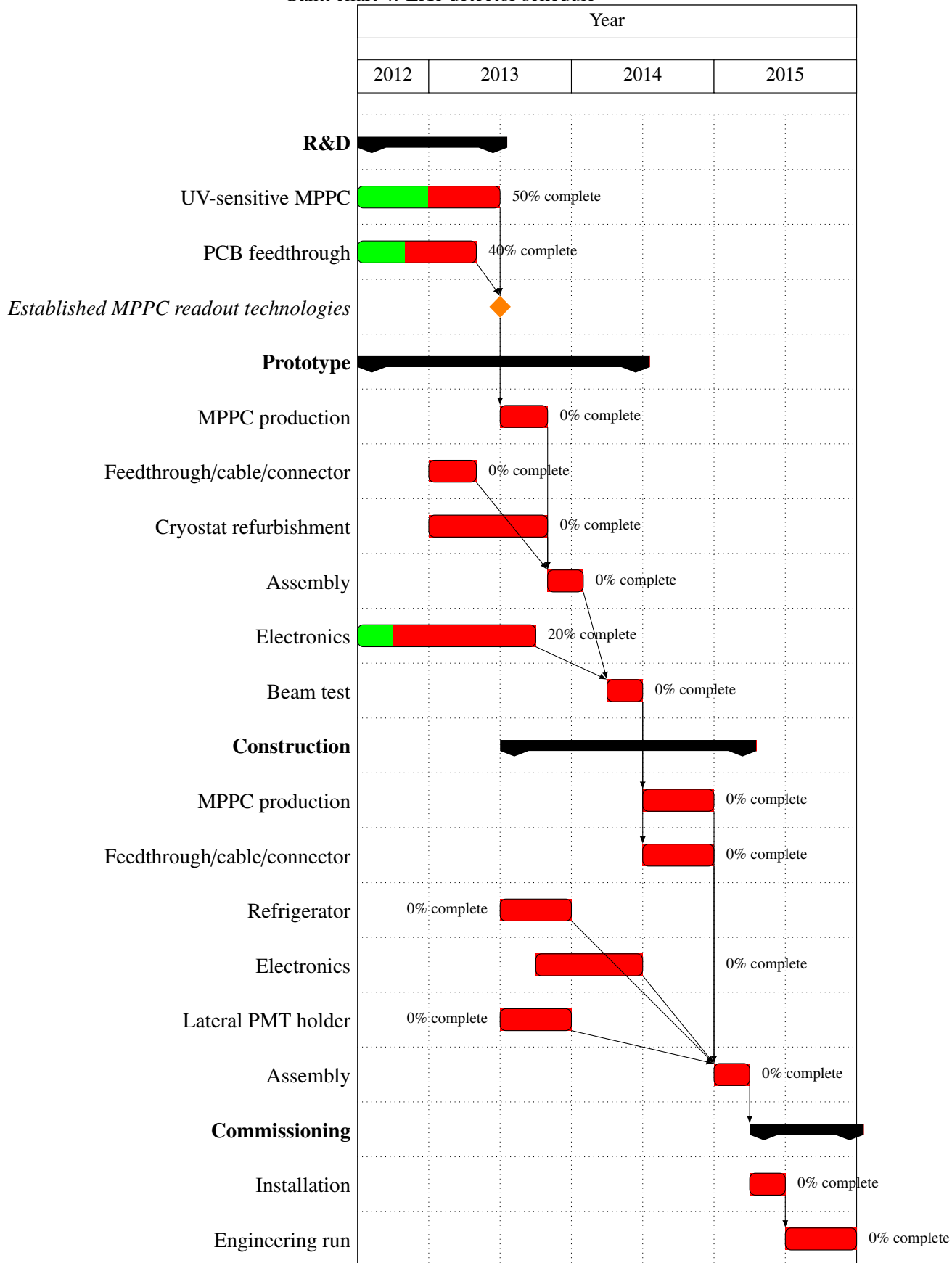
Gantt chart 2: New Drift Chamber schedule



Gantt chart 3: Timing counter schedule



Gantt chart 4: LXe detector schedule



Gantt chart 5: DAQ schedule

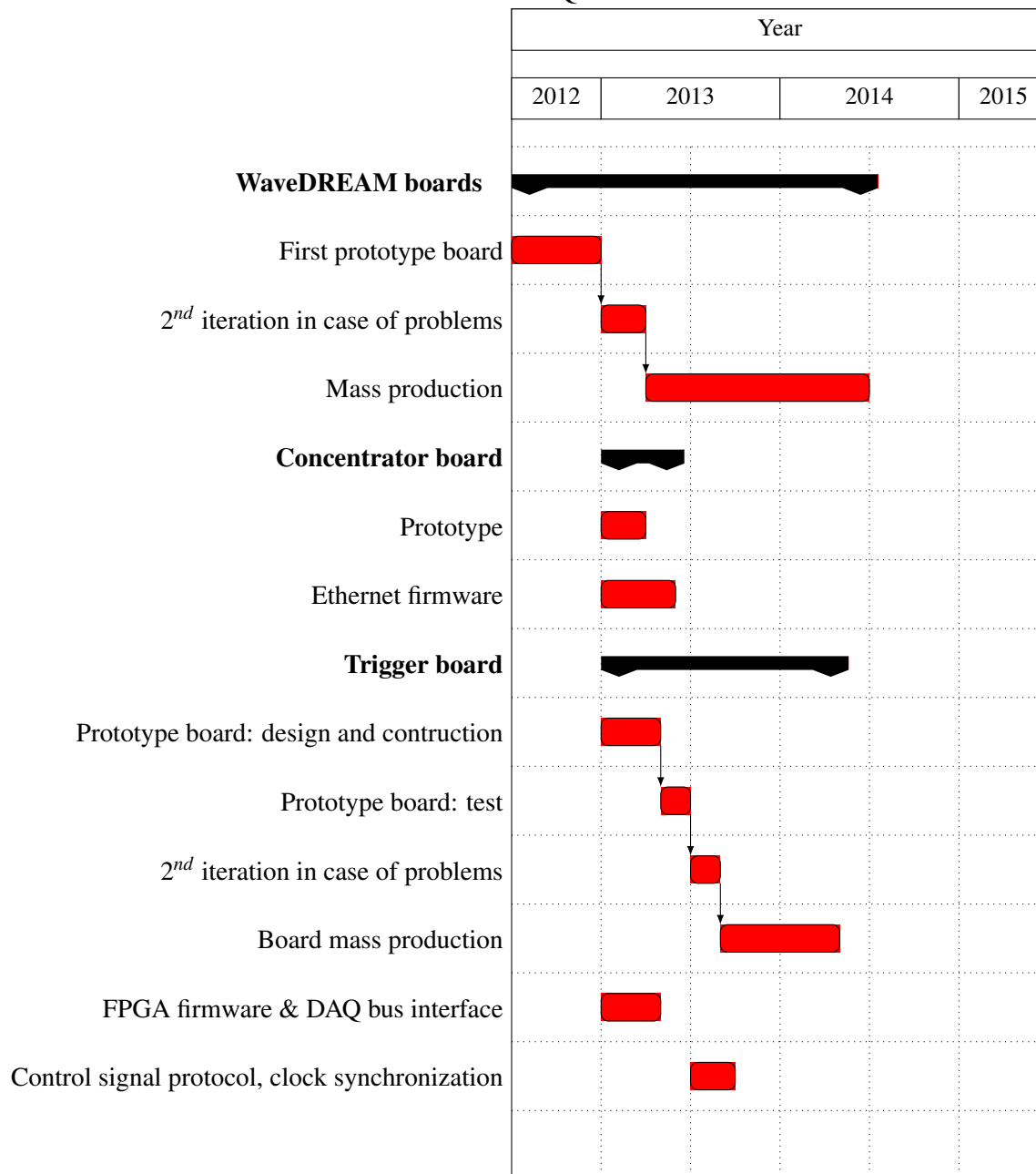


TABLE XVII: FTE researchers as a function of time for the different tasks

Item	Months									
	6	12	18	24	30	36	42	48	54	60
Beamline and Target	3	3	3	3	3	3	2	2	2	2
Drift Chamber	11	11	11	12	12	12	7.5	3.5	2.5	2.5
Timing Counter	9.6	9.6	10.1	10.1	10.1	10.1	5.6	5.6	3	3
Liquid Xenon Calorimeter	7	7	9	9	9	9	4	4	4	4
Trigger & DAQ	2.5	2.5	2.5	3.5	3.5	3.5	2.5	2.5	1.5	1.5
Analysis	3	3	3	3	3	3	15.5	19.5	21.1	21.1
<b>Total</b>	36.1	36.1	38.6	40.6	40.6	40.6	37.1	37.1	34.1	34.1

## XII. SUMMARY

The MEG experiment upgrade we propose with this document aims at reaching a sensitivity down to  $\mathcal{B} \simeq 6 \times 10^{-14}$  in the search of the  $\mu \rightarrow e\gamma$  decay. This is a very ambitious goal of extreme scientific interest, since a positive observation of the  $\mu \rightarrow e\gamma$  decay would represent the opening of a new world of phenomena in the field of particle physics. The proposed upgrade is competitive even with future projects like COMET or Mu2e, whose budgets are orders of magnitudes higher than what is needed for the MEG improvements.

It is however a really difficult task since in MEG we have to struggle with the rising wall of the accidental background which quadratically increases as a function of the muon stop rate. In order to accomplish it we need to deeply modify the liquid xenon calorimeter read-out and build new devices for measuring the positrons kinematical variables. We presented in full detail the selected solutions, their costs, the manpower involved in their realization and described the R&D tests that will be completed before the end of the year to make us sure that we will be able to reach the planned sensitivity goal.

The chosen solutions are somewhat conventional since we believe it is important not to exceed a total time of the order of 5 years for the construction and running of the apparatus: a time schedule which also fits well within the international context of cLFV searches. Less conventional solutions were however studied and described in the Appendix section.

Finally we would like to remark that the estimates and extrapolations we present in this document are firmly based on the results of a running experiment. The MEG international team of physicists has been successfully collaborating for a period of about 10 years; the total budget we are requiring roughly corresponds to 30% of the original MEG construction budget.

### XIII. APPENDIX

In this section an overview of related non-baseline upgrade studies is reviewed. These consist of complementary and alternative technologies that were considered as areas of potential for an upgrade programme. The scope of such on-going studies is rather broad and spans four main areas of interest:

- Tracking - (Active Target ATAR, TPC-based Tacker and a Si-based Vertex Tracker SVT)
- Diagnostics - (Active Target ATAR)
- Background Suppression - (Radiative Muon Decay Veto Counter RDC)
- Generic detector R&D - (LXe PMT Development, Timing Counter generic Scintillation Material Studies)

The devices described are also at different stages of R&D and development and some could, after development and successful testing and providing no serious background issues are discovered, be integrated into a running upgrade programme. However currently, these devices are not considered as part of the baseline solution presented in this proposal.

#### A. The Active target option

##### 1. Active target concept

We consider in this section the possibility to complement the new proposed MEG spectrometer with an active target [49]. The active target has two aims: 1) to improve the determination of the muon decay vertex and consequently to achieve better positron momentum and angular resolutions; 2) to continuously measure the muon stopping rate and therefore provide a direct evaluation of the detector acceptance (or an absolute normalization of our data). The former will be achieved by detecting the emerging positron using a single layer of 250  $\mu\text{m}$  fast scintillating fibres. This measurement is challenging since only a 30 keV mean energy deposit is expected from minimum ionizing particles in such a thin scintillating material. Stringent requirements must be satisfied to minimize positron multiple scattering and  $\gamma$  background from positron annihilation in the target materials. Therefore the target must have a minimal thickness and consist of low-Z materials. It must also have a fast response time to sustain the high rates and be able to operate in a high magnetic field environment (1.3 T). The muons ranging out into the target will provide the measurement of the stopping rate. The high target segmentation is a benefit also for this purpose. Muon and positron

signals can be distinguished by their large difference in energy deposit in the detector, as described in section XIII A 3.

*a. The muon decay vertex measurement* The position of the muon decay vertex can be determined by detecting the stopping muon or the emerging positron.

- **Muon detection.** In this case a spatial correlation must be used to connect the muon signal detected by the target, with the positron track measured by the spectrometer. The reconstructed positron track is extrapolated back to the target plane selecting only a small area. Only one fibre is expected to be fired in this area, which provides the muon position. This process is however rate limited to  $\approx 10^7$  particles/s, above which, muon multiplicities become larger than one and the efficiency of the method rapidly diminishes.
- **Positron detection.** In this case the positron detected by the target is timing correlated with the reconstructed track in the spectrometer, the positron time being provided by fast scintillators. This timing correlation can be used to have an external trigger on the target signal, which is fundamental to extract the expected weak positron signal as explained below.

With the proposed target a position resolution of  $\sigma_y < 100 \mu\text{m}$  is achievable and a timing resolution  $\sigma_t < 500 \text{ psec}$  is expected with a photo-electron statistics of about 10. A detection efficiency larger than 80% is desired.

## 2. Monte-Carlo simulations

In the current MEG experimental set-up there is no direct measurement of the muon decay vertex. Muons are stopped in a passive target (target thickness =  $205 \mu\text{m}$ , slant angle  $20.5 \text{ deg}$  relative to the beam direction) and the positrons from muon decay are detected, after traversing  $\sim 40 \text{ cm}$  He gas (at 1 atm pressure and room temperature). The muon decay vertex is determined by back-projecting the reconstructed positron track to the target plane. The measured performances of the present spectrometer coupled with a passive target are given in Tab. XVIII.

If an active target is used in a minimal configuration with only one single layer of horizontally mounted fibres, the measurement of the Y-coordinate can be performed which strongly constrains the positron momentum reconstruction. Fig. 86 shows typical positron momentum (left) and  $\phi$  angle (right) resolution distributions. The improved resolutions are summarized in Tab. XVIII.

Target/ Spectrometer	thickness ( $\mu\text{m}$ )/ angle (deg)	$\sigma_p$ (keV)	$\sigma_\phi$ (mrad)	$\sigma_\theta$ (mrad)	comment
Passive/old	205/ 20.5	320	11.7	9.8	measured
Passive/new	205/ 20.5	110	6.3	5.3	simulated
Passive/new	140/ 15	110	5.3	4.8	simulated
Active/new	250/ 20.5	90	4.7	5.1	simulated

TABLE XVIII: Measured positron momentum and angular resolutions with the present spectrometer (first row) . Monte Carlo simulation results for different target options coupled to the new spectrometer in  $\mu^+ \rightarrow e^+\gamma$  events are then reported.

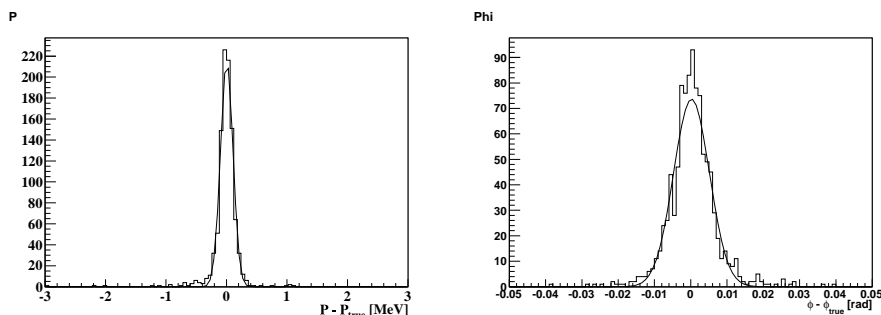


FIG. 86: Monte Carlo simulation of the positron momentum  $\sigma_p = 90$  keV/c (left) and the phi angle  $\sigma_\phi = 4.7$  mrad (right) resolutions of  $\mu^+ \rightarrow e^+\gamma$  events using an active target coupled with the new spectrometer.

### 3. Experimental set-up for R & D studies

The active target will be made from an array of 240 ( $0.25 \times 0.25$  mm<sup>2</sup>) multi-clad BCF12 (from Saint-Gobain) square fibres, with a peak emission at 435 nm, a light yield of about 8000 ph/MeV, a trapping efficiency of  $\approx 7\%$ , an attenuation length of 2.7 m and a decay time of 3.2 ns. Each fibre will be coupled to a single SiPM (Hamamatsu S10362-11-100C). The efficiency of this detector to be used was already optimized by using the SiPM with a detection efficiency (PDE) of 65% and a gain of  $2.4 \times 10^6$  (dark rate = 600 kHz at 0.5 phe).

*a. The positron detection from a muon decay vertex measurement* The main challenge is to detect minimum ionizing particles (m.i.p.) with high efficiency using  $0.25 \times 0.25$  mm<sup>2</sup> fibres. A set of measurements of a single fibre (BCF12) coupled to a SiPM (Hamamatsu S10362-11-50C) were undertaken. A  $\text{Si}^{90}$  source provides electrons with an end-point energy of 2.28 MeV. A plastic collimator mounted in front of the source ensured that a fraction of electrons goes through the fibre first before being stopped in a thick plastic scintillator (BC400 - diameter 20 mm x length 20 mm), coupled to a photomultiplier (Hama-

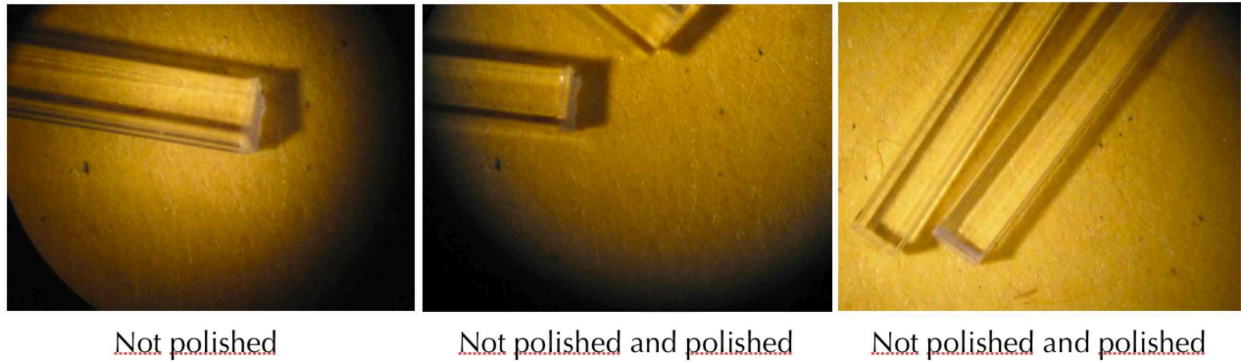


FIG. 87: Polishing of  $1 \times 1$ ,  $0.5 \times 0.5$  and  $0.25 \times 0.25$  mm<sup>2</sup> fibres with diamond head.

matsumoto R5900U). The plastic scintillator signal provides the trigger and suppresses the SiPM dark current background. An energy threshold of 1.5 MeV was set to select only minimum ionizing particles.

Several fibre thicknesses ( $1 \times 1$ ,  $0.5 \times 0.5$  and  $0.25 \times 0.25$  mm<sup>2</sup>) were tested. The measured number of photoelectrons scales, as expected, with the deposited energy, in all cases except for the 0.25 mm fibre, where slightly less light was collected due to a non-optimized mechanical and optical coupling. The signal from the SiPM was amplified by a factor 10 using a low-noise ( $< 10$  mV peak-to-peak) front-end preamplifier board (PSI made). The same board delivers the 70 V bias voltage to the detector. The data was acquired using the DRS4 evaluation board.

Fig. 88 shows the charge spectrum obtained as a result of a waveform integration over a fixed time window (15 ns). A mean of about 3 photoelectrons is measured to be compared with the expected 5. A m.i.p. detection efficiency was also measured to be  $\epsilon \sim 63\%$ .

**The fibre optimization.** The light collection, for instance, can be enhanced by depositing an aluminum reflector on the opposite end of the fibre to increase the detection efficiency. Samples of all fibre thicknesses were polished using a diamond milling head. Fig. 87 shows how the fibre surface appears under a microscope. An aluminum deposit was performed by painting or sputtering. The advantages of the sputtering method are that a known and uniform layer thickness can be deposited, in the range 10-1000 nm. Metallic and ceramic material can also be sputtered with the purity of the material kept under control. Unfortunately sputtering is time consuming. For  $1 \times 1$  mm<sup>2</sup> fibres an increase in the light collection of about 70% was obtained. Fig. 89 shows the obtained results using a  $1 \times 1$  mm<sup>2</sup> fibre without (left) and with (right) an aluminum deposit. An increasing in the light collection of about 1.75 was measured for both painted and sputtered Al. A similar result was obtained using painted Al on  $0.5 \times 0.5$  mm<sup>2</sup> and  $0.25 \times 0.25$  mm<sup>2</sup> fibres. Furthermore it was observed that the benefit of the Al deposit is strongly reduced or vanished (this is the

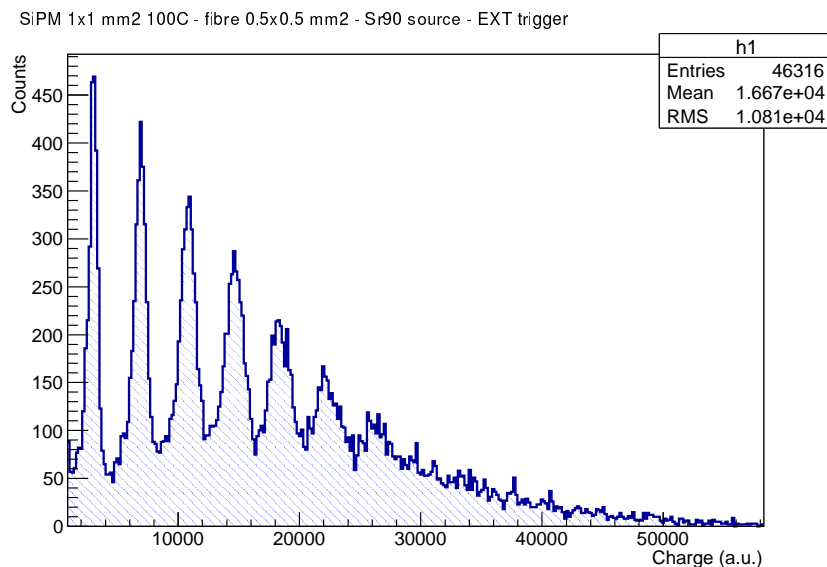


FIG. 88: Charge spectrum induced by minimum ionizing electrons in a  $0.25 \times 0.25 \text{ mm}^2$  scintillating fibre coupled to a SiPM Hamamatsu S10362-11-100C.

case e.g. for the smallest fibre) if the fibre surface is not polished. Fig. 90 shows the present best result for a painted Al  $0.25 \times 0.25 \text{ mm}^2$  fibre. A mean of 4.5 photoelectrons is measured and a m.i.p. detection efficiency of  $\epsilon \sim 80\%$  is measured. Some improvement in both light collection and detection efficiency can be expected glueing the fibre directly to the SiPM.

A sputtered  $\text{TiO}_2$  deposit is in preparation. The reflectivity of  $\text{TiO}_2$  is expected to be higher than that of Al. This could also increase slightly the light collection and the efficiency.

The sputtering method is also considered for a thin deposit ( $< 1\mu\text{m}$ ) on the sides of the fibre for light-tightness. Some samples are in preparation and will be tested it soon.

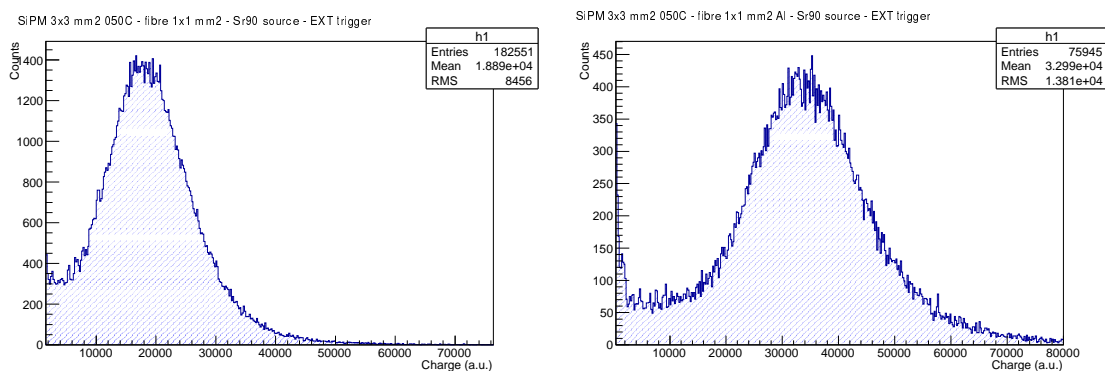


FIG. 89: Charge spectrum induced by minimum ionizing electrons in a  $1 \times 1 \text{ mm}^2$  scintillating fibre coupled to a SiPM Hamamatsu S10362-33-50C to one fibre end, without (left) and with (right) aluminum deposit on the other end.

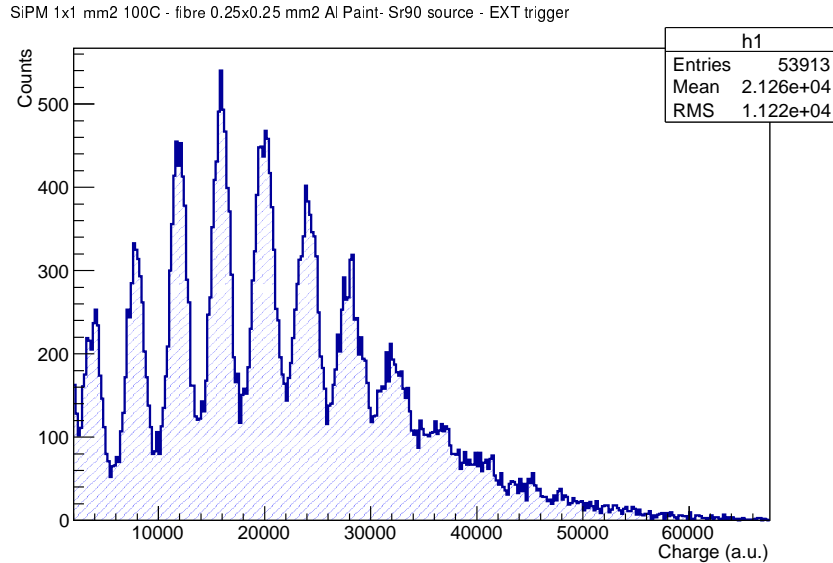


FIG. 90: Charge spectrum induced by minimum ionizing electrons in a painted Al  $0.25 \times 0.25 \text{ mm}^2$  scintillating fibre coupled to a SiPM Hamamatsu S10362-11-100C.

*b. The muon detection for muon stopping rate measurement* The muon detection study was performed using a layer of 4 round fibres (BCF-12, diameter 0.5mm) coupled to SiPM (Hamamatsu S10362-33-50C) at the PSI  $\pi$ E1 beam line, tuned to positive muons of 28 MeV/c (the same as used in MEG). The muon intensity was about  $2 \times 10^6 \mu/s$ . A typical waveform amplitude distribution is shown in Figure 91. A scan of the collected light as a function of the muon momentum was performed inserting  $50 \mu\text{m}$  thick mylar foils in front of the fibres until the muons are stopped in it. The muon signal is clearly visible for all the various different energy deposits.

*c. Event selection* **Positron selection.** For  $10^8$  muon stopped per second, a rate of  $2 \cdot 10^6$  event/s per fibre  $0.25 \times 0.25 \text{ mm}^2$  is expected. Two-fold are the main background sources for positron signal selection: the thermal noise and the muon stops. The first is present since the positron signal is expected to be at a level of few photo-electrons and therefore at the same level of the thermal noise, with a rate of few hundred KHz (in the best case). The second since the higher muon signal could overlap with the positron one. This muon signal can come from uncorrelated muons hitting the same fibre fired by the positron or from the stopping muon from which the positron originates. Both can be rejected using the Timing Counter detector as an external trigger (MEG trigger) in a time window of 20 ns. All the listed backgrounds are reduced to a contamination level of a few percent. In conclusion the positron selection efficiency based on an external trigger is expected to be  $\geq 95\%$ .

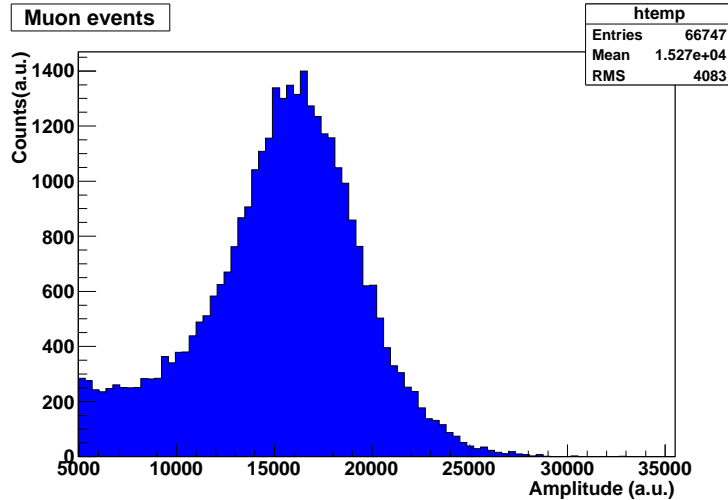


FIG. 91: Waveform amplitude spectrum induced by muons of 28 MeV/c in a 0.5 mm (diameter) scintillating fibre coupled to a SiPM Hamamatsu S10362-33-50C.

**Muon selection.** The muon rate can be measured setting a relatively high amplitude threshold, which removes completely the positron and thermal noise contributions.

#### 4. Conclusion

In conclusion, preliminary tests have shown that minimum ionizing particles can be detected with 250  $\mu\text{m}$  scintillating fibres coupled to SiPM. The light collection and the detection efficiency was increased using an Aluminum deposit on the polished free one-end of the fibre. A detection efficiency of approximately 80% was measured. A different reflector ( $\text{TiO}_2$ ) is in preparation and could improve the light collection and the detection efficiency even more. The positron signal is clearly detected rejecting the thermal noise with an external trigger. No cooling system for the SiPM is needed. The large pulse-height difference between positron and muon allows one to distinguish between the two particles. A prototype is under-construction in order to finalize the project.

#### B. Radiative muon decay veto counter : RDC

The dominant source of  $\gamma$ -rays in the accidental background events in the MEG analysis window is the radiative muon decays (RMD). In the present detector, 53% of  $\gamma$ -rays above 48 MeV are from RMDs and the fraction is more in the upgraded detector because of the reduced background  $\gamma$ -rays thanks to the new positron tracker. In a radiative decay with a high energy  $\gamma$ -ray, a low momentum positron, typically lower than 2 MeV, is emitted in a high probability. On the other hand, in Michel decay, the probability of a muon

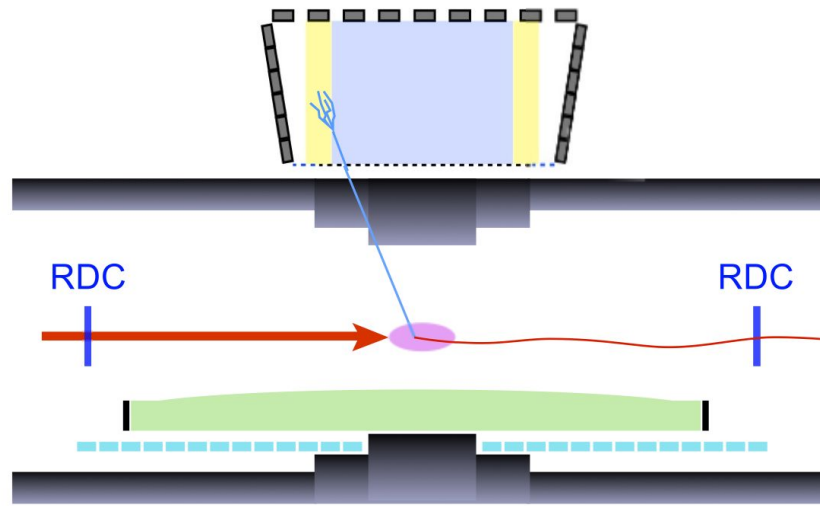


FIG. 92: A configuration of the upgraded detector with radiative decay counters located at the both ends of the spectrometer. In this figure, a high-energy  $\gamma$ -ray and a low-momentum positron from a muon decay on the target are detected by the LXe detector and the downstream RDC, respectively.

to decay with such a low momentum positron is low. In the CrystalBox detector [50], RMD events with low momentum positrons were clearly detected and used in the physics analysis, which discarded 12.3% of the candidate events with a loss in the signal detection efficiency of 0.5%. In the MEGA experiment [51], internal bremsstrahlung veto counters (IBV) were mounted to detect low momentum positrons. The original design was to decrease 80% of background events. However those counters were not used in the final physics analysis because only 3.5% of high energy  $\gamma$ -rays with a pair positron were detected with IBV hits, and the rate was independent of the  $\gamma$ -ray energy.

In the MEG detector, the bending radii of those low momentum positrons are typically smaller than 4 cm and 9 cm at the center and the end of the magnet, respectively. The radiative decay veto counters (RDC) therefore have to be mounted on the muon beam axis. The detection of the low momentum positrons can be done using plastic scintillation counters of about  $250\mu\text{m}$  thickness. The counter at the upstream side is used also to reduce the momentum of the muon beam. By removing or thinning the degrader in the beam transport solenoid, which is presently  $300\mu\text{m}$  thick Mylar, the total thickness of the material before the target can be the same as the present detector.

A RDC module consists of 192 vertically aligned scintillation fibers and several scintillation plates. The thickness of the fibers and plates is  $250\mu\text{m}$ . The fibers are used at the central part to minimize the dead-time due to the high hit-rate, and the plates are used at the edge parts of the counter to not increase number of

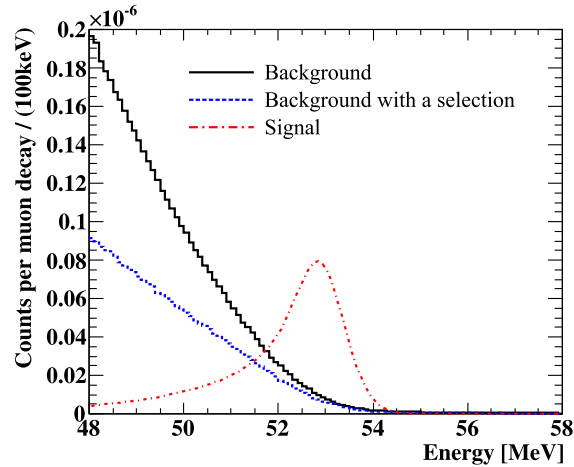


FIG. 93: Simulated spectra of  $\gamma$ -rays detected by the upgraded LXe detector. The dotted blue histogram shows a spectrum after a rejection of RMD events identified by RDC. The signal spectrum is arbitrary scaled.

read-out channels too much. Scintillation photons are transported through optical fibers. Sixteen optical fibers are bundled and coupled to a  $1 \times 1 \text{ mm}^2$  SiPM. In total 28 SiPMs are used for the upstream and the downstream RDCs.

The performance of RDC was studied using MC simulation by inserting thin plastic scintillators at the both ends of the magnet (Fig. 92). The position is far from the center of the magnet and outside of the tracking volume; therefore neither the significant increase of background  $\gamma$ -rays nor the reduction of the signal detection efficiency are expected. The tagging efficiency of radiative muon decays was evaluated to be 70% for radiative decays with  $\gamma$  energy higher than 48 MeV when the coincidence time window between RDC and the LXe detector is chosen to be 8 nsec. Figure 93 shows a spectrum of background  $\gamma$ -rays detected by the upgraded LXe detector, and the same after a rejection of RMD events identified by RDC. The probability for signal events for coinciding accidentally with RDC hits is about 15% for the same coincidence time window. Instead of using RDC for rejecting signal candidate events, the probability density function of the time difference between a RDC hit and a  $\gamma$ -ray detected by the LXe detector can be included in the physics analysis so that signal efficiency is not reduced.

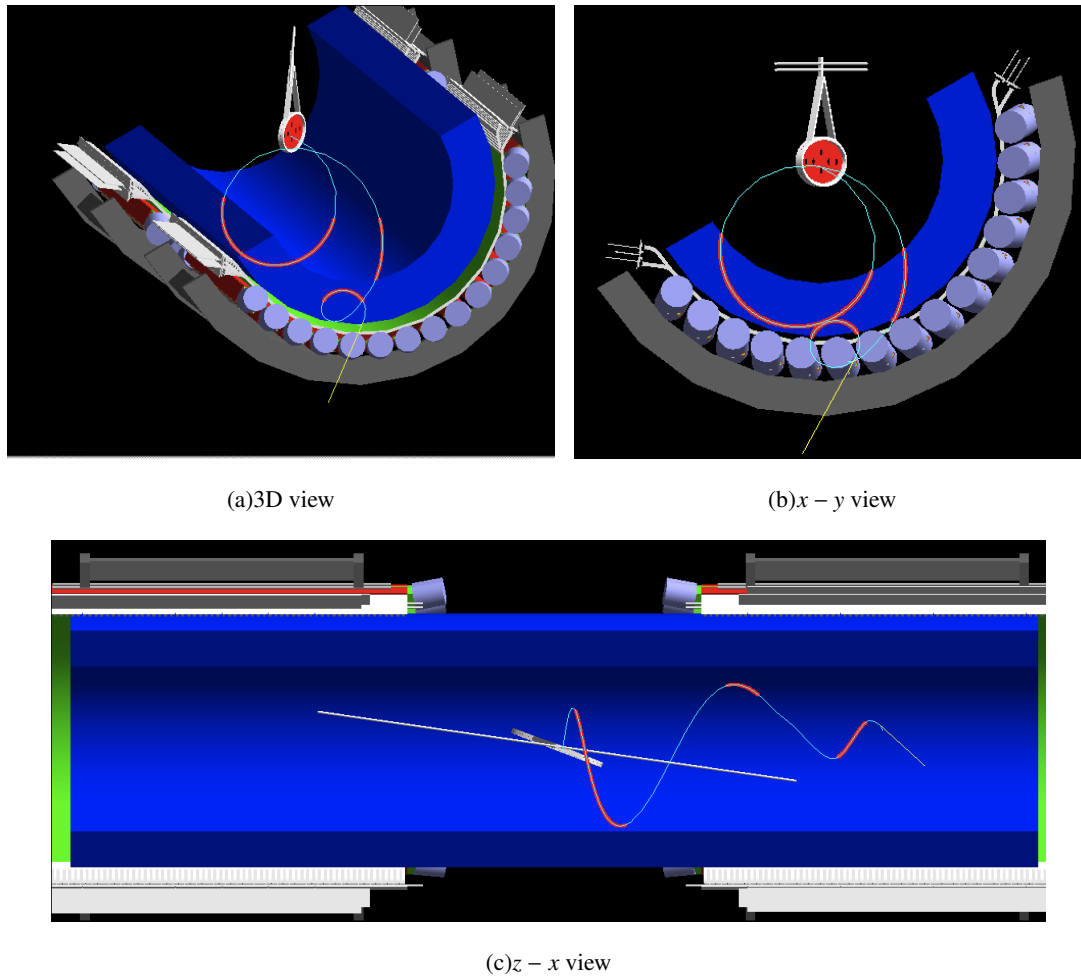


FIG. 94: Event display of TPC-based tracker by Geant4-base simulation with three view points. Blue trajectory indicates the generated positron and red indicates the hits recorded in the TPC fiducial, respectively.

### C. TPC-based tracker option

#### 1. Concept

As one of alternatives for the positron tracker, a Time-Projection-Chamber(TPC)-based tracker was considered for the upgrade.

The TPC provides a complete 3-dimensional (3D) pictures of the ionization deposited in an active gas volume. It acts somewhat like a bubble chamber. The TPC's 3D localization makes it extremely useful in tracking charged particles in a high-track-density environment. This can improve the MEG positron spectrometer performance in a significant way.

As described in the previous sections, we aim to improve the detection efficiency of the positron spectrometer by reducing the amount of material used in the components. In the present tracker, the amount

of material existing inside the fiducial volume is substantially small while there is significant amount of material in between the drift chamber and timing counter; this cause deterioration of the position detection efficiency. The proposed drift chamber design solves this problem by adopting a unique gas volume. The TPC design also takes the same approach to address this.

In addition to this we plan to improve the tracking accuracy by increasing the number of sampling points along a positron track. The present tracker system is based on the modularized drift chambers, and thus, the number of possible ionization positions, the so-called *hits*, is limited. Consequently, the reconstructed momentum resolution and angular resolutions are somehow limited. With this principle, the TPC-based tracker is also possible to bring tremendous improvement for that, because the TPC can provide a complete 3D pictures of charged track in its fiducial volume.

In order to adopt the TPC-based detector idea for the MEG positron spectrometer, there is one important issue to be addressed first, namely, the orientation of time-projection. The commonly adopted method by many experiments is projecting the charged trajectory onto the plane which is perpendicular to the beam axis, *i.e.* projecting along the beam axis. However, it is difficult to adhere the same idea for the MEG positron spectrometer, because of the limited space to install the front-end electronics. In addition, very long projection distance is necessary in case we adopt time projection along the beam axis, approximately 3 m, which will potentially lead to a technical problem to maintain the electric field, and also poor spatial resolution caused by electron diffusion during drift.

In consequence, for the MEG positron spectrometer, we have to adopt the “radially-projecting” TPC which consists of:

- electrodes which establish an electric field to make electrons drift radially, and
- electron detection device cylindrically curved to fit the shape of the inner face of the COBRA magnet.

In order to investigate the possibility to realize such a challenging detector idea, intensive simulation work is progressing, and some prototypes are being planned. The simulated event display for the TPC-based positron spectrometer is shown in Fig. 94 with three different view points.

## 2. Design

At first, in order to have a look at the time-projection as described in the previous sub-section, the calculated electric field is implemented in the MC framework. Here we assume the 9 cm of maximum drift distance and curved electrode to be matched with the volume inside COBRA magnet. Fig. 95 (a) shows

the obtained electric field map which is calculated by the commercial FEA program [23]. In this example, 9 kV is applied on the anode, and field-cage wires are equipped at 5 mm intervals at both ends of fiducial volume,  $y = 0$ , in order to maintain the uniformity of electric field. By extracting this calculated electric

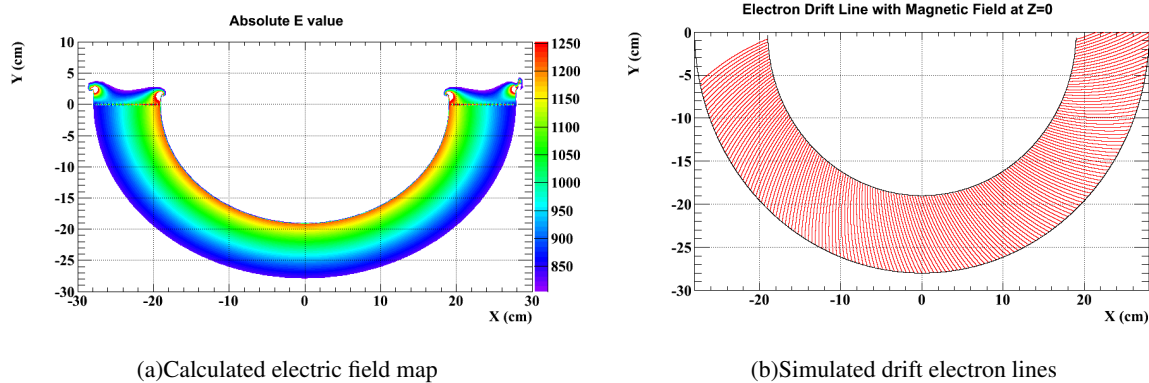


FIG. 95: Calculated field map and drift-line.

field map with the COBRA magnetic field map, the time-projection trajectory inside the fiducial volume can be obtained as shown in Fig. 95 (b). In this figure,  $z = 0$  of coordinate is adopted as an example to determine a cut view, because COBRA magnetic field is highly graded. As shown in this figure, even if we have a graded magnetic field, each ionization position can be reconstructed by the combination of  $z$ -coordinate and the projection time uniquely.

Thus, now it is required to consider how to measure the  $z$ -coordinate reasonably. The front-end detector of TPC is normally realized by a wire-chamber-base detector or a MPGD<sup>4</sup>-base detector. For our case, the projection plane is cylindrical, hence the MPGD-base detector, like GEM [52], is suitable. However, now we are facing the next issue, *i.e.* we have to build a cylindrical GEM detector to cover the inner surface of COBRA magnet. So far, three cylindrical GEM detector have been successfully fabricated in the particle/nuclear experimental field: (1) NA61 tracker at CERN [52], (2) KLOE upgrade detector at LNF [53], and (3) BoNuS TPC at JLab [54]. Thus, in principle, it has been established to build the cylindrical GEM detector technically, nevertheless it is very difficult to keep the precise gaps between each GEM layers over the all cylindrical surface. Two examples of the fabricated cylindrical GEM detector are shown in Fig. 96. Furthermore, all realized detectors so far are not big size,  $\sim 20$  cm of diameter at maximum, while it is required to build a  $\sim 60$  cm of diameter cylindrical GEM for the MEG positron spectrometer.

<sup>4</sup> Micro Pixel Gas Detector



(a)Cylindrical GEM for NA61 at CERN



(b)Cylindrical GEM for KLOE-2 at LNF

FIG. 96: Examples of the cylindrical GEM detector.

Front-end detector for the TPC may be realized by the cylindrical GEM detector, on the other hand, we have to carefully consider how to build the electrode to maintain the TPC electric field. Such an electric field should be;

- high field ( $\sim 1$  kV/cm), and
- precisely uniform (or precisely controlled).

Fig. 97 shows how electric field uncertainties affect the tracking performance in the MC simulation. Both plots in Fig. 97 show the difference of projected time with some perturbed electric fields. In Fig. 97 (a), the electric fields are scaled by 0.1, 0.5, and 1 %, respectively, while the electric fields are randomly perturbed by factor of 0.1, 0.5, and 1 %, respectively, in Fig. 97 (b). According to these results, a randomly fluctuated electric field does not have a severe effect on the tracker performance, while scaled fields lead serious systematic uncertainties. In consequence, in order to obtain a reasonable spatial resolution by means of time-projection, 0.2 % of electric field uniformity is required at worst.

It is necessary to actualize such a good uniformity on the electric field by using the ultra-thin electrode foil, because all the incoming positrons pass through the inner surface of TPC, namely, the inner electrode, as clearly shown in Fig. 94. During the development of present MEG drift chamber, the specially dedicated technique to make a ultra-thin electrode foil which is  $12.5 \mu\text{m}$  thickness of polyimide with precisely patterned aluminum layer which is 250 nm of deposition thickness over 1 m length. This 250 nm of deposition thickness is compromised due to patterning precision, however, this deposition thickness can be reduced down to 50 nm level for the TPC detector, because patterning is not necessary for the TPC electrode. By

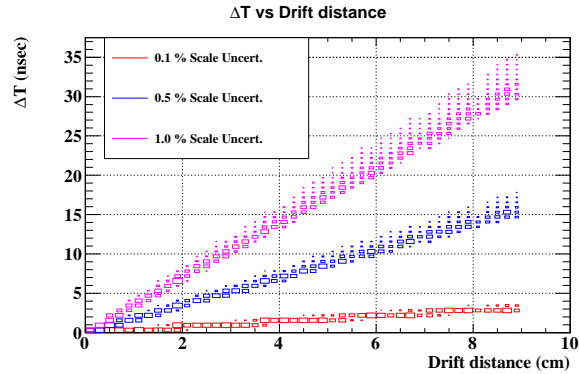
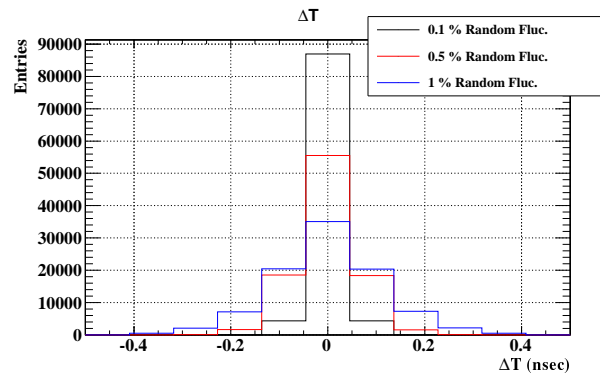
(a)  $\Delta T$  with scaled E-fields(b)  $\Delta T$  with randomly perturbed E-fields

FIG. 97: Projection-time differences as a function of electric field uncertainties

assuming 50 nm of aluminum deposition on the electrode foil, the required uniformity of electric field is achievable, nevertheless the fabrication method will be a next issue to be discussed.

### 3. Expected Performance

By implementing the items described in previous sub-sections, *e.g.* radial electric field with assumed precision, cylindrical GEM as a front-end detector of TPC, ultra-thin electrode foil, *etc.*, the detector performances are estimated by the MC simulation.

In the MC simulation, the following parameters are assumed;

- event generation: same as the present MEG MC
- gas mixture: He/CO<sub>2</sub>/C<sub>2</sub>H<sub>6</sub>(70% : 20% : 10%)
- diffusion coefficient:  $150\mu\text{m}/\sqrt{\text{cm}}$

- inner electrode: 40  $\mu\text{m}$  of polyimide with 1  $\mu\text{m}$  of Cu deposition

The event generation scheme is based on the present MEG MC simulation, and it would be further tuned, in particular, the event rate is varied to simulate the capability of possible high rate experiment. The gas mixture is currently assumed to use the He/CO<sub>2</sub>/C<sub>2</sub>H<sub>6</sub> mixture, however, almost nothing is decided yet about gas mixture, just a use of helium-base gas mixture is mandated, because multiple scattering effect should be one of the dominant source to deteriorate the tracking resolution for 52.8 MeV/c positron. In any case, the gas mixture is the most important item to study at the next step, not only for the simulation but also for the hardware R&D. Some numbers of diffusion coefficient are assumed to calculate the diffusion effect for the time-projection, and tentative electrode materials are also implemented even it is very conservative setting. The simulated track finding is shown in Fig. 98 with MC events. Fig. 98 (a) shows an example of track find-

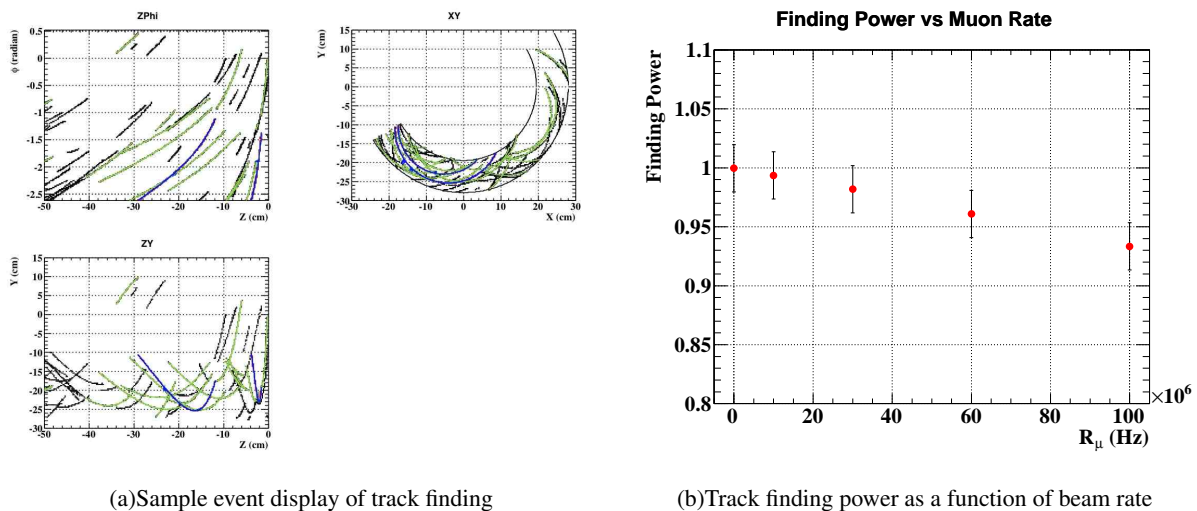


FIG. 98: Track finding simulation

ing; blue trajectory indicates the found signal track which fires a trigger while all others indicate the pile-up events. Fig. 98 (b) shows the obtained track-finding power as a function of the beam intensity. As shown,  $\sim 93\%$  of finding power is expected at the  $1 \times 10^8 (\mu/\text{s})$  of beam intensity. So far, we applied just a local clustering method to find the track. No fancy algorithms, like a Hough transformation, are applied any more.

After the track finding, track fitting is performed which is based on the Kalman-filter-base track fitter developed for the present MEG tracking code. Fig. 100 show the reconstructed momentum/angular resolutions as a distribution of residuals between the reconstructed and the true(MC) information. Of course, the accuracy of reconstruction strongly depends on the diffusion (gas mixture), intrinsic spatial resolution (pad size), *etc.*, and hence, the intrinsic spatial resolution dependence and the diffusion coefficient dependence of

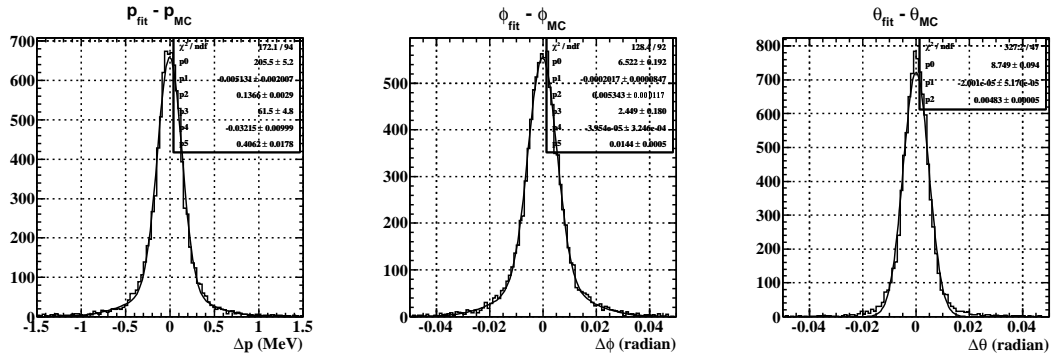


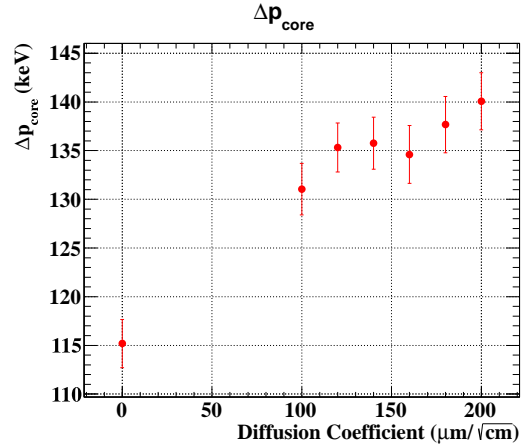
FIG. 99: Example of reconstructed momentum and angular resolutions

the track-reconstruction accuracy are also studied. According to the MC simulation studies, 130-160 keV/c of momentum resolutions could be expected depending on diffusions and spatial resolutions, as shown in Fig. 100. In addition to the momentum resolution,  $4 \div 9$  mrad of angular resolution and  $80 \div 90\%$  of detection efficiency are also expected.

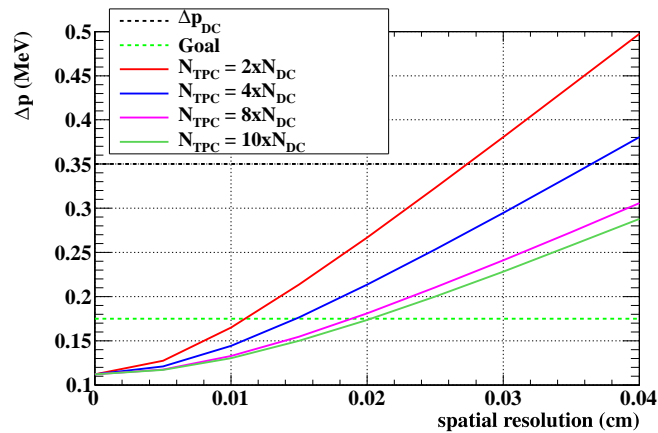
#### 4. Prototyping Plan

Here some prototyping plans are presented. First of all, it is certainly required to clarify if it is possible to build the cylindrical GEM detector even with larger dimension than the previously actualized detector which should be matched with our COBRA magnet geometry. Thus we are now building the first prototype which is shown in Fig. 101. As shown in this figure, a three layered GEM detector is adopted as the first prototype. The GEM foil has approximately  $10 \times 10 \text{ cm}^2$  of area and pattern characteristics is optimized for the E16 experiment at J-PARC, gap is 2 mm and  $10^4$  order of gain in total is expected. The most important challenge of this prototype is this three-layered GEM detector is bent with 30 cm of curvature which is corresponding to COBRA radius. This first prototype currently under construction will be used to study the following items:

- how to build the cylindrical GEM for COBRA,
- use of helium-base gas mixture for GEM,
- fundamental characteristics; *e.g.* gas gain, rate dependence, diffusion coefficient, efficiency, intrinsic spatial resolutions,
- behavior in the magnetic field, in particular, COBRA field.



(a) Resolution as a function of diffusion coefficient



(b) Resolution as a function of intrinsic spatial resolution

FIG. 100: Reconstructed momentum resolution studies

After this first prototype, we will be able to step into the second prototype which has much larger dimension.

#### D. Silicon vertex tracker option: SVT

##### 1. Concept

Solid state detectors have been widely used for tracking charged particles in high-energy physics. Recently silicon pixel detectors have been successfully implemented in LHC detectors to obtain high precision position resolution in high rate environments. The advantages to use such detectors are

- good stability of operation under high rate,

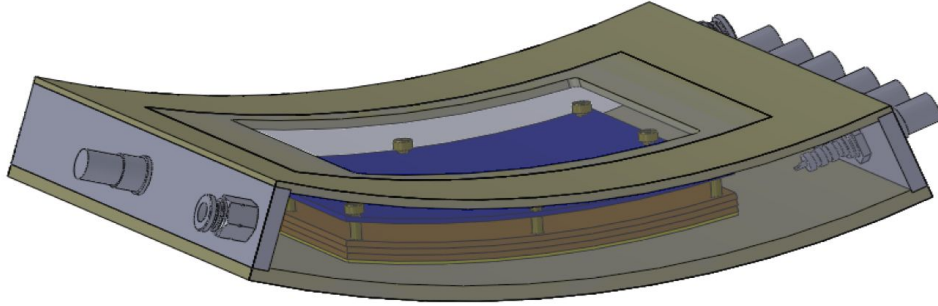


FIG. 101: 3D view of the first prototype of cylindrical GEM

- high rate tolerance with low occupancy,
- high spatial resolution ( $O(10 \mu\text{m})$ ).

These features are attractive for our upgrade project as well. However, those devices have been considered to be unsuitable for low energy experiments because of the material budget limiting the performance. To overcome this issue, many R&D are now under way mainly for future lepton collider experiments such as super B factories and ILC. Several devices such as DEPFET [55], MAPS [56], and SOI [57] are getting feasible for practical usage. With these new technologies very thin sensors down to several tens micro meter could be available in a few years from now. Among them, the High-Voltage Monolithic Active Pixel Sensor (HV-MAPS) [58] which is proposed to be used in the  $\mu \rightarrow eee$  experiment at PSI (Mu3e) [4] is in particular a good candidate, because many of the experimental requirements are shared between  $\mu \rightarrow e\gamma$  and  $\mu \rightarrow eee$  searches. Here, we propose an option of MEG-upgrade positron tracker using such new silicon device inspired by the Mu3e project.

In application to a  $\mu \rightarrow e\gamma$  search, one has to carefully design the detector to minimize the generation of photons becoming accidental background source. Not only positrons from  $\mu^+ \rightarrow e^+\gamma$  decays in acceptance region but also all possible particles have to be considered. The dimension of the tracker system is already fixed by the magnet. Because of the size, making a full tracker with silicon sensors is not feasible to fit our limited time scale and budget. From these limitations, introducing a silicon tracker as a vertex detector is an effective and efficient solution. Fig. 102 shows the conceptual design of the silicon vertex tracker (SVT). The silicon sensors are placed only at small radii to form a couple of layers, and cover only the signal positron acceptance, namely the opposite side of the photon detector. This configuration works to minimize the generation of photons pointing to the photon detector as well as to reduce the area to be covered. Because measurements with a couple of layers are not sufficient to reconstruct positron trajectories, a main tracker is necessary outside SVT. Hence, SVT is not an alternative solution of the new tracker, but an optional

detector. Even with a few measurement points, SVT gives us powerful functions in tracking:

- providing precise measurements of muon decay vertices,
- providing precise measurements of positron emission angles,
- improving momentum measurement by providing precise initial point of tracking.

These functions can be obtained by putting the tracker close to the vertex points where the hit rate is extremely high.

One may think such an additional detector is not necessary if we construct a new tracker proposed in previous sections. We think it is important to have a redundancy of functions among detectors to promise the proposed performance. In this sense, SVT perfectly works. It might happen that the expected position resolution of the main tracker cannot be achieved for example because of a bad noise situation (as that happened for current DC system) until the final detector is constructed and the performance is verified. Even in such a case, SVT makes it possible to achieve the proposed resolutions. However, the greatest role of SVT would be given by the point that introducing SVT makes the design and construction of main tracker simpler and easier. Requirements for the main tracker will be relaxed and its development can be concentrated on the viewpoints of the detection efficiency and high-rate tolerance. For example, the limitation of beam rate for the proposed drift chamber is given by the hit rate at the inner-most wires. With SVT, we can think of the modified configuration of the new drift chamber where the radius of the inner-most wires is increased or the inner-most wires are removed without a cost of resolution. In such a way, we get the room of further improvement of the sensitivity.

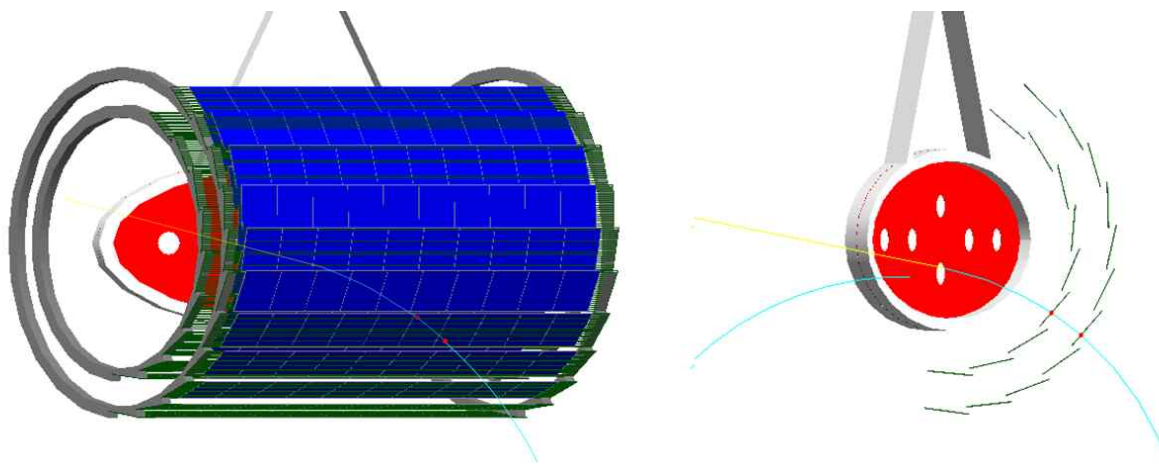


FIG. 102: Schematic view of double layer SVT.

## 2. Design

The most important parameter is the thickness of the silicon sensors. Low momentum positrons at about 50 MeV can be easily scattered by the nuclei of material put on its way. To study the intrinsic limitation from material effect, a simple MC simulation was performed. The results are shown in Fig. 103 for angle- and energy-measurement as well as detection efficiency as a function of the sensor thickness. It is turned out that the sensor of 100  $\mu\text{m}$  thickness or thicker is unacceptable for our purpose from the angle measurement point of view. On the other hand, it is also figured out that putting SVT does not affect the energy measurement. The timing resolution (or the readout speed) gives another requirement for the device when it is used at a high rate. To restrict the number of positrons hitting SVT in an event to less than a few dozens, a resolution of a few hundreds nanosecond is required. From these requirements, HV-MAPS is the first candidate. The advantages of this device are the possibility to be thinned (down to 30  $\mu\text{m}$ ), 100% fill factor, the good S/N, the fast signal collection, high radiation tolerance, the possibility to implement CMOS in-pixel electronics, and a low price. These features as well as the principle of the charged particle detection have been successfully tested [59, 60]. As the basis of the design, we assume a sensor similar to one proposed in the Mu3e experiment. Numbers assumed in the following study is summarized in Tab. XIX. The digitization and readout circuit will be implemented in the sensor itself by the CMOS technology. Thus, no other components like ASIC are necessary. The digitized signal is readout through flexible print on which the sensors are glued. This flexible print also works as a mechanical support at the barrel part. Since the power consumption of the MAPS-type devices is low enough to be cooled via helium gas, additional cooling system is not necessary. The material budget is  $0.8 \times 10^{-3} X_0$  per layer.

The momentum resolution in a given magnetic field depends on the number of measurement points, the position resolutions, the length of the measured track segment, and the multiple scattering. Adding SVT measurements effectively works to increase the measurement length, and hence to increase the sagitta. Increasing the number of layers between the first layer and the main tracker does not work for momentum measurement because the effect of multiple scattering dominates the effect of position resolution<sup>5</sup>. Precise measurements of vertex and angle can be achieved with at least two layers. Thus we propose a double-layer configuration for the basic design as schematically shown in Fig. 102. The radii of layers are one of the important parameters not only for the resolutions but also for the number of readout and mechanical structure. From the resolution point of view, smaller radii are better; the vertex resolution is, in the first order, proportional to the radius of the first layer. The limitation comes from the beam size. With current

---

<sup>5</sup> This is opposite to the case for the gaseous detectors where the effect of multiple scattering is smaller than the effect of worse position resolution which can be reduced by increasing the measurement points

beam profile, it is not possible to put SVT at radius smaller than  $\sim 5$  cm. The interval of layers contributes to the precision of the angle measurements. To minimize the finite size of the pixel, the interval should be larger; an interval of 10 mm corresponds to about 3 mrad contribution, and linearly suppressed as the interval increases. The actual radial positions will be determined by considering practical mechanical design, while we study with several numbers ranging from 5 to 8 cm. The area to be covered is defined by the angular acceptance of the whole spectrometer and the beam spot size. Because of the finite beam spot size and slanted target, SVT should cover  $\sim 160^\circ$  in  $\phi$  and  $\sim 20$  cm in  $z$  direction (about 35% solid angle). To cover the range, about 200 sensors are necessary, resulting in about 12 million pixels in total. At a 100 ns readout speed, average number of trajectories making hits on SVT is about three, and the maximum hit rate of a pixel is about 20 Hz (occupancy of  $2 \times 10^{-6}$ ) at  $1 \times 10^8 \mu^+$ /sec. The layout of the sensors is a usual ladder structure. The slant angle of the sensors from the tangent is optimized for signal positron to pass minimum length. The overlap of sensors is necessary for alignment purpose as well as to compensate possible dead space for the readout.

Other configurations are also under consideration. A single-layer configuration has a large merit from the material budget viewpoint, and it can be better depending on the performance of the main tracker. The single layer SVT and an active target can also be a good solution. The best configuration will be determined in combination with the main tracker performance.

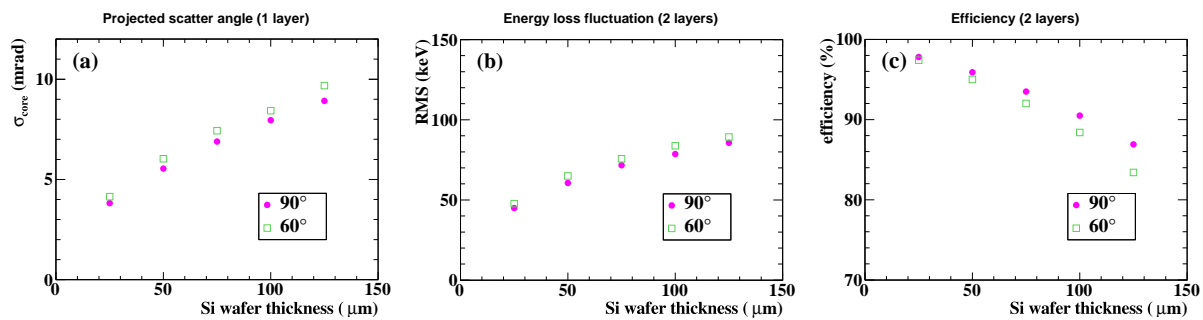


FIG. 103: Intrinsic limitation on measurement of 52.8 MeV positrons by the thickness of silicon sensor for two incident angle cases. (a) Limitation on the angle measurement coming from the projected (plane) scatter angle at the first layer. (b) Limitation on the energy measurement coming from the energy loss fluctuation on both layers. (c) Limitation on the detection efficiency. Efficiency here is defined as the fraction of events with the (space) scatter angle by the two layers is less than 50 mrad and the energy loss is less than 300 keV.

TABLE XIX: Design parameters of silicon sensors.

Sensor size	$20 \times 20 \text{ mm}^2$
Sensor thickness	$50 \mu\text{m}$
Pixel size	$80 \times 80 \mu\text{m}^2$
Readout speed (timestamp)	100 ns

### 3. Expected performance

The expected performance of SVT is being evaluated using MC simulation based on GEANT4. The functionality of SVT is studied in combination with the current DC system. Two MC samples of signal positrons, with and without putting SVT, were generated without event mixing, and analyzed with our reconstruction tool. In the case of with SVT, first the tracking is performed as usual only with DC, and then the interconnection is tried between the extrapolated trajectory and the SVT hits. If the interconnection is successful, the SVT hits are integrated into the Kalman filter and final track fit is performed. An example of the track reconstruction is shown in Fig 104. The performances of the two cases are evaluated after applying our nominal event selection. The results are summarized in Tab. XX. Because of the current reconstruction procedure, adding SVT hits cannot increase the number of reconstructed tracks. Even with such a preliminary reconstruction, the total efficiency after applying the final event selection increases thanks to the improvement of the reconstruction quality.

TABLE XX: Comparison of the spectrometer (current DC base) performance with and without SVT (double-layer at (5.9, 7.5 cm)). Resolutions are given in sigma.

	DC only	DC & SVT
Momentum resolution, core component (keV)	233	150
Fraction of the core component (%)	83	91
$\phi$ resolution (mrad)	12	7.2
$\theta$ resolution (mrad)	8.2	7.0
Vertex resolution, Y / Z (mm)	1.8 / 2.3	0.48 / 0.39
Efficiency (%)	48	52

The effect on the additional photon yield is also evaluated with the MC. The photon yield from Michel positrons (bremsstrahlung or AIF) are shown in Fig. 105 for current system and that with SVT as a function

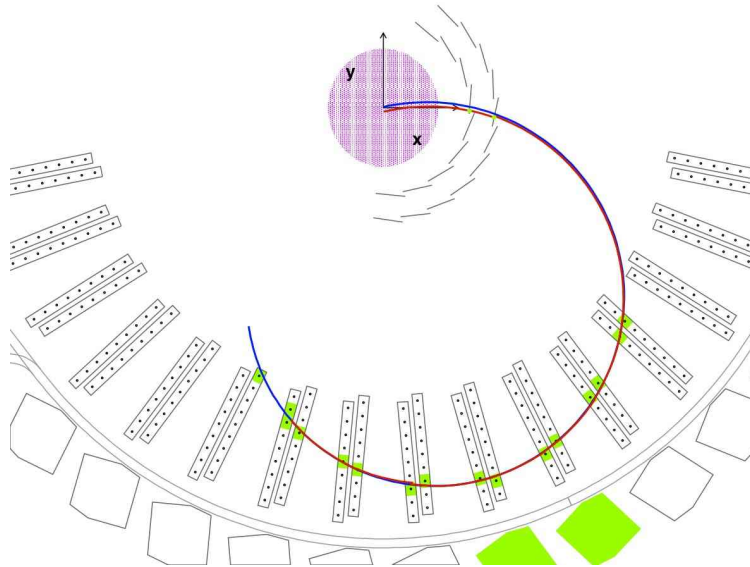


FIG. 104: Tracking with SVT and current DC for a simulated signal positron. Blue line shows the reconstructed trajectory only using DC measurements, while red one shows that with SVT measurements too.

of the energy deposition in LXe of the photon detector. The increase of the yield is clearly seen for low energy part, while at high energy the yield is not increased because of the geometrical configuration. The main contribution for the high energy photon yield comes from DC, while it will be significantly reduced with a new tracker in upgrade experiment. Thus, we also investigated the photon yield with TPC tracker. The results of photon yield which make energy deposit in LXe larger than  $0.9 \times M_\mu/2$  are summarized in Tab. XXI. The increment due to SVT for the total photon yield (including one from RMD) can be suppressed lower than 5% even. Low-energy photons increase the hit rate of the photon detector and can be backgrounds via pileup. The photon yield originated from positrons increases by 75% for  $E_{\text{dep}} > 10$  MeV, while the dominant source at the region is RMD. The total increment due to SVT is about 10%.

### E. R&D on New Scintillator Material for Timing Counter

In the last few years organic scintillators have been investigated in order to achieve higher light yield than the usual plastic or liquid scintillators. It has been shown that very pure organic compound with high quality crystal structure can achieve superior light yield performance in combination with fast decay time. Among a large number of types of organic compounds only few ones have proven to have practical applications. These are for example the stilbene and *p*-terphenyl [61]. Both have light yield about 3 times higher than

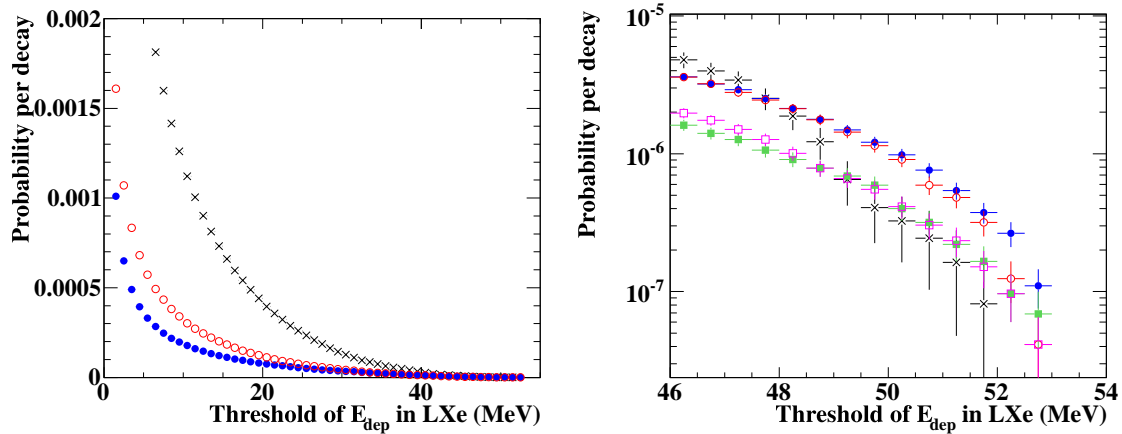


FIG. 105: Integrated photon yield per muon decay. Right figure is the close-up view around the signal region, where the cases of TPC option are also shown. Black cross markers shows photon yield from RMD and the others show those originated from positrons (bremsstrahlung or AIF). Red: DC (current system), blue: DC + SVT, green: TPC, magenta: TPC + SVT configuration, respectively.

TABLE XXI: Photon yield for energy deposition in LXe larger than  $0.9 \times M_\mu/2$ .

Detector setup	yield ( $10^{-6}$ )
RMD	2.5
AIF, DC (current system)	2.5
AIF, DC + SVT	2.5
AIF, TPC	1.1
AIF, TPC + SVT	1.2

ordinary plastics and a decay time of few nanoseconds. It has been found also that the crystal sizes must be larger than the range of the charged particles to be detected, otherwise the light output decreases of a large amount. In case of particle with small range, the detector can be made of poly-crystal samples. Conversely, in our case whose positrons have tracks longer than the typical sizes of scintillators, we need to adopt large pieces of single crystals. Large single crystals begin to be commercially available: single crystals with linear sizes of 10 cm have been recently produced. Doped *p*-terphenyl single crystal is a very appealing option for a fast and high light output pixel of the timing counter. Below are listed the measured properties of actual samples from ALKOR company [62]. We notice that the data are preliminary since the investigations are in progress at the INFN of Genova.

- Light yield:  $2.7 \times 10^4 (2.7 \times 10^4)$

- Maximum of emission: 390 nm (420 nm)
- Attenuation length (see explanation): > 5 cm

The emission spectrum has characteristic features with 3 peaks and is slightly blue-shifted. As suggested by previous studies reported in literature this could be caused by two effects: first, a reduced self absorption at lower wavelengths due to *p*-terphenyl fine powder at the not polished surfaces of the sample and, second, to a lower level of dopant, biphenyl butadiene, that act as wavelength red-shifter. The attenuation length has been obtained with a *p*-terphenyl slab with section of  $3 \times 5 \text{ mm}^2$  and 50 mm length. The slab has been wrapped with high reflectance foil from 3M and the surfaces are finished at optical level. The data have been acquired with two Hamamatsu  $1 \text{ mm}^2$  SiPMs at each end and a collimated beam of electrons from a  $^{90}\text{Sr}$  radioactive source. Thanks to the high light yield the SiPM pulse amplitude, about hundred of mV, signal is sent to the digitizer without any loss of signal to noise ratio. These features are very appealing for a possible application as active material for the pixels of the timing counter. Further assessments are necessary and a proper evaluation of cost to benefit ratio.

#### F. Development of New Photomultiplier Tube (PMT) for LXe Detector

A small and square-shaped PMT can also be a candidate for the replacement of the current PMT. The biggest advantage is that it is a well-proven technology and has been long working quite well in the MEG experiment. The drawbacks compared to SiPM are its larger thickness and thick insensitive edge of the pressure-proof package.

Two types of PMTs are under development in collaboration with Hamamatsu Photonics.

- 1-inch square-shape PMT

The 1-inch square-shape PMT is a smaller version of the current PMT as shown in Fig. 106. The quantum efficiency (QE) is expected to improve from 15% to 20-30% for LXe scintillation photon. The prototypes are being tested in the test facilities at KEK and Pisa.

- 2-inch flat panel multi-anode PMT

The left picture in Fig. 107 shows a sketch of the prototype of 2-inch flat panel multi-anode PMT developed for LXe use. It is based on Hamamatsu H8500 64-channels multi-anode PMT. It has the same dynode structure as the current PMT (metal-channel) enabling its compact design, fast response (TTS of 0.4 ns) and high gain ( $1.5 \times 10^6$  at -1100 V). The dimension is  $52 \times 52 \times 27.4 \text{ mm}$  which is not smaller than the current PMT, but it is position sensitive with  $8 \times 8$  pixels with a size of  $5.8 \times 5.8 \text{ mm}^2$

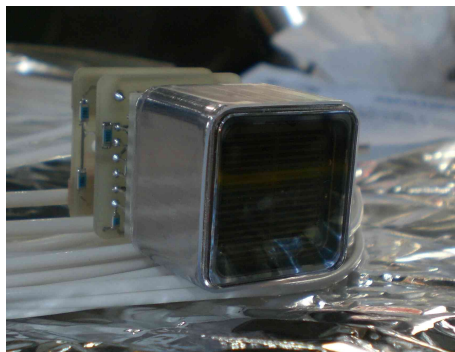


FIG. 106: 1-inch square-shape PMT developed for the MEG experiment.

each. The high voltage is common to all the channels and the channel-to-channel gain variation is  $\pm 20\%$ . A careful calibration would, therefore, be required. The same bleeder circuit as for H8500 can be used with Zener diode protection for high rate operation.

A pressure-proof package design is in progress as shown in Fig. 107 and the first working prototype is expected to arrive in 2013.

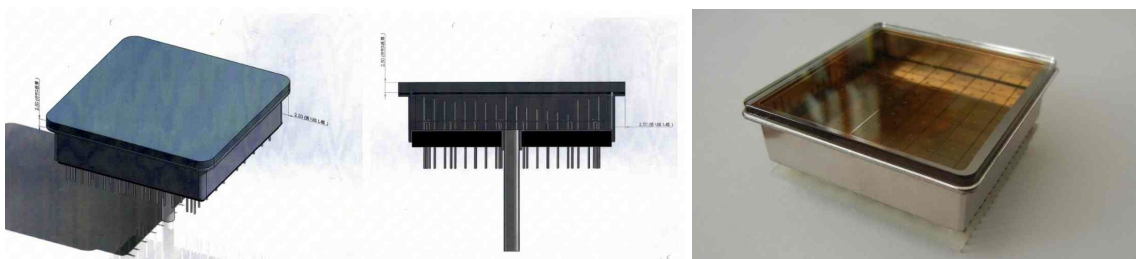


FIG. 107: (Left) Design of the prototype of 2-inch flat panel multi-anode PMT developed for LXe in collaboration with Hamamatsu Photonics and (right) a prototype of the pressure-proof package with a quartz window where a VUV-sensitive photocathode is deposited, but without a dynode structure.

- 
- [1] S. Ritt, R. Dinapoli, and U. Hartmann. Application of the DRS chip for fast waveform digitizing. *Nucl. Instr. and Meth. A*, 623(1):486 – 488, 2010. 1st International Conference on Technology and Instrumentation in Particle Physics.
- [2] R.M. Carey et al. Fermilab proposal 0973: <http://mu2e.fnal.gov>. Technical report.
- [3] D. Bryman and others: [http://j-parc.jp/NuclPart/pac\\_0801/pdf/Kuno.pdf](http://j-parc.jp/NuclPart/pac_0801/pdf/Kuno.pdf). Technical report.
- [4] A. Blondel, A. Bravar, M. Pohl, S. Bachmann, N. Berger, A. Schöning, D. Wiedner, P. Fischer, I. Perić, M. Hildebrandt, P.-R. Kettle, A. Papa, S. Ritt, G. Dissertori, Ch. Grab, R. Wallny, P. Robmann, and U. Straumann. Letter of intent for an experiment to search for the decay  $\mu \rightarrow 3e$ : PSI LoI R-12-03.0. Technical report, January 2012.
- [5] B. O’Leary et al: arXiv:1008.1541. 2010.
- [6] A.G.Akeroyd et al: arXiv:1002.5012. 2010.
- [7] L. Calibbi, D. Chowdhury, A. Masiero, K.M. Patel, and S.K. Vempati. Status of supersymmetric type-i seesaw in so(10) inspired models. *JHEP*, 1211:040, 2012.
- [8] R. Barbieri and L. J. Hall. *Phys. Lett. B*, 338:212, 1994.
- [9] J. Hisano. . *Phys. Rev.*, D59:116005, 1999.
- [10] L. Calibbi et al. *Phys. Rev. D*, 74:116002, 2006.
- [11] Lorenzo Calibbi, Michele Frigerio, Stephane Lavignac, and Andrea Romanino. Flavour violation in supersymmetric SO(10) unification with a type II seesaw mechanism. *JHEP*, 0912:057, 2009.
- [12] J. K. Ahn et al.; ArXiv:1204.0626, 2012.
- [13] F. P. An et al., 2012.
- [14] K. Abe et al. *Phys. Rev. Lett.*, 107:041801, 2011.
- [15] Y. Abe et al. *Phys.Rev.Lett.*, 108:131801, 2012.
- [16] S. Antush et al. *JHEP*, 11:090, 2006.
- [17] G. Blankenburg et al. ; ArXiv:1204.0688v1, 2012.
- [18] A. de Gouvea and N. Saoulidou. Fermilab’s Intensity Frontier. *Annu. Rev. Nucl. Part. Sci.*, 60:513–38.
- [19] J. Adam et al. Calibration and monitoring of the MEG experiment by a proton beam from a Cockcroft-Walton accelerator. *Nucl. Instr. and Meth. A*, 641:19-32, 2011.
- [20] A. Baldini et al. A radioactive point-source lattice for calibrating and monitoring the liquid xenon calorimeter of the meg experiment. *Nucl. Instr. and Meth. A*, 565(2):589 – 598, 2006.
- [21] A.E. Pifer, T. Bowen, and K.R. Kendall. A High Stopping Density mu+ Beam. *Nucl.Instrum.Meth.*, 135:39–46, 1976.
- [22] M. Adinolfi et al. *Nucl. Instr. and Meth. A*, 448:51, 2002.
- [23] ANSYS®.
- [24] C. Niebhur et al. *Nucl. Instr. and Meth. A*, 566:118–122, 2006.
- [25] A. Andryakov et al. *Nucl. Instr. and Meth. A*, 409:84, 1998.
- [26] G.F. Tassielli et al. *Nucl. Instr. and Meth. A*, 572:198, 2007.

- [27] A. Baschirotto et al. A cmos high-speed front-end for cluster counting techniques in ionization detectors. 2007. 2nd International Workshop on Advances in Sensors and Interface. IWASI 2007.
- [28] V. Re et al. *Nucl. Instr. and Meth. A*, 560:5, 2006.
- [29] *GARFIELD - Simulation of gaseous detectors*: <http://garfield.web.cern.ch/garfield>.
- [30] A. Stoykov et al. G-apd + plastic scintillator: fast timing in high magnetic fields., 6th International Conference on New Developments in Photodetection, Lyon, France, 4-8 July 2011: <http://ndip.in2p3.fr/ndip11/AGENDA/AGENDA-by-DAY/Presentations/5Friday/PM/ID17-Stoykov.pdf>.
- [31] A. Stoykov et al. A time resolution study with a plastic scintillator read out by a Geiger-mode Avalanche Photodiode. *Nucl. Instrum. Meth.*, A695:202–205, 2012.
- [32] Saint-Gobain Premium Plastic Scintillators: [http://www.detectors.saint-gobain.com/uploadedFiles/SGdetectors/Documents/Product\\_Data\\_Sheets/BC418-420-422-Data-Sheet.pdf](http://www.detectors.saint-gobain.com/uploadedFiles/SGdetectors/Documents/Product_Data_Sheets/BC418-420-422-Data-Sheet.pdf).
- [33] Hamamatsu Photonics MPPC S10931-050P: <http://sales.hamamatsu.com/en/products/solid-state-division/si-photodiode-series/mppc/part-s10931-050p.php>.
- [34] FBK-AdvanSiD ASD-SiPM3S-P-50: [http://www.advansid.com/sites/www.advansid.com/files/ASD-SiPM3S-P\\_V4.pdf](http://www.advansid.com/sites/www.advansid.com/files/ASD-SiPM3S-P_V4.pdf).
- [35] KETEK PM3350: <https://indico.cern.ch/getFile.py/access?contribId=18&sessionId=0&resId=0&materialId=slides&confId=164917>.
- [36] G. Punzi. Sensitivity of searches for new signals and its optimization, 2003.
- [37] Hamamatsu Photonics Picosecond light source PLP-10: <http://sales.hamamatsu.com/en/products/system-division/ultra-fast/picosecond-light-sources.php>.
- [38] Private communication with Dr. A. Stoykov of Paul Scherer Institut.
- [39] Jozsef Janicsko-Csathy, Hossein Aghaei Khozani, Xiang Liu, Bela Majorovits, and Allen Caldwell. Development of an anti-Compton veto for HPGe detectors operated in liquid argon using Silicon Photo-Multipliers. *Nucl.Instrum.Meth.*, A654:225–232, 2011.
- [40] T. Matsumura, T. Shinkawa, T. Hirai, K. Miyabayashi, T. Hiraiwa, et al. Radiation damage to MPPCs by irradiation with protons. *PoS*, PD07:033, 2006.
- [41] T. Matsubara, H. Tanaka, K. Nitta, and M. Kuze. Radiation damage of MPPC by gamma-ray irradiation with Co-60. *PoS*, PD07:032, 2006.
- [42] V. Andreev, V. Balagura, B. Bobchenko, P. Buzhan, J. Cvach, et al. A high granularity scintillator hadronic-calorimeter with SiPM readout for a linear collider detector. *Nucl.Instrum.Meth.*, A540:368–380, 2005.
- [43] T. Nagano et al. Timing Resolution Improvement of MPPC for TOF-PET Imaging. In *IEEE Nuclear Science Symposium Conference Record*, October 2012.
- [44] M. Yokoyama, A. Minamino, S. Gomi, K. Ieki, N. Nagai, et al. Performance of Multi-Pixel Photon Counters for the T2K near detectors. *Nucl.Instrum.Meth.*, A622:567–573, 2010.
- [45] H. Anderhub, M. Backes, A. Biland, A. Boller, I. Braun, et al. FACT – the First Cherenkov Telescope using a G-APD Camera for TeV Gamma-ray Astronomy (HEAD 2010). *Nucl.Instrum.Meth.*, A639:58–61, 2011.

- [46] Radiall MIL-C-17/93-RG178 (P/N : C291 145 007) : <http://www.radiall.com/media/files/RFCableAssemblies%20D1C004XEe.pdf>.
- [47] S. Agostinelli et al. Geant4—a simulation toolkit. *Nucl. Instr. and Meth. A*, 506(3):250–303, 2003.
- [48] J. Adam et al. New limit on the lepton-flavour violating decay  $\mu^+ \rightarrow e^+\gamma$ . *Phys. Rev. Lett.*, 107:171801, 2011.
- [49] A. Papa et al. Development of an active target for a  $\mu \rightarrow e\gamma$  search. *Nucl. Instr. and Meth. A*, 2012.
- [50] R. D Bolton et al. Search for rare muon decays with the crystal box detector. *Phys. Rev. D*, 38(7):2077–2101, Oct 1988.
- [51] M. Ahmed et al. Search for the lepton-family-number nonconserving decay  $\mu^+ \rightarrow e^+\gamma$ . *Phys. Rev. D*, 65:112002, Jun 2002.
- [52] Fabio Sauli. Imaging with the gas electron multiplier. *Nucl. Instr. and Meth. A*, 580:971–973, 2007.
- [53] A. Balla et al. Status of the cylindrical-gem project for the kloe-2 inner tracker. *Nucl. Instr. and Meth. A*, 628:194–198, 2011.
- [54] H. Fenker et al. Bonus: Development and use of a radial tpc using cylindrical gems. *Nucl. Instr. and Meth. A*, 592:273–286, 2008.
- [55] G. Lutz, R.H. Richter, and L. Strüder. Novel pixel detectors for X-ray astronomy and other applications. *Nucl. Instr. and Meth. A*, 461(1-3):393–404, April 2001.
- [56] R. Turchetta et al. CMOS Monolithic Active Pixel Sensors (MAPS): New eyes for science. *Nucl. Instr. and Meth. A*, 560(1):139–142, May 2006.
- [57] Y. Arai, T. Miyoshi, Y. Unno, T. Tsuboyama, S. Terada, Y. Ikegami, T. Kohriki, K. Tauchi, Y. Ikemoto, and R. Ichimiya. Developments of SOI monolithic pixel detectors. *Nucl. Instr. and Meth. A*, 623(1):186–188, November 2010.
- [58] I. Perić. A novel monolithic pixelated particle detector implemented in high-voltage CMOS technology. *Nucl. Instr. and Meth. A*, 582(3):876–885, December 2007.
- [59] I. Perić and C. Takacs. Large monolithic particle pixel-detector in high-voltage CMOS technology. *Nucl. Instr. and Meth. A*, 624(2):504–508, December 2010.
- [60] I. Perić, C. Kreidl, and P. Fischer. Particle pixel detectors in high-voltage CMOS technology New achievements. *Nucl. Instr. and Meth. A*, 650(1):158–162, September 2011.
- [61] S. V. Budakovskiy et al. New generation of organic scintillation materials. *Functional materials*, 16(1):86, 2009.
- [62] <http://www.alkor.net/Scintillators.html>.